



BOURNEMOUTH UNIVERSITY

**NUMERICAL MODELLING OF THE ALUMINIUM EXTRUSION
PROCESS WHEN PRODUCING COMPLEX SECTIONS**

LONGJIANG NIU

Doctor of Philosophy

November 2010

**NUMERICAL MODELLING OF THE ALUMINIUM EXTRUSION
PROCESS WHEN PRODUCING COMPLEX SECTIONS**

LONGJIANG NIU

**A thesis submitted in partial fulfillment of the requirements of
Bournemouth University for the degree of Doctor of Philosophy**

November 2010

Bournemouth University

Copyright Statement

This copy of the thesis has been supplied on condition that anyone who consults it is understood to recognise that its copyright rests with its author and due acknowledgment must always be made of the use of any material contained in, or derived from, this thesis.

Abstract

Longjiang Niu

Numerical Modelling of the Aluminium Extrusion Process when Producing Complex Sections

This thesis reports the analysis by FEM of both continuum and structural models describing the extrusion process. They were compared with experimental work and the agreement is satisfactory.

All the simulations were performed with the implicit finite element code Forge2009[®] with user input written in Visual Fortran[®]. Alloys AA2024 and AA6063 were utilised as the source materials in order to compare with published experimental work.

The Forge2009[®] 2D module was used to investigate both direct and indirect axisymmetric rod extrusions. The extrusion load and the temperature rise were predicted and the load-displacement curves and the events that took place in both extrusion modes were also simulated, discussed and again verified. The effects of the difference between the two modes, especially friction and its consequences on the process were investigated. The indirect results point to a good method of improving efficiency.

For complex solid section, the 3D module has been used to study the load required, temperature evolution, surface formation of the extrudate and material flow during the process. These all showed good correlation with experimental results. The microstructure evolution during the extrusion process and the following solution soaking process were simulated with physically-based mathematical microstructure models integrated into FEM through its Fortran[®] subroutine interface,. The agreement between the predicted microstructures using associated models and experimental measurements were acceptable. For hollow section, the emphasis was placed on the study of the complicated metal flow and the seam welding quality. Novel analyses were developed to analyse the metal flow.

List of symbols

A	material constant (eq(2.8),(2.9), (2.14))
A_B	cross sectional area of the extrudate
A_C	cross sectional area of the container bore
a	constant (eq(2.3), (2.12))
B	material constant (eq(2.8),(2.9), (2.14), (5.1))
B_n	linear operator
b	magnitude of Burgers vector constant (eq(2.3), (2.12))
C	constant (eq(2.5),(2.6))
C_{cr}	critical value for the material to be damaged
C_d	constant
C_t	constant
c	constant (eq(2.3), (2.12))
D_C	diameter of the container bore
D_E	equivalent diameter of the extrudate
D_0	pre-growth grain diameter
d	constant (eq(2.3))
d_{rex}	recrystallised grain size
d_0	initial grain diameter
E	energy per unit length of dislocation line
E_{el}	elastic energy of distributed edge dislocation
E_{sb}	energy per unit length of low angle tilt boundary
F_j	point force
G	universal gas constant (eq(2.10)) grain growth rate (eq(5.7)) shear modulus (eq(5.32))
G_0	constant (eq(5.9))
h_{ch}	height of the welding chamber
J_1	first invariant of the stress tensor
J_2	second invariant of the stress tensor
J_3	third invariant of the stress tensor
k	constant (eq(2.12), (5.1))
L_c	length of dislocations annihilated
\bar{L}_0	mean linear intercept at zero strain
l	welding path
M	Talor factor
M_{GB}	grain boundary mobility
M_m	shape function for the nodal pressure
M_0	constant prefactor of the grain boundary mobility
m	strain rate sensitivity index (eq(3.11)) Tresca friction coefficient (eq(3.14))
m_0	constant (eq(3.11))
m_1	constant (eq(3.11))

N_L	number of boundaries per unit length
N_n	shape function
N_V	nucleation sites per unit volume
n	inverse of the temperature compensated strain rate sensitivity (eq(2.8),(2.9))
P	pressure
P_D	stored energy per unit volume
P_i	material properties invariant
P_j	body force
p	constant (eq(2.12))
\mathbf{p}	pressure field
\mathbf{P}_m	nodal pressure
\dot{Q}_d	heat generation rate due to deformation per unit volume
Q_{def}	activation energy for deformation
Q_{GB}	activation energy for grain boundary migration
q	constant (eq(2.12))
R	extrusion ratio
R_{ρ_e}	radius caused by excess dislocation of a given Burgers vector
R_{ρ_δ}	radius caused by misorientation across subgrain boundaries
r	constant (eq(2.12))
r_0	radius of dislocation core
r_1	outer cut-off radius
S	surface area of the calculated domain (eq(3.2))
\mathbf{S}	general deformation matrix (eq(5.15))
S_i	state variables
S_j	value of a microstructure state variable
S_{j0}	value of the microstructure state variable microstructure state variable S_j before a change of deformation conditions
S_{js}	value of the microstructure state variable microstructure state variable S_j after a change of deformation conditions
S_V	grain boundary area per unit volume
S_{V_0}	grain boundary area per unit volume at zero strain
T	temperature
T_j	surface force
T_m	lowest melting point
t_{50}	time to 50% recrystallisation
t	holding time (eq(5.1))
t_w	contact time of the two metal streams
U	total stored energy per unit volume
U_i	energy per unit volume for internal dislocations
U_{sb}	energy per unit volume for subgrain boundaries
u_j	displacement
V	volume
\mathbf{V}_n	nodal velocity field
V_R	ram speed

v	velocity field
\bar{v}_m	mean velocity of mobile dislocations
v_{avg}	average flow velocity of the metal in the welding chamber
\hat{W}	virtual work resulting from the strain due to the virtual displacement
w	distance between the sites of cross-slip or climb events
\mathbf{X}_n	coordinate vector
\mathbf{X}_V	volume fraction recrystallised
x	displacement field
Z	temperature compensated strain rate parameter
Z^*	material constant
α	material constant
α'	material constant
β	constant (eq(2.12), (2.15)) drag force (eq(5.37))
ΔH	activation energy for hot deformation
δ	subgrain size
δ_{ss}	subgrain size at steady state
ε	mean equivalent strain or effective strain
$\bar{\varepsilon}$	mean equivalent strain or effective strain
$\dot{\varepsilon}$	strain rate tensor
$\dot{\bar{\varepsilon}}$	mean equivalent strain rate or effective strain rate
$\hat{\varepsilon}_{ij}$	virtual strain
ε_{js}	characteristic strain that controls the strain over which steady-state is reached
ε_θ	characteristic strain for misorientation growth
ε_δ	characteristic strain for subgrain growth
θ	misorientation across subgrain boundaries
θ_c	critical angle for high angle grain boundary
θ_{ss}	misorientation across subgrain boundaries at steady state
Λ_r	mean distance travelled by the dislocation before it is stopped
λ	heat generation efficiency (eq(2.4))
μ	friction coefficient
ν	Poisson ratio
ξ	local coordinate vector
ρ	total dislocation density
ρ_b	boundary dislocation density
ρ_e	equivalent distributed dislocation density for a simple low angle tilt boundary (eq(5.28)) excess dislocation or ‘geometrically necessary’ dislocation density (eq(5.39))
ρ_g	‘geometrically necessary’ dislocation density
ρ_i	internal dislocation density
ρ_r	random dislocation
σ	flow stress
$\bar{\sigma}$	equivalent stress or effective stress
σ_{N-H}	Norton-Hoff flow stress

σ_{Z-H}	Zener-Hollomon flow stress
σ_f	friction stress
σ_{ij}	Cauchy stress tensor
σ_m	mean stress or hydrostatic stress
σ_n	normal stress
σ_1	the first principal stress
σ_2	the second principal stress
σ_3	the third principal stress
τ	friction stress
ω	semi-angle of the deformation zone in direct extrusion (eq(2.3))

List of contents

Copyright Statement	1
Abstract	2
List of symbols	3
List of contents	7
List of Figures	13
List of Tables	17
Acknowledgement	18
Author's Declaration	19
1. Introduction	20
1.1 Aluminium alloys and aluminium extrusion process	20
1.2 Modelling of extrusion process	24
1.3 Objective of this research	26
2. Literature review	27
2.1 Numerical modelling and simulation of aluminium extrusion	27
2.1.1 Introduction	27
2.2 Numerical methods used for bulk metal forming modelling	30
2.3 Main parameters established by experiment (empiricism)	33
2.3.1 Extrusion ratio	33
2.3.2 Plastic strain and strain rate	34
2.3.3 Friction	35
2.3.4 Extrusion pressure	36
2.3.5 Heat transfer and temperature	36
2.4 Constitutive laws used for hot working metal FEM simulation	38

2.4.1	Yield criterion.....	38
2.4.2	Viscoplastic model	38
2.5	Thermal-mechanical process modelling using the Finite Element Method	41
2.6	Microstructure modelling.....	42
2.6.1	Empirical models for structure prediction.....	43
2.6.2	Probabilistic (statistical) methods and neural network method...	45
2.6.3	Neural network method	47
2.6.4	Physically-based internal variable methods	47
2.6.4.1	Introduction	47
2.6.4.2	The internal state variable formalism	48
2.6.4.3	Modelling dislocation substructure changes	51
2.6.4.3.1	Dislocation substructure evolution	51
2.6.4.3.2	Dislocation density evolution modelling	53
2.6.4.3.3	Subgrain size modelling.....	54
2.6.4.3.4	Misorientation change modelling	55
3.	Thermal-mechanical simulation of the extrusion process	57
3.1	Introduction	57
3.2	Finite element procedure.....	57
3.3	The equilibrium equation in FE simulations.....	58
3.4	Finite element kinematical description	59
3.5	Finite element discretisation and element type	60
3.6	Finite element discretisation and increment approach.....	61
3.7	Constitutive equations	63
3.7.1	Norton-Hoff equation	63
3.7.2	Zener-Hollomon equation	64

3.8	Friction model	64
3.9	FE approach of the coupled thermal and mechanical problem.....	66
3.10	Techniques used in the FEM simulation.....	66
3.11	Data file and user-subroutine	70
3.11.1	The data file.....	70
3.11.2	The user subroutine and its integration with Forge2009 [®] solver...	71
3.12	Concluding remarks	73
4.	Forge[®] validation using both original observations and results from the literature.....	74
4.1	Introduction of direct and indirect extrusion simulations	74
4.2	Extrusion experiments for validation	75
4.2.1	Extrusion press	75
4.2.2	Material compositions	77
4.2.3	Tooling	77
4.2.4	FEM model setup	78
4.3	Extrusion load validation	80
4.4	Temperature evolution during extrusion.....	81
4.4.1	Comparison between predicted temperature and experiment	81
4.4.2	Billet temperature distributions for both direct and indirect extrusions	83
4.5	Metal flow and surface formation.....	84
4.5.1	The application of Grain Flow technique.....	85
4.5.2	The application of the Sensor technique	87
4.6	Microstructure prediction in simple 2D simulation.....	93
4.7	Concluding remarks	96
5.	Complex solid section extrusion simulation and integrated microstructure prediction	98

5.1	Introduction	98
5.2	Mathematical model and the determination of the relevant parameters	98
5.2.1	Volume fraction recrystallised X_V	98
5.2.2	Time to 50% recrystallisation t_{50}	99
5.2.3	Grain boundary mobility M_{GB}	100
5.2.4	N_V and C_d in the equation (5.10).....	104
5.2.5	Grain boundary surface area per unit volume S_V	105
5.2.6	The stored energy P_D	108
5.2.7	The equations for evolutions for dislocation characteristics	110
5.2.7.1	Evolution of internal dislocation	110
5.2.7.1.1	Using Holt relation to calculate internal dislocation density and subgrain size at steady state	110
5.2.7.1.2	Evolution of internal dislocation at transient deformation state	111
5.2.7.1.2.1	Evolution of geometrically necessary internal dislocation	113
5.2.7.1.2.2	Incremental equations for the evolution of subgrain structure	117
5.3	Simulation considerations	119
5.4	Simulated results of solid section extrusion.....	122
5.4.1	Load prediction.....	122
5.4.2	Strain, strain-rate and temperature distribution.....	123
5.4.3	Material flow analysis	127
5.5	Microstructure prediction.....	131
5.5.1	Grain boundary area per unit volume S_V and the density of recrystallisation nuclei N_V	132
5.5.2	The prediction of dislocation density ρ and subgrain size δ and misorientation θ	134

5.5.3	The prediction of stored energy.....	139
5.5.4	The volume fraction recrystallised	140
5.5.5	The predicted recrystallised grain size	143
5.6	Concluding remarks	145
6.	Hollow section extrusion simulation and its weld seam quality prediction	147
6.1	Introduction	147
6.2	Experiment procedure	148
6.3	FEM simulation.....	148
6.3.1	The determination of the constants of the constitutive equation for AA6063 alloy.....	148
6.3.2	One-sixth FEM model	150
6.3.3	Load and temperature evolution prediction.....	151
6.3.4	Metal flow and surface formation	156
6.3.5	Weld seam formation and its quality criteria	164
6.3.6	The simulation of one-third self-contact model	170
6.3.6.1	One-third self-contact FE model	173
6.3.6.2	Predicted load, temperature and equivalent strain using the one-third model	174
6.4	Concluding remarks	179
7.	Conclusions and further research	181
7.1	Conclusions	181
7.2	Further research.....	182
8.	Appendix A.....	184
9.	Appendix B	194
10.	Appendix C.....	195
11.	Appendix D.....	197

12. Appendix E	199
13. Appendix F	201
14. References	205
15. Publications	217

List of Figures

Figure 1.1 (left) Direct and (right) indirect extrusion layout (Sheppard 1999a, p.9)	22
Figure 2.1 Procedure for numerical modelling (Bograd 2004)	29
Figure 2.2 A schematic representation of the microstructure; cell diameter, δ , cell wall thickness, h , cell wall dislocation density ρ_b and dislocation density within the cells ρ_i (after Nes 1997)	51
Figure 2.3 Sub-boundary misorientation vs. strain	56
Figure 3.1 Modified Coulomb friction law	65
Figure 3.2 Symmetry and auto-trim used in 2D simulation	68
Figure 3.3 Symmetry and auto-trim used in a 3D simulation	69
Figure 4.1 General layout of the extrusion press and the direct and indirect tooling (Subramanian 1989, p.49)	75
Figure 4.2 The die used for rod extrusion (in mm)	77
Figure 4.3 FEM model of the rod extrusion	78
Figure 4.4 Variation of load with ram displacement for both modes of extrusion	80
Figure 4.5 Temperature changes according to Grasmø <i>et al</i> 's experiment (1992)	82
Figure 4.6 Forge [®] predicted temperature vs. Grasmø's experimental measurements at the thermocouple 7 (Flitta and Sheppard 2005)	82
Figure 4.7 Temperature distribution for (a) direct and (b) indirect extrusions at the ram travel of 65mm (in °C)	83
Figure 4.8 Simulated flow patterns (a) at 300°C (b) at 450 °C and the corresponding experimental flow patterns (c) at 300°C and (d) at 450 °C (Flitta 2004, p.125)	85
Figure 4.9 (a) Predicted flow pattern (Peng 2005, p.82) and (b) experiment result (Peng 2005, p.84) in an indirect extrusion	86
Figure 4.10 Simulated flow patterns (a) direct and (b) indirect extrusions	86
Figure 4.11 Sensors' initial positions (a) for direct and (b) indirect extrusions	87
Figure 4.12 Positions of sensors (a) for direct extrusion at ram displacement 9mm and (b) for indirect extrusion at ram displacement 9.5mm	88
Figure 4.13 Relation between ram travel and sensor distance from the extrudate surface (a) for direct extrusion and (b) for indirect extrusion	91
Figure 4.14 Subgrain size distribution (Peng 2005, p.89)	93
Figure 4.15 Transverse subgrain size and temperature distribution (Peng 2005,	

p.88).....	94
Figure 4.16 Predicted volume fraction recrystallised factor (X_V) along the extrudate surface and the selected point.....	94
Figure 4.17 Distribution of parameter Z ($\times 10^{10}$) (a) direct and (b) indirect extrusions.....	95
Figure 5.1 Tetrakaidecahedron (Zhu <i>et al.</i> 2007).....	106
Figure 5.2 Relationships between local lattice curvature and (a) excess dislocations of a given Burgers vector and (b) subgrain boundary (microband) spacing and misorientation (Baxter <i>et al.</i> 1999)	113
Figure 5.3 Local lattice curvature of Al-1%Mg deformed at 385°C (Sellars and Zhu 2000)	116
Figure 5.4 Comparison of calculated and experimental data of (a) internal dislocation density; (b) subgrain size and (c) misorientation between subgrains (Sellars and Zhu 2000)	116
Figure 5.5 Dies geometries, dimensions in <i>mm</i> (Sheppard 1993).....	119
Figure 5.6 FEM configurations prior to simulation for (a) square, (b) T-shape and (c) U-shape where part A is the ram, part B, the container, part C the billet and part D the die (orifice).....	120
Figure 5.7 Schematic for multi mesh boxes and auto-trim settings	121
Figure 5.8 Predicted loads variations for different shape extrusions	122
Figure 5.9 Equivalent strain distribution during steady state.....	124
Figure 5.10 Strain rate (s^{-1}) distributions on the cross-sections	125
Figure 5.11 Temperature ($^{\circ}C$) distributions of different shape extrusions.....	126
Figure 5.12 Grid section for metal flow study	128
Figure 5.13 Metal flow in different section extrusions at different stages.....	129
Figure 5.14 Metal flow near and at the billet surface for T-section.....	130
Figure 5.15 Comparison of the calculation of S_V using and (a) simplified plane strain cubic model and (b) tetrakaidecahedron model	133
Figure 5.16 Density of recrystallisation nuclei	133
Figure 5.17 Subgrain size distribution (μm)	135
Figure 5.18 Misorientation results using differential equations.....	137
Figure 5.19 Dislocation density and subgrain size using Holt relation.....	138
Figure 5.20 The stored energy, P_D , distribution (N/m^2).....	139
Figure 5.21 Predicted volume fraction recrystallised, X_V	141

Figure 5.22 Microstructures in the transverse plane of a solution soaked T-section extrudate (Subramaniyan 1989, p.131)	143
Figure 5.23 Predicted recrystallised grain size (μm).....	144
Figure 5.24 Recrystallised grain of the extrudate after 500°C solutionising followed by water quench (Subramaniyan 1989, p.162)	145
Figure 6.1 A typical tooling arrangement for aluminium hollow sections (Sheppard 1999a, p.359).....	147
Figure 6.2 Comparison between predicted and experimental stress	149
Figure 6.3 Top view of the bridge die	150
Figure 6.4 The one-sixth FEM model for tube simulation.....	150
Figure 6.5 Load evolution with ram displacement of tube extrusion.....	151
Figure 6.6 Deformed billet at different key points.....	153
Figure 6.7 Temperature evolution during tube extrusion ($^{\circ}C$).....	154
Figure 6.8 Strain distribution of tube extrusion	156
Figure 6.9 Gridded planes and their positions in the billet	157
Figure 6.10 Metal flow on the symmetry planes in tube extrusion.....	157
Figure 6.11 Comparison between (a) experimental result (Nisaratanaporn 1995, p.101) and (b) predicted metal flow in the welding chamber	159
Figure 6.12 Flow patterns that are not on the symmetry planes in tube extrusion	160
Figure 6.13 Positions of ten cylindrical surfaces inside the billet.....	161
Figure 6.14 Metal flow of surfaces coaxial with the billet surface	162
Figure 6.15 DMZs in tube extrusion (mm/s) shown (a) in filled contours (b) in iso-surfaces.....	163
Figure 6.16 Strain-rate distribution in tube extrusion (s^{-1}).....	167
Figure 6.17 Mean stress distribution of tube extrusion (MPa)	168
Figure 6.18 Effective stress distribution of tube extrusion (MPa).....	169
Figure 6.19 Weld quality index	169
Figure 6.20 A self-contact example by Ansys [®] (Ansys 2010).....	170
Figure 6.21 FEM model of penetrated mesh on welding surface before and after mesh repairing: (a) mutual penetration meshes on welding surfaces; (b) before mesh repairing; (c) after mesh repairing (Huang <i>et al.</i> 2010).....	172
Figure 6.22 One-third model of the tube extrusion.....	173

Figure 6.23 Metal flow of two neighbouring streams at the ram displacements of (a) 27 (b) 28 (c) 29 (d) 30 (e) 31 (f) 34 mm in the self-contact model.....	174
Figure 6.24 Load evolution versus ram displacement using one-third model	175
Figure 6.25 Temperature distribution at the ram displacement of 40mm (a) one-third model and (b) one-sixth model	176
Figure 6.26 Equivalent strain distribution at the ram displacement of 40mm (a) one-third model and (b) one-sixth model.....	176
Figure 6.27 The weld and non weld areas (Nisaratanaporn 1995, p.149).....	177
Figure 6.28 Microstructure of tube extrudate (as extruded, transverse section, I/D=4mm, O/D=16mm) (Nisaratanaporn 1995, p.151-153) (a),(b) at the tube outer surface, (c),(d) at the mid-radius area, (e) and (f) at the tube inner surface.....	178
Figure 10.1 Grain shape (a) cube before deformation (b) block after deformation	195
Figure 12.1 The bridge die used in the experiment (Nisaratanaporn 1995, p.74)	199
Figure 12.2 The dimensions of the die used in the study (Nisaratanaporn 1995, p.74).....	200
Figure 13.1 $\ln \epsilon$ against $\ln \sigma$	203
Figure 13.2 $\ln \epsilon$ against σ	203

List of Tables

Table 2.1 Constants for the equation (2.14)	44
Table 3.1 Basic element shapes.....	61
Table 4.1 Chemical compositions (wt%) of cast alloy AA2024.....	77
Table 5.1 Mobilities of high and low angle grain boundaries.....	101
Table 5.2 Estimation of the migration parameters at 280°C.....	102
Table 5.3 Experimental parameters and results	119
Table 5.4 Predicted load results vs. experimental measurements	122
Table 5.5 Peripheral ratios for different sections	123
Table 5.6 Predicted X_V vs. experimental measurements.....	142
Table 6.1 Chemical composition (wt%) of the AA6063 alloy (Sheppard <i>et al.</i> 1998)	148
Table 6.2 Flow stress at different temperature and different strain rate Akeret's experiment (1978)	149
Table 6.3 Distances from the billet surface of the 10 cylindrical surfaces	161
Table 13.1 Flow stress at different temperature and different strain rate Akeret's experiment (1978)	201

Acknowledgement

This PhD journey has certainly been a learning experience, and there are many people who have had an impact on me in one way or another. There are so many people that deserve a ‘thank you’ here, so don’t feel offended if your name is not mentioned. More importantly, this list is not ordered by importance.

I would like to express my deepest gratitude to Professor Terry Sheppard, my major supervisor, for his supervision, guidance and encouragement throughout various stages of this thesis. I really appreciated the numerous conversations which improved my professional knowledge and at the same time were quite humorous.

Heartfelt thanks go to Dr. Xavier Velay who is my second supervisor for his continuous assistance and illuminating instructions during the production of this thesis.

Professor Terry Sheppard and Dr. Xavier Velay certainly made my stay at Bournemouth a most enjoyable experience.

The help from Mr. Kjell Nilsen for offering a shop-floor visit to Boal Aluminium and the permission from Mr. Russell Wade to use the computing facilities are much appreciated.

I also extend my regards and blessings to all of those who supported me in any respect during the completion of the thesis.

My great tribute is due to my parents and parents-in-law for their loving considerations and invariable support through my long student life.

This work is dedicated to my dear wife, Yang Zhang, without her love and support I could not have attempted this thesis. It is also dedicated to my lovely son whom I haven’t yet held in my arms. I don’t know how much I owe him but I will do as much as possible to make him up after the thesis has been written.

Author's Declaration

The work contained in this thesis is the result of my own investigations and has not been accepted or concurrently submitted in candidature for any other award.

1. Introduction

1.1 Aluminium alloys and aluminium extrusion process

Aluminium, the second most plentiful metallic element on earth, constitutes some eight per cent of the earth's crust. Besides good mechanical properties, aluminium and its alloys also have good physical properties, such as low density, high corrosion resistance, good electrical and thermal conductivity. Thanks to this unique combination of properties, aluminium and its alloys offer a wide range of applications in engineering.

All aluminium production is based on the Hall-Heroult process. Alumina refined from bauxite is dissolved in a cryolite bath with various fluoride salt additions made to control bath temperature, density, resistivity, and alumina solubility. An electrical current is then passed through the bath to electrolyse the dissolved alumina with oxygen forming at and reacting with the carbon anode, and aluminium collecting as a metal pad at the cathode. The separated metal is periodically removed by siphon or vacuum methods into crucibles, which are then transferred to casting facilities where remelt or fabricating ingots are produced.

By careful control of alloying elements, an array of commercially available aluminium alloys can be produced. These aluminium alloys fall into two main groups, according to their suitability to specific manufacturing processes, casting alloys and wrought alloys. Based on whether they can be hardened by heat treatment or not, aluminium alloys can be classified into another two categories: heat or non-heat treatable alloys.

In terms of chemical composition, wrought aluminium alloys further are divided into eight series as follows:

- 1xxx aluminium of 99% purity, excellent corrosion resistance with high

thermal and electrical conductivity,

- 2xxx aluminium and copper, silicon alloys, high strength-to-weight ratio,
- 3xxx aluminium and manganese alloys, medium strength,
- 4xxx aluminium and silicon alloys, lower melting point, good melting characteristics,
- 5xxx aluminium and magnesium alloys, good corrosion resistance, high strength,
- 6xxx aluminium, magnesium and silicon alloys, good formability, machinability, weldability,
- 7xxx aluminium, zinc and magnesium alloys, moderate to very high strength.
- 8xxx alloys including tin and some lithium for airframe and auto locomotive components that have densities 7 to 12% lower and stiffnesses 15 to 20% higher than existing high-strength aluminium alloys.

The two basic types of extrusion are direct and indirect which are commonly used in aluminium extrusion industries as shown in Figure 1.1. In direct extrusion the direction of the metal flow is the same direction as ram travel while for the indirect extrusion the material flow to the opposite direction of the ram movement. Indirect extrusion is characterised by the absence of friction between the container and the billet surface whether the movement is both the billet and container moving relative to the stationary die or the die moving along the stationary container.

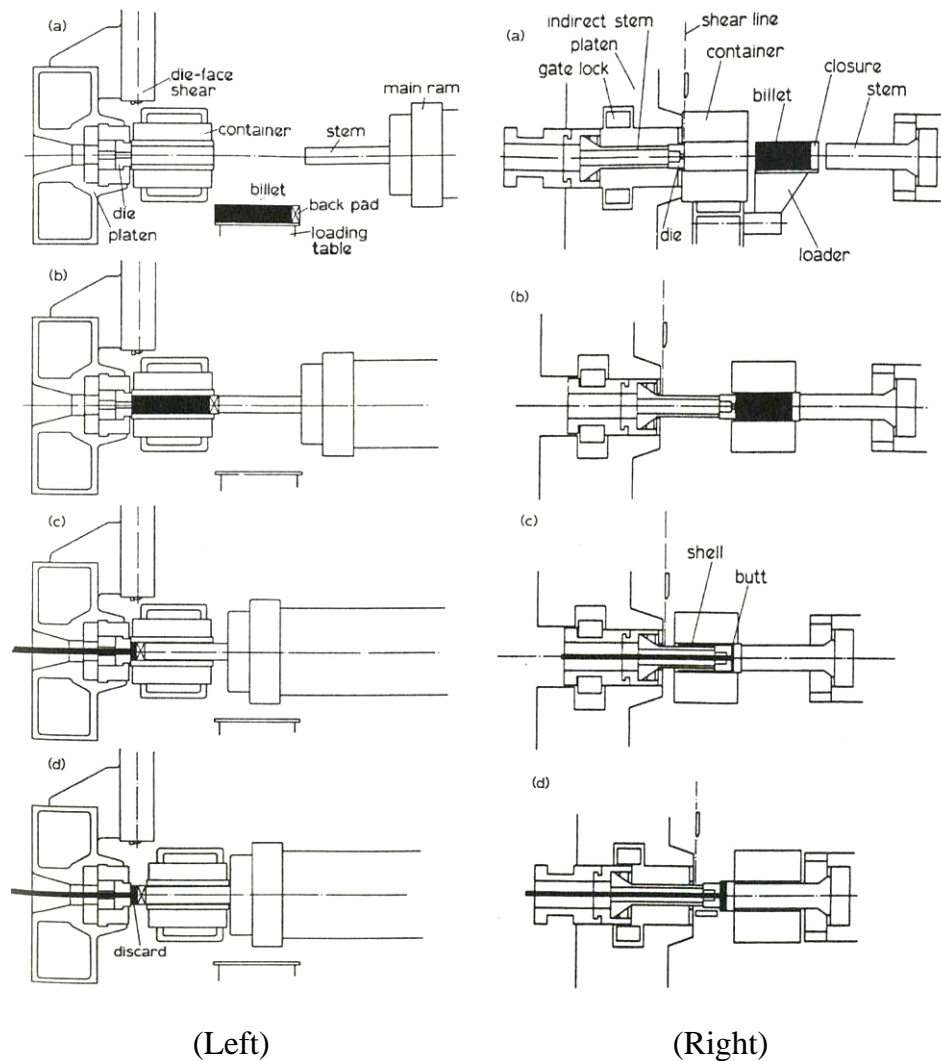


Figure 1.1 (left) Direct and (right) indirect extrusion layout (Sheppard 1999a, p.9)

The differences between direct and indirect extrusions have been extensively studied in the literature (Niu *et al.* 2008; Paterson 1981; Sheppard 1984; Sheppard and S.J. Paterson 1982; Valberg and Loeken 1992). It is well accepted that the major difference is that in the indirect process there is no friction between the billet and container whereas in the direct process the outer shell of the billet moves relative to the container as extrusion proceeds, thus considerable friction is generated.

Despite the advantages such as lower peak load, high productivity, better surface

quality, extended service life of tools and uniform deformed extrudate, limiting factors such as pre-machining of billet, limitation placed on the cross-section by die design and difficulties for rapid press quenching prevent the indirect mode from wider use in the aluminium extrusion industry.

Historically, mechanical working has been used as the primary means of changing the size and shape of materials while transforming the cast structure of an ingot into what is generally referred to as a wrought product. Extrusion is one of the major processes by which this has been achieved (Sheppard 1999a. p.6). It has been a dominant process to produce complex shape products in the aluminium industry.

Typical steps for an aluminium extrusion process cycle are:

- 1) Homogenisation of the direct-chill cast billet;
- 2) Loading die holder and die;
- 3) Preheating dies and container;
- 4) Loading the homogenised billet into the heated container;
- 5) Extrusion of the billet;
- 6) Decompression of the press and opening of the container;
- 7) Shearing the billet to obtain the discard or to prepare for the next extrusion in case of indirect extrusion;
- 8) Returning the shear, container and ram to the loading position;
- 9) Necessary temper designations for extruded products.

In principle, aluminium extrusion is a plastic deformation process during which a heated and homogenised billet in a preheated container is forced by compression to flow through a shaped die opening of a smaller cross-section to achieve the final desired profile and structure.

1.2 Modelling of extrusion process

The use of modelling opens up great opportunities for making maximum use of sparse process data, for optimum co-selection of material and process, and for providing the designer with feedback on the likely influence of processing on the viability and cost of a design as well as indicating trial processing parameters (Shercliff and Lovatt 2001). In their work, ‘modelling is interpreted in its widest sense: from empirical rules and curve fits, to advanced statistical methods such as neural networks, to physically-based process models’.

Hill (1950) developed the elastic-plastic analysis. Then by assuming convenient boundary condition he put forward the slip line field analysis and indicated that it may be possible to create a much quicker method which turned out to be the ‘Upper Bound’ method: described in his classical book. From this Johnson and Kudo (1962) developed the Upper Bound approach. Subsequently the approach was applied to most of the suitable problems by a number of workers. This theory suffers from two major setbacks: it is two dimensional and the effect of temperature is difficult to implement. After this many authors were successful in adapting this technique to various problems but none were really successful when the problem was three dimensional and temperature dependent. At the beginning of the 1950’s J. H. Argyris and Oleg C. Zienkiewicz at Imperial College commenced to publish their work on Finite Element Method (FEM) (Zienkiewicz *et al.* 2005, p.2-3). By the early 80’s most engineering problems could be solved by these methods and they continued to develop until the early 90’s several commercial programs appeared specifically to deal with thermo-plastic problems. These are now available to the scientific community.

Bianchi and Sheppard (1987) were among the pioneers of applying FEM to extrusion calculation. So far process modelling has gained considerable impetus over the past few decades with the rapid increase in computational power. It has

been mainly driven by industry to increase output with lower cost and better quality. Industrial modelling activity in metals and alloys extends to virtually every process from primary refining and casting processes through forming to fabrication and heat treatment (Grong and Shercliff 2002).

A complete analytical resolution of the extrusion process is presently impossible because of the complexities of the metal forming processes: large deformation, thermo-mechanically coupled, nonlinear boundary conditions and nonlinear material behaviour. Currently there are no other methods that are as convenient as the Finite Element Method (FEM) to approach all of these problems with the necessary precision. A large amount of work in the modelling and simulation of aluminium extrusion processes by the use of finite element software has been undertaken in the last few decades. The applications involve nearly every aspect of the extrusion process: predict load, temperature, material flow, surface formation, surface cracks, recrystallisation and die wear (Velay 2004, p.27). The main advantages of FEM, compared with other numerical methods and analytical techniques are:

- Predict the deformation information such as strain, stress, temperature, velocity;
- Consider the complex interactions between strain, strain rate, temperature, microstructure, and the flow stress;
- Use very realistic models to represent real process behaviour, such as the coefficients of friction and heat transfer coefficients;
- Visualise the deformation process with the ability to trace the history after solution of the problem.

The ultimate goal of FEM software is to replace the experimental phase partially or completely. For this reason a number of programmes modified to deal with deformation processes have become available commercially.

1.3 Objective of this research

The research will focus on using FEM to model the hot extrusion of certain aluminium alloys of different profiles. Since modelling of simple sections such as rod, square have been extensively studied (Duan *et al.* 2004; Flitta and Sheppard 2003; Sheppard 1993; Sheppard and Duan 2002; Sheppard and S.J. Paterson 1982), focus will be concentrated on the modelling and simulation of section extrusions having more complex profiles such as T-shape (solid section) and tubular shape (hollow section). Therefore the research objectives are as follows:

- 1) Validate the FEM code with rod simulation;
- 2) Investigate and develop suitable constitutive equations;
- 3) Predict the extrusion pressure, temperature distribution and evolution;
- 4) Predict the metal flow and surface generation during extrusion;
- 5) Develop microstructure evolution model during extrusion using state variables (subgrain size, misorientation, and dislocation density);
- 6) Develop the subroutines to integrate the microstructure evolution model into FE code through the FE code's subroutine interface.

For hollow profiles, special attention will be paid to the formation of the welding seams and related parameters.

Thus the contribution to knowledge lies in the ability to describe the evolution of subgrains, dislocation density distribution during the process; the ability to use these parameters to predict microstructure both in heat treated and in non-heat treated stock is also novel and of some importance. The reader should be aware that predicting the microstructure is necessary to ensure that suitable properties are obtained in the extrudate.

2. Literature review

2.1 Numerical modelling and simulation of aluminium extrusion

2.1.1 Introduction

The term ‘modelling’ has two meanings: one falls into the domain of model formulation or model design. The second often-encountered meaning of modelling is the numerical solution of the governing equations associated with models. This procedure can be referred to as "numerical modelling" or "simulation". Both terms paraphrase the solution of a set of mathematical expressions, i.e., of a number of path-dependent and path-independent functions, which quantify the underlying model formulation using appropriate boundary and initial-value conditions. Although both numerical modelling and simulation basically address the same activity, they are often used in a somewhat different fashion. One common approach is to use the notion "numerical modelling" for the entire procedure of model formulation and program code generation, while the term "simulation" is often used in the sense of numerical experimentation. In this picture, modelling comprises the entire phenomenological, theoretical, and conceptual work including programming, while simulation describes the mere application of the program under conditions that map essential parameters of real processes, i.e. under different boundary and initial-value conditions (Raabe 1998, p.20).

The application of numerical techniques to the continuum mechanics problem, developed over the past several decades, has improved the capability for an integrated treatment of both tool-load demands and internal micromechanics. Their implementation as computer codes, with thermo-mechanical balance and kinematics compatibility built in, has introduced a modelling tool driven only by the external boundary conditions and the material behaviour. The Finite Element Method now provides sufficient information for many “mechanical” problems, such as load prediction, speed optimisation, temperature and residual stress, etc.

Whilst most of the early finite element methods used in computational science postulated isotropic, homogeneous, linear, and continuous materials properties (Zienkiewicz *et al.* 1990), a number of advanced methods consider material heterogeneity, crystal anisotropy, nonlinear material response, and nonlinear geometrical aspects.

Figure 2.1 shows the procedure of a numerical modelling process, in which after the physical model is described with mathematical model, the real problem would be reformulated in discrete terms, as a finite set of algebraic equations, which are more suitable than a set of Partial Differential Equations (PDEs) to the number-manipulating capabilities of present-day computing machines. If this discretisation step is made by starting from the mathematical problem in terms of partial differential equations, the resulting procedures can logically be called numerical methods for partial differential equations. This is indeed how the Finite Difference (FD), Finite Element (FE), Finite Volume (FV), and many other methods are often categorised. Finally, the system of algebraic equations produced by the discretisation step is solved, and the result is interpreted from the point of view of the original physical problem (Mattiussi and Peter 2002).

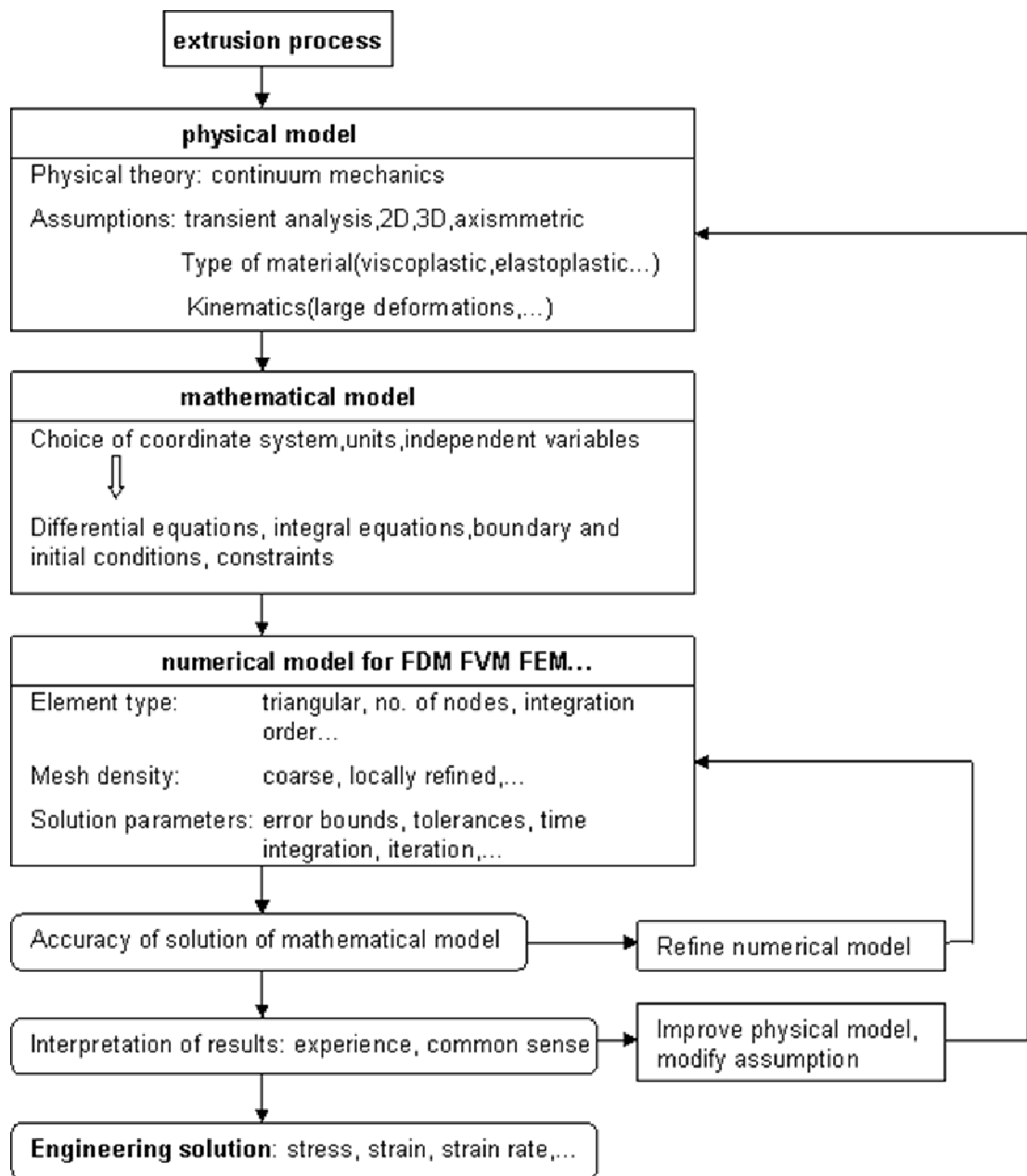


Figure 2.1 Procedure for numerical modelling (Bograd 2004)

2.2 Numerical methods used for bulk metal forming modelling

There are three most popular discretisation methods used for the governing equation: Finite Difference Method (FDM), Finite Volume Method (FVM) and Finite Element Method (FEM).

An FDM discretisation is based upon the differential form of the PDE to be solved. Each derivative is replaced with an approximate difference formula (that can generally be derived from a Taylor series expansion). The computational domain is usually divided into hexahedral cells (the grid), and the solution will be obtained at each nodal point. The FDM is the easiest to understand when the physical grid is Cartesian, but through the use of curvilinear transforms the method can be extended to domains that are not easily represented by brick-shaped elements. The discretisation results in a system of equations of the variable at nodal points. Once a solution is found, a discrete representation of the solution is obtained.

An FVM discretisation is based upon an integral form of the Partial Differential Equation (PDE) to be solved (e.g. conservation of mass, momentum, or energy). The PDE is written in a form which can be solved for a given finite volume (or cell). The computational domain is discretised into finite volumes and then for every volume the governing equations are solved. The resulting system of equations usually involves fluxes of the conserved variable, and thus the calculation of fluxes is very important in FVM. The basic advantage compared to FDM is that it does not require the use of structured grids, and the effort to convert the given mesh into structured numerical grid internally is completely avoided. As with FDM, the resulting approximate solution is discrete, but the variables are typically placed at cell centres rather than at nodal points. This is not always true, as there are also face-centred finite volume methods. In any case, the values of field variables at non-storage locations (e.g. vertices) are obtained using interpolation.

An FEM discretisation is based upon a piecewise representation of the solution in terms of specified basis functions. The computational domain is divided up into smaller domains (finite elements) and the solution in each element is constructed from the basis functions. The actual equations that are solved are typically obtained by restating the conservation equation in weak form: the field variables are written in terms of the basis functions, the equation is multiplied by appropriate test functions, and then integrated over an element. Since the FEM solution is in terms of specific basis functions, a great deal more is known about the solution than for either FDM or FVM. This can be rather pragmatic because the choice of basis functions is very important and boundary conditions may be more difficult to formulate. Again, a system of equations is obtained (usually for nodal values) which must be solved to obtain a solution (CFD_Online 2008).

Since the creation of these methods arguments about which represents the most efficient numerical modelling and simulation have never ceased (Bianchi and Sheppard 1987; Blazek 2001, p.37-39; Chung 2002, p.26; Cubric *et al.* 1999; Ferziger and Peric 2002, p.35-37; Mattiussi and Peter 2002). Comparison of the three methods is difficult, primarily due to many variations of all three methods. However, generally speaking:

FDM

- Easy to program and possible to obtain higher order accuracy of the spatial discretisation;
- The simplicity of discretisation using structured grid;
- The poor capacity in representation of complex geometry.

FVM

- Better conservation properties;
- Easiness for programming like FDM;
- Complex geometries and unstructured meshes are easily accommodated;
- The disadvantage of FVM compared to FD schemes is that methods of order higher than second are more difficult to develop in 3D problem.

FEM

- Higher order of accuracy is easier to be realised compared to FVM;
- Complex geometries and unstructured meshes are easily accommodated;
- Underlying principles and formulations require mathematical rigor and its realisation of programming is complex, hence calculation efficiency is low.

In sum, although opinions vary, the finite difference method (and its finite volume counterparts) is used widely in Computational Fluid Dynamics (CFD). The main reason is that a fluid is better modelled in an Eulerian frame. The general ease of FEM in handling boundary conditions, as compared to FDM and better working with a Lagrangian framework to accurately track free surface makes it powerful and dominant in metal forming modelling. And its low calculation efficiency is not a formidable problem anymore because of huge advances in PC hardwares.

The FEM software FORGE2009[®] that is developed by Transvalor, a French company, and incorporates Forge2[®] and Forge3[®] is selected to be used in this research, because it has the ability to simulate thermo-mechanically coupled large deformation both in 2D and 3D, to re-mesh the FEM model automatically, to calculate the evolving contact and frictional interfaces and complicated temperature evolution, and most importantly, its user-subroutine interface offers users more flexibilities to incorporate their own material and structural evolution models into it.

The procedure for a finite element analysis (FEA) has been well established and can be seen in many books (Reddy 2006; Zienkiewicz *et al.* 2005). Reddy (2006, p.105) summarised the basic steps of an FEA can be as follows:

- 1) Discretisation (or representation) of the given domain into a collection of preselected finite elements (This step can be postponed until the finite element formulation of the equation is completed);
- 2) Derivation of element equations for all typical elements in the mesh;
- 3) Assembly of element equations to obtain the equations of the whole problem;
- 4) Imposition of the boundary conditions of the problem;
- 5) Solution of the assembled equations;
- 6) Postprocessing of the results.

2.3 Main parameters established by experiment (empiricism)

2.3.1 Extrusion ratio

In conventional extrusion the extrusion ratio R is defined as:

$$R = \frac{A_C}{A_B} \quad (2.1)$$

where A_C is the area of the container cross section, A_B is the cross sectional area of the extrudate.

2.3.2 Plastic strain and strain rate

The effective strain, $\bar{\epsilon}$, obtained by integration is a logarithmic function. Therefore, the effective strain in direct extrusion is usually approximated as the fractional sectional area and is defined in an elementary notation as:

$$\bar{\epsilon} = \ln \frac{A_C}{A_B} = \ln R \quad (2.2)$$

which ignores any inhomogeneity on the extrudate section.

The rate of straining is also an important parameter and very difficult to determine due to the complex flow pattern in the deformation zone. The material undergoes a rapid acceleration as it passes through the deformation zone. Therefore a mean equivalent strain rate, $\dot{\bar{\epsilon}}$, is useful both for preliminary determination of the flow stress and a rapid way to determine possible limit of the equipment. After extensive optimisation of the upper bound solution, Castle and Sheppard (1976a) and Tutcher (1979) suggested the following equation for the mean equivalent strain rate

$$\dot{\bar{\epsilon}} = \frac{6D_C^2 V_R (a + b \ln R) (c + d \tan \omega)}{D_C^3 - D_E^3} \quad (2.3)$$

where a, b, c and d are constants, D_C is the container diameter, D_E is the extrudate diameter, V_R is the ram speed and ω is the semi-angle of the deformation cone. Of

course more accurate calculation may be obtained when using FEM.

2.3.3 Friction

Generally hot extrusion of aluminium alloys is performed without lubricants. However a small amount of graphite based grease is sometimes used on the face of the die and dummy block. This is because the surface is a very important feature of the product and is formed from the interior of the billet by the shear occurring in the conical zone adjacent to the die known as the dead metal zone (Sheppard 1999a, p.10).

Friction in aluminium extrusion is a complex and still not fully understood phenomenon (Nakamura *et al.* 1997; Nakamura *et al.* 2003; Schikorra *et al.* 2007; Wagener and Wolf 1994). The environment of hot extrusion (i.e. high pressure, high temperature and complicated material flow) prevents efficient investigation of the frictional interfaces.

In direct extrusion (with a flat die) the friction occurs at four interfaces: (a) container-billet, (b) die bearing-material, (c) dead metal zone-material, and (d) dummy block-billet. In indirect extrusion there is a similar upsetting stage in the beginning as in direct extrusion whilst there is no friction on the container-billet surface during the extrusion process because of the lack of relative movement between them. On the other three interfaces frictions still exist.

At commencement of extrusion the ram contacts the billet interface producing a frictional force at that location. Further ram travel upsets the billet into the container and the billet surfaces make first contact only at the highest points of the billet surface. Subsequently due to increasing pressure the contact area is increased. The high points start to deform and the concentrated mechanical energy required to overcome frictional resistance is converted into heat energy. This eventually

leads to sticking friction between the container and the billet and extrusion proceeds by shearing along the container wall. The thickness of the shearing layer was calculated as of an order of 40-100 μm (Jowett *et al.* 2000; Sheppard 1999a, p.49). At the bearing-extrudate interface friction in the die land can further increase the extrudate's temperature, which contributes to the surface quality of the extrusion (Peng and Sheppard 2004; Saha 2004). This temperature change is also one of the influencing factors for recrystallisation in the extrudate. At the dead metal zone-material the material experiences intermetallic friction that defines the dead metal zone semi-angle (Saha 2000, p.8). Due to the relatively small flow of material and the shearing of the discard, the dummy block-billet surface does not significantly influence the extrudate quality.

2.3.4 Extrusion pressure

Since the first attempt based on the assumption of uniform deformation by Siebel and Fangmeir (Sheppard 1999a, p.29) the study of pressure during aluminium extrusion has been extensively reported (Flitta and Sheppard 2002; Jo *et al.* 2003; Lou *et al.* 2008). The pressure required for the process is the principal consideration in the selection of an extrusion press. The pressure can vary depending on: the alloy and its condition, the extrusion ratio, diameter and length of the billet, initial temperatures of the billet and tooling, ram speed and the shape of the extrudate (Castle and Sheppard 1976b; Sheppard 1993; Sheppard 1999a, p.143-144; Sheppard and Wood 1980).

2.3.5 Heat transfer and temperature

Heat transfer is one of the most the important phenomena to consider in extrusion as it defines the temperature parameter. This is one of the process variables which should be controlled. Temperature rise and distribution have been investigated by many researchers (Duan and Sheppard 2002a; Libura *et al.* 2000; Lou *et al.* 2008;

Mollerbernd *et al.* 1996; Zasadzinskii and Misiolek 1988). In general it has been shown that variations in temperature are mainly due to the extrusion ratio and ram speed. The flow stress and therefore the pressure will be reduced if the temperature is increased. However there is a risk of localised incipient melting with high ram velocity.

Heat transfer occurs throughout the extrusion process from the initial stage of homogenisation to the following extrusion stage, during which heat transfers to the die (from the billet) and air (from the extrudate), until the stage of stretching and finally at the stage of solution treatment and ageing (Castle and Sheppard 1976b; Chenot *et al.* 1996; Sheppard and Wood 1980). The heat generation and heat transfer occurring during the extrusion are critical because they define the exit temperature of the extrudate. The temperature distribution over the extrudate leaving the die is important for product quality (dimensional stability, structural factors and extrusion defects) and die life (wear and performance). Castle (1992) and Sheppard (1999b) divided the heat balance between the following processes:

- Heat generation due to plastic deformation;
- Heat generation due to friction at the container-billet, dead metal zone-material and die land-material interfaces;
- Heat exchange between the billet and the tooling (container, pressure pad and die land).

Approximately 90-95% of the mechanical energy is transformed into heat. Therefore the heat generation rate per unit volume, \dot{Q}_d , can be written as follows:

$$\dot{Q}_d = \lambda \dot{\epsilon} \tag{2.4}$$

where λ is the heat generation efficiency ($0.90 \leq \lambda \leq 0.95$).

2.4 Constitutive laws used for hot working metal FEM simulation

2.4.1 Yield criterion

A yield criterion is a postulated mathematical expression of the states of stress that will cause yielding. It is expressed by

$$f(\sigma_{ij}) = C(\text{constant}) \quad (2.5)$$

where $f(\sigma_{ij})$ is known as the yield function and σ_{ij} is defined by the Cauchy stress tensor. For isotropic materials, such as aluminium alloys, plastic yielding can depend only on the magnitude of three principal stresses ($\sigma_1, \sigma_2, \sigma_3$) and not on their directions. Thus any yield criterion can be expressed as follows:

$$f(J_1, J_2, J_3) = C(\text{constant}) \quad (2.6)$$

where J_1, J_2, J_3 are the three invariants of the stress tensor, σ_{ij} . The first invariant, $J_1/3$, represents the hydrostatic pressure. Although this pressure may increase ductility it does not contribute to deformation. For ductile materials, two different criteria are generally used. The Tresca criterion, which postulates that yielding will occur when the largest shear stress reaches a critical value, and the Von Mises criterion which states that yielding will take place when the second invariant, J_2 , reaches a critical value. The Tresca criterion provides a practical approximation of yielding, however, the Von Mises criterion is usually preferred because it correlates better with experimental data.

2.4.2 Viscoplastic model

The theory of plasticity adequately describes materials with time-independent behaviour. However the theory of viscoplasticity more effectively defines the material behaviours which exhibits strain rate sensitivity such as in aluminium

alloys. During hot extrusion the aluminium alloys' properties will vary considerably with temperature. The workpiece (e.g. billet and extrudate) experiences temperature gradients. At elevated temperature, plastic deformation can induce phase transformations and modifications to grain structures. These metallurgical changes can, in turn, modify the flow stress of the material as well as other mechanical properties. Thus, the flow stress, $\bar{\sigma}$, can be expressed as a function of temperature, strain, strain rate, and state variables. At very high temperature ($< 0.9T_m$), where T_m is the melting point of the material, the influence of strain on flow stress is insignificant, and the influence of strain rate becomes increasingly important. Therefore $\bar{\sigma}$ can be expressed as follows:

$$\bar{\sigma} = f(\dot{\epsilon}, T, S_i, P_i) \quad (2.7)$$

where $\dot{\epsilon}$ is the mean equivalent strain rate, T is the temperature, S_i are the state variables such as grain and subgrains size, stacking fault energy (SFE) and thermomechanical history, P_i are the material properties invariant such as elastic modulus and the crystal structure.

Three constitutive equations, the Hansel-Spittle's model, the Norton Hoff law and the Zener-Hollomon formulation, have usually been adopted in the FEM simulations of hot forming. However among the three constitutive equations, the hyperbolic sine function (Zener-Hollomon formulation) is the only one revealing the physical nature of the flow stress (Sheppard 1999a, p.132-136; Sheppard and Jackson 1997), while the other two are purely empirical methods with the tuneable constants ensuring equation/experimental compatibility. Velay (2004) made an excellent comparative study of these three equations and their suitability for hot extrusion of aluminium alloys using FEM software Forge[®]. His results show that Zener-Hollomon formulation is the most accurate equation to represent the flow stress in hot extrusion of aluminium alloys in FEM simulation.

Thus the Zener-Hollomon formulation was adopted in this research. The hot deformation of aluminium alloys is commonly described by the equations shown below ((2.8), (2.9)). Initially proposed by Zener and Hollomon (1944), later modified by Sellars *et al.* (1972) and subsequently rearranged by Sheppard and Wright (1979b), the flow stress is written:

$$\bar{\sigma} = \frac{1}{\alpha} \ln \left\{ \left(\frac{Z}{A} \right)^{\frac{1}{n}} + \left[1 + \left(\frac{Z}{A} \right)^{\frac{2}{n}} \right]^{\frac{1}{2}} \right\} \quad (2.8)$$

or

$$Z = A[\sinh(\alpha\bar{\sigma})]^n \quad (2.9)$$

where the parameters are defined as follows:

α , A , n are constants. Garofalo (1963) showed that equation (2.8) reduces to a power law when $\alpha\bar{\sigma} < 0.8$, but approximates an exponential relationship when $\alpha\bar{\sigma} > 1.2$.

Z is the temperature compensated strain rate parameter also called the Zener-Hollomon parameter. It is given by equation (2.10) below:

$$Z = \dot{\epsilon} \exp\left(\frac{\Delta H}{GT}\right) \quad (2.10)$$

where T is the temperature, G is the universal gas constant ($8.31451 \text{ J} \cdot \text{mol}^{-1} \cdot \text{K}^{-1}$), and ΔH is the activation energy for hot deformation. Dorn (1957); Garofalo (1966) and Weertman (1968) have compiled a considerable body of data to demonstrate that the activation energy for creep for many metals including

aluminium increases with temperature up to $T \approx 0.5T_m$ whereupon it remains constant up to the melting point.

2.5 Thermal-mechanical process modelling using the Finite Element Method

The simulation of an extrusion sequence in an industrial environment consists principally of a thermo-mechanical analysis of the plastic deformation. The term thermodynamics refers to the study of heat related matter in motion. Modelling of thermo-mechanical processing of metals is one of a number of industrial modelling activities which has been reviewed in response to the technology foresight exercise (Shercliff 1997). The Finite Element Method is a general numerical means of obtaining approximate solutions in space to boundary and initial-value problems. It is based on generating the governing differential equations and the discrete algebraic counterparts of the problems under investigation using a variation formulation. The development of the state variable is approximated by appropriate interpolation functions. The application of numerical techniques to the continuum mechanics problem, developed over the last three decades has improved the capability for an integrated treatment of both tool-load demands and internal micromechanics.

Currently, computer modelling and simulation of the material forming process has been developed to the point where it may be used to solve industrial problems. Computer modelling is often treated as a universal tool in all problems of metal forming processes. Taking a general view of the present state of the art in terms of numerical modelling, it appears that the finite element method is most suited to the three-dimensional analysis of material forming processes. In fact the finite element method can take into account practical non-linearity in the geometry and material properties, as well as producing accurate predictions of stress, strain, strain rate and temperature throughout the deforming billet (Chanda *et al.* 2000; Chenot *et al.* 1996; Duan and Sheppard 2003b; Flitta *et al.* 2007; Peng and Sheppard 2004).

For many deformation processes, there is a view that continuum mechanics FEM is well established, both for simulating the manufacturing process itself and the less obvious task of modelling the ‘standard test’ used, for example, to determine constitutive behaviour (Huang 1998). The greatest limiting factors at the continuum level in all metal-forming analyses are poor characterisation of interfacial friction conditions (and to a lesser degree heat transfer), and the need for improved models of material constitutive behaviour for complex deformation histories and for heterogeneous materials (Marthinsen *et al.* 2003; Shercliff 1997).

2.6 Microstructure modelling

Observations of the structure developed by hot working have been made on a wide range of materials deformed either by forging, rolling, or extrusion, or by high torsion rate tension, compression, or torsion tests (Blum *et al.* 1996; McQueen and Blum 2000; Nes *et al.* 1994; Sheppard and Wright 1979a; Wright and Sheppard 1979; Zhu and Sellars 2001). In general, the results obtained using different modes of deformation are in good agreement and they indicate that there are two broad groups of metals and solid-solution alloys which may behave differently under hot working conditions. Aluminium and aluminium alloys, commercial-purity α -Fe and ferrite alloys are observed to develop subgrains during deformation when specimens are cooled rapidly after either small or large amounts of deformation. The structural changes during hot working of this group of metals are similar to those during creep, and where activation energies have been observed to remain nearly constant over the whole range of strain rates and temperature as previously mentioned.

The work in the present study concentrates on deformation of aluminium alloys in which dynamic recovery and static recrystallisation are the main restoration process. Since the beginning of the 1990’s, much progress has been made in computer modelling of microstructure evolution during the hot deformation

process. Excellent reviews of modelling of static recrystallisation (SRX) have been given by several researchers (Doherty *et al.* 1997; Humphreys and Hatherly 2004, p.507-524; Shercliff and Lovatt 1999). There are several approaches to modelling microstructure evolution in hot deformation and subsequent annealing, the most commonly used methods include: (a) empirical methods, (b) probabilistic methods, (c) physically based state variable methods.

2.6.1 Empirical models for structure prediction

The inherent complexity of bulk metal forming modelling calls for a degree of pragmatism, and hence in some cases purely empirical models have to be used. Extensive experimentation is used as a pragmatic and traditional approach to describe microstructure and to interpret the behaviour by empirical equations or graphs.

The established empirical approach to predict flow stress and subsequent recrystallisation is based on the Zener-Hollomon parameter (see equation (2.10)) (Shercliff and Lovatt 1999). Flow stress in the empirical approach study is commonly described by an equation in the form of

$$\sigma = \frac{1}{\alpha'} \operatorname{arcsinh} \left(\frac{Z}{Z^*} \right)^{1/n} \quad (2.11)$$

where α' , Z^* and n are material constants. Recrystallised grain size, d_{rex} , and the time to 50% recrystallisation, t_{50} (a common measure of recrystallisation kinetics), are described by power laws:

$$d_{rex} = k d_0^a \varepsilon^{-b} Z^c \quad (2.12)$$

$$t_{50} = \beta d_0^p \varepsilon^{-q} Z^{-r} \exp(Q_{def}/RT) \quad (2.13)$$

where β , k are constants, d_0 is the initial grain size, Q_{def} is an activation energy characteristic of the material, and ε is the Von Mises equivalent strain. The other parameters are all empirical constants (Shercliff and Lovatt 1999).

Other empirical models have been developed to describe:

(1) The relations between the subgrain size and recrystallised grain size to processing parameters.

On the finer scale, the extrudates contain a well recovered subgrain structure whose sizes are modified by the presence of the inclusion and precipitates. The subgrain size is commonly given as reported in a considerable volume of literature (Paterson 1981; Sellars 1990; Sheppard and Titcher 1980) as:

$$\delta^{-1} = A \ln Z + B \quad (2.14)$$

in which constants A and B have been given for various aluminium alloys for different forming process that are shown in Table 2.1.

Material	A	B	Process	Reference
AA1100	0.0153	-0.196	Rolling	(Zaidi and Sheppard 1982)
AA2014	0.096	-0.1747	Direct extrusion	(Vierod 1983)
AA2014	0.085	-1.586	Indirect extrusion	(Vierod 1983)
AA2024	0.0378	-0.5778	Direct extrusion	(Subramaniyan 1989)
AA2024	0.0426	-0.6457	Indirect extrusion	(Subramaniyan 1989)
AA7075	0.023	-0.54	Direct extrusion	(Dashwood <i>et al.</i> 1996)

Table 2.1 Constants for the equation (2.14)

Empirical equations were also given to relate the recrystallised grain size to the deformation conditions (Nes *et al.* 1994). Empirical models have been combined with FEM to predict the final structure in rolling in previous studies (Duan and Sheppard 2002a; Duan and Sheppard 2003b; Herba and McQueen 2004)

(2) Volume fraction recrystallised factor

the volume fraction X_V of a material which recrystallises in a time t during isothermal annealing produces a curve of sigmoidal shape as reported by Sheppard and Raghunathan (1989). It is consistent with the recovery, nucleation, and growth equation proposed by Avrami (1939, 1940, 1941) which takes the form:

$$X_V = 1 - \exp(-\beta t^n) \quad (2.15)$$

where β and n are constants for any fixed time and temperature conditions. Rearranging this equation yields:

$$\ln\left(\ln\left(\frac{1}{1-X_V}\right)\right) = \ln\beta + n \ln t \quad (2.16)$$

By empirical means, a modest degree of prediction of microstructure can be achieved by linking recrystallisation after deformation to the average process conditions. While at present this empirical methodology is applied with moderate success in industrial practice, the range of applicability and the accuracy of such predictions are limited due to the empirical nature of the microstructure models employed. Firstly, these empirical models do not disclose the underlying physical mechanisms of the microstructure evolution. Their applicability is confined within the boundaries in which they were obtained and hence they do not offer universal prediction capabilities. Secondly, they are usually of simple forms, while more complicated microstructural phenomena cannot be fully described using such equations.

2.6.2 Probabilistic (statistical) methods and neural network method

Monte Carlo (MC) and Cellular Automata (CA) techniques are two well known

probabilistic methods.

Computer simulation of grain growth and recrystallisation was in the early 1980's when it was realised that MC models could be applied to problems of grain structure evolution while the simulation of recrystallisation by the CA method was reported as early as 1990's (Hesselbarth and Gobel 1991).

Monte-Carlo simulation is based on the fact that the microstructure is developed by growth of nucleated sites during recrystallisation. Stored energy is assigned to all sites within those grains. By varying the stored energy within the grain heterogeneous nucleation rates can be simulated. In the CA method, each cell of the lattice represents a group of atoms, and the movement of individual cells acting in response to their neighbourhood describes the microstructure evolution (Chopard and Droz 1999). Cells of CA are characterised by certain attributes through which the 'state' of the cell is determined. These attributes are variables corresponding to the thermo-mechanical process. CA has been proved successful for simulating grain structure in casting, with close coupling with both a thermal finite element computation and the progressive solidification behaviour (Gandin and Rappaz 1994). More recently some researchers began to predict microstructure evolution by coupling CA with FEM both in hot working and the progressive solidification behaviour (Das *et al.* 2007; Guillemot *et al.* 2007; Sheppard and Velay 2007). However, the main problem in the CA and MC methods is the limitation of their scale of application. That is, only a small number of grains can be simulated due to the drawback that CA involves extremely intensive computation. This kind of simulation of microstructure behaviour of a few grains usually is not sufficient to describe the material behaviour in more macroscopic circumstances. Besides, the problems that have yet to be resolved are the quantification of grain boundary migration velocity and the definition of the transient rules which determine the state of the cell in the next time step depending on the current cell state, which affects the model's ability to predict the fraction

recrystallised. Although both models have been developed extensively in the last decade and various hybrid models have been provided, difficulty still remains in applying the two methods without arbitrary interference by the user.

2.6.3 Neural network method

The reliability of the artificial neural network method still depends on the availability of extensive, high quality experimental data, but this method offers great potential to link processing parameters, composition and properties. Examples of the application of artificial network method to predict microstructure evolutions are continuous cooling transformation (CCT) diagram modelling after hot working (Dobrzanski and Trzaska 2004; Wei *et al.* 2007) and recrystallisation (Korczak *et al.* 1998; Lin *et al.*). This approach offers much more to the field than traditional empirical approaches since large number of input variables can be handled (including composition) and the embedded function mapping between input and output could be highly complex and non-linear. Microstructure may be incorporated explicitly if appropriate, either as input parameters or as the target output of the model. These new approaches are regarded with deep suspicion by some physical metallurgists, since they offer no physical insight. They may, however, prove of great value for identifying underlying trends in complex multi-parameter data-sets, reducing the quantity of experimentation needed, or for testing hypotheses reached from a physically-based approach (Grong and Shercliff 2002).

2.6.4 Physically-based internal variable methods

2.6.4.1 Introduction

Microstructure modelling has long been an important task of physical metallurgist. However the complexity of industrial processing of commercial alloys had entailed the above-mentioned empirical methods and physically-based modelling

with idealised alloys under controlled laboratory conditions. Until recently the great improvement of computation power, in particular the development of the Finite Element Method (FEM) and its application into metals processing made it possible that microstructural modelling could be integrated with modern Finite Element Analysis (FEA) and the results with considerable details can be extracted.

Theoretical modelling has long been an integral part of physical metallurgy applied to thermal or thermomechanical processing. This applies both to the evolution of microstructure with time or strain, and the dependence of properties on microstructure. Microstructural models attempt to describe the underlying phenomena in terms of a small number of identifiable microstructural features (or ‘internal state variables’) (Grong and Shercliff 2002). Since it is widely acknowledged that a physically-based internal state variables method can gain more confidence than an empirical approach in terms of predicting the metal behaviours under conditions that have not been experimentally studied, quite a amount of work has been done in this field (Carron *et al.* 2010; Chen *et al.* 1991; Duan and Sheppard 2001; Flitta *et al.* 2007; McLaren and Sellars 1992; Talamantes-Silva *et al.* 2009; Zhu *et al.* 2003).

2.6.4.2 The internal state variable formalism

Because the process conditions inevitably vary during industrial processing of metals, the internal state variable method was originally proposed to model the non-isothermal transformation behaviour. If the phenomena of the microstructure evolution can be represented in the form of some differential equations about the state variables variation with respect to time, then using some appropriate numerical codes that have been developed commercially and available easily at present, the process history, in principle, can be represented by these state variables whose values are calculated by integrating step-wise throughout the process.

Modelling of microstructure evolution explicitly in differential form has been the basis for most classical theories of work hardening and annealing. The internal state variables are now physically meaningful quantities that can, at least in principle, be measured by electron microscopy (dislocation density etc.). developments of this approach can now benefit from the recent advances in microscopy, such as semiautomatic Electron Back Scatter Diffraction (EBSD), which enables substructures to be quantified with far greater speed and precision (Hurley and Humphreys 2003a, 2003b). Differential physically based state variable models have the potential to follow complex process histories and provide a means of conveying microstructure explicitly from one processing stage to the next.

Physically-based internal state variable models have been reported extensively by these research groups (Nes *et al* at the Norwegian University of Science and Technology in Trondheim, Sellars *et al* at the University of Sheffield, UK and Sheppard's group at Bournemouth University, UK, after establishment at Imperial College, UK). There are three separate modelling tasks: (a) describing the evolution of the deformation substructure, in particular the subgrain size, dislocation density and subgrain boundary misorientation; (b) relating substructure parameters to flow stress; and (c) predicting recrystallisation behaviour.

The Trondheim group have proposed and further developed a three-parameter approach to model the metal plasticity (Marthinsen and Nes 1997, 2001; Nes 1997; Nes and Marthinsen 2002; Nes *et al.* 2000). Their result was concluded as a work hardening model during plastic deformation of FCC metals and alloys. Based on a statistical approach to the problem of athermal storage of dislocations, the model combines the solution for the dislocation storage problem with models for dynamic recovery of network dislocations and sub-boundary structures. Finally a general state variable description is obtained. The model includes the effects resulting from variations (a) stacking fault energy (b) grain size (c) solid solution

content (d) particle size and volume fraction. Although the Trondheim group called their model a ‘unified theory of deformation’, controversy exists. Some workers (Shercliff and Lovatt 1999) doubt their ‘unified model’ cannot be straightforwardly applied in a practical context because it introduces many adjustable parameters. Marthinsen and Nes (2001; 2002) later argued the large number of tuning parameters is not a problem and their model can deal with processing conditions under any combination of constant strain rate and temperature or more complex transient conditions. However from the fact that nearly no researchers adopted their model in the FE simulation except only one paper can be found by themselves in a conference (Marthinsen *et al.* 2003) it is safe to say too many adjustable parameters, at least, do hamper its wide application in its integration with FE simulation. Furthermore, it appears that any attempt to unify this theory with materials which dynamically recrystallise has not been successful.

The Sheffield group have approached hot working of aluminium alloys from a background of FE analysis of the transient nature of the deformation history in flat rolling, in terms of temperature, strain rate and strain path. Models for predicting the evolution of internal state variables such as internal dislocation density, subgrain size and misorientation between subgrains, as well as subsequent recrystallisation behaviour are developed for both constant and transient deformation conditions (Baxter *et al.* 1999; Zhu and Sellars 2000). It should be noted that although great efforts have been invested by the Sheffield group to carry out experiments to get the mathematical expressions and to finally validate these models they used very simple FEM that is not capable of structure prediction. Until recently have they begun to resolve proper problems, mainly rolling (Talamantes-Silva *et al.* 2009; Zhu *et al.* 2003).

Despite the criticism that the physically based models from the Sheffield have mainly been concentrated on a specific alloy (Al-1%Mg) and developed from

experiments utilising plain strain compression (PSC), in which plastic strains greater than 2 are difficult to achieve and the interaction of recrystallisation and precipitation has not been considered in detail in the models (Jones and Humphreys 2003), the Sheffield models assisted researchers to study microstructure evolution because the nature of these models focus on the transient nature of the metal processing and they have the advantage of less number of tuning parameters and convenience to be integrated into commercial FEM codes. Sheppard's group has done a considerable amount of pioneering work in this respect. After the success in applying these models into rolling simulation (Duan and Sheppard 2002b, 2003a; Sheppard and Duan 2002) researching attention was turned to its integration with the FEM simulation of more complex extrusion process (Duan and Sheppard 2003b; Duan *et al.* 2004; Flitta and Sheppard 2004; Flitta *et al.* 2007; Peng and Sheppard 2004 ; Sheppard and Velay 2007). In this work suitable models will be chosen and adapted for extrusion and its post-treatment simulation by user-subroutine interface of the commercial FEM software Forge2009[®].

2.6.4.3 Modelling dislocation substructure changes

2.6.4.3.1 Dislocation substructure evolution

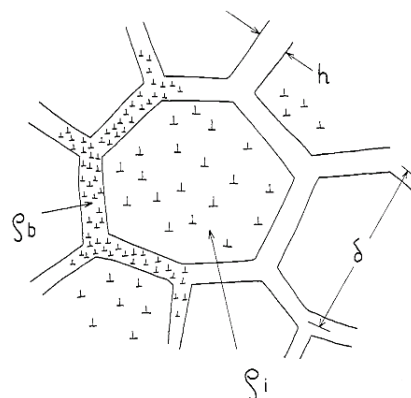


Figure 2.2 A schematic representation of the microstructure; cell diameter, δ , cell wall thickness, h , cell wall dislocation density ρ_b and dislocation density within the cells ρ_i (after Nes 1997)

Dislocation theory is an important tool to study the mechanism of metal plasticity. Dislocation substructure can be described by three internal state variables: dislocation density (ρ), subgrain size (δ) and misorientation across subgrain boundaries (θ). To have a clear understanding of these variables, a schematic representation of substructure was taken from the literature (Nes 1997).

During the early stage of deformation, dislocation multiplication occurs, and the total dislocation density $\rho = \rho_i + \rho_b$ increases from $10^8 \sim 10^{10} m^{-2}$ to $10^{11} \sim 10^{12} m^{-2}$ at the commencement of macroscopic flow. Dislocations move and interact with one another to form tangles. This terminates in a cellular structure with the dislocations clustering tightly into the cell walls separating dislocation free regions. As deformation proceeds, ρ continues increasing and attains a constant value of approximately $10^{14} m^{-2}$ when the steady state regime is reached. The cellular structures are replaced completely by the formation of subgrains due to the additional dislocation reactions. Subgrains can be regarded as an extension of a cellular structure in that the dislocations are arranged in the form of planar networks in subgrain boundaries, while the cellular boundaries consist of three-dimensional network and tangles of dislocation. The ability to form a cellular or subgrain structure depends on several factors: the stacking fault energy, the applied stress, the strain, the temperature and the presence or absence of obstacles.

A notable feature of subgrains is they are equiaxed and maintain their equilibrium size and shape in the steady state even at very large strains whereas the grains are always elongated in the direction of the extension. There are two interpretations for this phenomenon. The first considers that sub-boundaries are constantly migrating in such a way as to keep the substructure equiaxed. The second possible interpretation is by the repeated unravelling of the sub-boundaries and the subsequent reformation of new sub-boundaries at locations which keep their average spacing and dislocation density constant, termed 'repolygonisation' (Jonas

et al. 1969).

2.6.4.3.2 Dislocation density evolution modelling

For steady state deformation a generally accepted equation that represents the relation between the internal dislocation density and subgrain size is written as

$$\rho_i^{\frac{1}{2}} \delta = Constant \quad (2.17)$$

It was first proposed by Holt (1970) from his experiment observations.

In contrast with the consensus reached for the calculation of the dislocation density at steady state deformation, different dislocation evolution models can be found in different work-hardening models such as the Mechanical-Threshold-Strength (MTS) model, the Microstructure Metal Plasticity (MMP) model and the Three Internal Variable (3IV) model reviewed by Holmedal *et al* (Hirsch 2006, p.129). But their purpose is to try to find a flow stress formulation that can include effects due to variations in solid solution level, particle contents, grain size, etc. from a microstructure view point, which inevitably involves many tuning parameters. The difficulty is increased in this problem because some of the parameters are not as yet defined that an intelligent guess must be utilised.

By contrast, Sellars and Zhu's model (Baxter *et al.* 1999; Sellars and Zhu 2000; Zhu *et al.* 1997) developed from an FE background that doesn't have a large number of tuning parameter seems more suitable to be integrated with FEM. In their model, the internal dislocation density ρ_i has two components, that is, the so-called 'random' dislocation ρ_r and the 'geometrically necessary' dislocation density ρ_g ,

$$\rho_i = \rho_r + \rho_g \quad (2.18)$$

This model will be discussed in detail in Chapter 5.

2.6.4.3.3 Subgrain size modelling

It is generally accepted that the subgrain size δ can be directly related to the temperature-compensated strain-rate or Zener-Hollomon parameter, Z , by the following equation

$$\delta_{SS}^m = A + B \ln Z \quad (2.19)$$

where A , B , m are constants.

A good subgrain size fit could be obtained by varying exponent m within a range between -1.25 and -0.35 (Zaidi and Sheppard 1983). In fact, many researchers (Castle 1992; Chanda *et al.* 2000; Subramanian 1989) have chosen $m = -1$ to produce accepted results. This is because in hot working range the subgrain size ranges obtainable are very small when compared with the range of $\ln Z$ value.

It should be noted that equation (2.19) can be modified into different forms (Jonas *et al.* 1969; Nes *et al.* 1994; Sheppard and Raghunathan 1989) to predict steady state subgrain size. But they all use more extra statistically-defined parameters from experimental data and would not be discussed.

It should also be emphasised that equation (2.19) is not valid for prediction of subgrain size in a transient deformation. In contrast with the well recognised relationship for subgrain size during steady-state deformation, there is still a lack of quantitative relationship to relate the subgrain size with the deformation parameters in a transient deformation. Nevertheless, the Trondheim group

(Marthinsen and Nes 1997) and Sheffield group (Sellars and Zhu 2000; Zhu *et al.* 1997) have proposed their equations respectively to model the subgrain size evolution during transient state deformation. The Trondheim group approached the subgrain size problem including the effects of different microstructures which naturally need corresponding parameters to describe. As a result, to use this model those parameters must be derived from experimental data or from reasonable estimation, which greatly increased the difficulty in its integration with FEM. On the other hand, the model from the Sheffield group is calculated from a background of FE analysis of the transient nature of hot deformation history in terms of temperature, strain rate and strain path. In their model, the subgrain size evolution have been explicitly expressed in a differential form, so even though its physical basis is limited to some extent, using this evolution law reasonable results have been achieved in hot working simulation, at least, in rolling simulation (Ahmed *et al.* 2005; Duan 2001). However there is a great lack of research in prediction of subgrain size by FEM in aluminium extrusion. The few attempts (Dashwood *et al.* 1996; Duan and Sheppard 2003b) carried out on this topic either used only empirical steady state equation or were limited to simple rod extrusion. This exactly highlights that using physically-based model to simulate complex shape extrusion is of significance.

2.6.4.3.4 Misorientation change modelling

Misorientation could be the least well-characterised microstructure variable probably because of the obvious experimental technique constraints. Some work concerned about the high purity aluminium is shown in Figure 2.3 (Nes and Marthinsen 2002) that clearly shows that the average boundary misorientation increases rapidly with strain, reaching about 3° at a strain of about 1, after that it remains constant up to strain as high as 4.

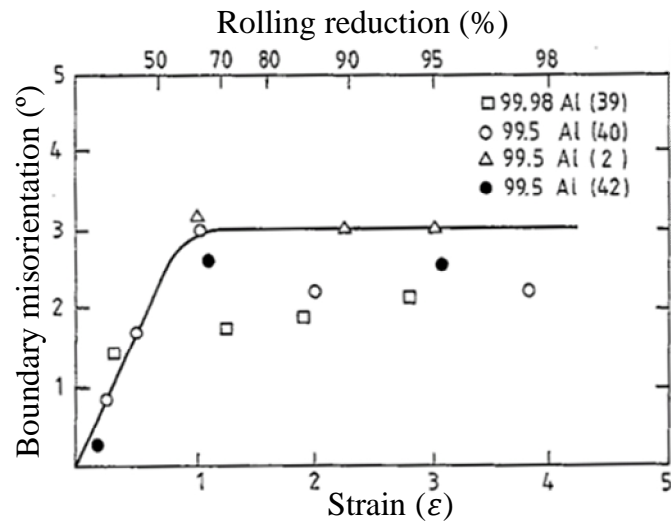


Figure 2.3 Sub-boundary misorientation vs. strain

Sheffield group (Zhu and Sellars 2000) have proposed another relationship for Al-1%Mg alloy during transient deformation conditions in differential form:

$$d\theta = \frac{1}{\varepsilon_{\theta}} (\theta_{ss} - \theta) d\varepsilon \quad (2.20)$$

where ε_{θ} is a characteristic strain. In their study, the predicted results agree well with the experiments for the increasing and constant strain rate conditions while the discrepancy became larger during decreasing strain rate condition. But this is not the case for extrusion; therefore, equation (2.20) has the potential to predict the misorientation that will be investigated further in Chapter 5.

3. Thermal-mechanical simulation of the extrusion process

3.1 Introduction

The Finite Element (FE) procedures are employed extensively in the analysis of solids and structures and of heat transfer and fluids, and indeed, finite element methods are useful in virtually every field of engineering analysis (Bathe 1996, p.1).

In contrast with analytical techniques, finite elements can be applied to complicated shapes. The basic characteristic of the finite element method is the discretisation of the domain of interest, which may have nearly arbitrary geometry, into an assembly of relatively simple shaped elements that are connected by nodes. The finite element method approximates the real value of the state variables considered within each element by interpolation polynomials. This approach of interpolating the variable within each cell amounts to assuming a piecewise polynomial solution over the entire domain under consideration. In the case of elastic and large strain plastic materials response it is usually the displacement that is the unknown state variable. The polynomials usually serve as shape functions to update the form of the finite elements. The coordinate transformation associated with the remesh, for instance during a simulated large strain plastic deformation process is often referred to as the most important component of a successful finite element solution.

3.2 Finite element procedure

The most widely used finite element formulation in solid mechanics is the displacement approach. The displacement field within the element is defined in terms of assumed functions (interpolation functions) and unknown parameters at the nodes which are either displacements or displacement related quantities such as slopes and curvatures. For each finite element, a displacement function in terms

of the element coordinates (x, y, z) and the nodal displacement parameters is chosen to represent the displacement field, and thereby the strain and stress within the element. A stiffness matrix relating the nodal forces to the nodal displacements can be derived through the application of the principle of virtual work or the principle of minimum total potential energy. The stiffness matrices of all the elements in the domain can be assembled to form the overall stiffness matrix for the system. After modifying the global stiffness matrix in accordance with the boundary conditions and establishing the force vector, the system of equations can be solved to yield firstly the nodal displacements, and subsequently the stresses at any point in each individual element.

3.3 The equilibrium equation in FE simulations

Depending on the character of the material response to external and internal load, the material dynamics are conveniently described in terms of the ‘strong form’ of the differential equation of motion, the ‘weak form’ of the virtual work principle, or the stable equilibrium quantified by the ‘minimum mechanical energy’.

A simple straightforward approach to deriving the equations for displacement-based finite element codes starts from the general principle of virtual work. This is the work done by arbitrary small virtual displacements due to the forces and the moments acting on a solid body in accordance with continuity and displacement boundary constraints. For the most general cases this principle can be written as (Zienkiewicz and Taylor 2005, p.14):

$$\delta\widehat{W} = \iiint_V \sigma_{ij} \delta\hat{\varepsilon}_{ij} dV = \iiint_V P_j \delta\hat{u}_j dV + \iint_S T_j \delta\hat{u}_j dS + F_j \delta\hat{u}_j \quad (3.1)$$

where $\delta\widehat{W}$ is the virtual work which results from the strain due to the virtual displacements $\delta\boldsymbol{\varepsilon}$ that act on the stresses $\boldsymbol{\sigma}$. This work equals the sum of the

virtual work which results from the virtual displacements $\delta \hat{\mathbf{u}}$ due to the body force \mathbf{P} , to the surface force \mathbf{T} , and to point forces \mathbf{F} . S is the surface that encloses the volume V .

Equation (3.1) is generally valid for an arbitrary body. However, the finite element method decomposes the solid under investigation into a large number, n , of simply shaped volume elements which are connected at nodes. Thus equation (3.1) applies for each individual element under implicit consideration of equilibrium and compatibility. The course of the displacement is approximated in each finite element by interpolation polynomials that enter all n equations of the form of equation (3.1). This amounts to calculating the volume and surface integrals over each finite segment individually and subsequently summing up all elements. Assuming that the point forces are only applied at the nodal points, the equation (3.1) may then be rewritten

$$\sum_n \iiint_V \sigma_{ij} \delta \hat{\varepsilon}_{ij} dV = \sum_n \iiint_V P_j \delta \hat{u}_j dV + \sum_n \iint_S T_j \delta \hat{u}_j dS + \sum_n F_j \delta \hat{u}_j \quad (3.2)$$

3.4 Finite element kinematical description

The algorithms of continuum mechanics usually make use of two classical descriptions of motion: the Lagrangian description and the Eulerian description.

Lagrangian algorithms, in which each individual node of the computational mesh follows the associated material particle during motion, are mainly used in structural mechanics. The Lagrangian description allows an easy tracking of free surfaces and interfaces between different materials. It also facilitates the treatment of materials with history dependent constitutive relations. Its weakness is its inability to follow large distortions of the computational domain without recourse

to frequent remeshing operations.

Eulerian algorithms are widely used in fluid dynamics. The computational mesh is fixed and the continuum moves with respect to the mesh. In the Eulerian description, large distortions in the continuum motion can be handled with relative ease, but generally at the expense of precise interface definition and the resolution of flow details.

Arbitrary Lagrangian-Eulerian (ALE) technique has been developed that, to a certain extent, succeed in combining the best features of both the Lagrangian and the Eulerian approaches. In the ALE description, the nodes of the computational mesh may be moved with continuum in normal Lagrangian fashion, or be held fixed in Eulerian manner, or be moved in some arbitrary specified way to give a continuous remesh capability. Because of this freedom in moving the computational mesh offered by the ALE description, greater distortions of the continuum can be handled than would be allowed by a purely Lagrangian method, with more resolution than that afforded by a purely Eulerian approach (Belytschko 2000, p.1(3-15); Bonet and Wood 1997, p.3.3).

3.5 Finite element discretisation and element type

To divide the continuum or problem domain into valid finite elements is to discretise the problem domain involved. The number, size and shape of the elements are critical for a successful finite element analysis. The element should be small enough to give useful results and large enough to reduce the computational effort.

Depending on the problems studied different shapes of elements can be adopted. Basic element shapes are shown in Table 3.1. The shapes, sizes number, and configurations of the elements have to be chosen carefully such that the original body or domain is simulated as closely as possible without increasing the

computational effort needed for the solution. Mostly the choice of the type of element is dictated by the geometry of the body and the number of independent coordinates necessary to describe the system. One dimensional or line element can be used if the geometry, the material properties, and the field variable of the problem can be represented in terms of only one spatial coordinate while the configuration and other details of the problem can be described in terms of two independent spatial coordinates the two-dimensional elements can be used and likewise, three-dimensional elements have to be employed when the description of the geometry, material properties, and other parameters of the body needs three independent spatial coordinates.


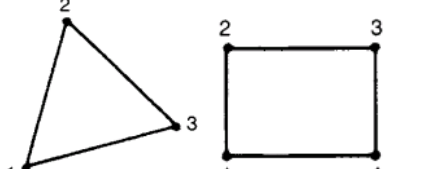
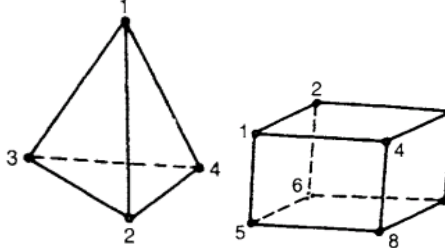
Dimension	Type	Geometry
Line (1-D)	Spring, beam	
Area (2-D)	2D solid, axisymmetric solid, plate	
Volume (3-D)	3D solid	

Table 3.1 Basic element shapes

3.6 Finite element discretisation and increment approach

The detailed theory of this topic can be found in many textbooks. Below is a concise description of it.

Using isoparametric elements, the velocity field \mathbf{v} , can be discretised in terms of the nodal velocity \mathbf{V}_n , shape function \mathbf{N}_n and local coordinate vector $\boldsymbol{\xi}$ as:

$$\mathbf{v} = \sum_n \mathbf{N}_n(\boldsymbol{\xi}) \mathbf{V}_n \quad (3.3)$$

The mapping with the physical space is defined by

$$\mathbf{x} = \sum_n \mathbf{N}_n(\boldsymbol{\xi}) \mathbf{X}_n \quad (3.4)$$

The strain rate tensor is computed with the help of the \mathbf{B} linear operator

$$\dot{\boldsymbol{\varepsilon}} = \sum_n \mathbf{B}_n \mathbf{V}_n \quad (3.5)$$

The pressure field \mathbf{p} is discretised in term of nodal pressure, \mathbf{P}_m , with compatible shape functions, \mathbf{M}_m

$$\mathbf{p} = \sum_n \mathbf{P}_m \mathbf{M}_m(\boldsymbol{\xi}) \quad (3.6)$$

For purely viscoplastic materials, the most popular scheme for nodal update can be performed with the Euler explicit scheme. Then if \mathbf{X}_n^t is the coordinate vector, at time $t + \Delta t$ the new coordinate vector

$$\mathbf{X}_n^{t+\Delta t} = \mathbf{X}_n^t + \Delta t \mathbf{V}_n^t \quad (3.7)$$

A second order scheme was shown to improve the accuracy with a Runge and Kutta method or the semi-implicit scheme (Chenot *et al.* 1998):

$$\mathbf{X}_n^{t+\Delta t} = \mathbf{X}_n^t + \frac{1}{2}\Delta t(\mathbf{V}_n^t + \mathbf{V}_n^{t+\Delta t}) \quad (3.8)$$

3.7 Constitutive equations

Three constitutive equations, the Hansel-Spittel equation the Norton-Hoff equation, the hyperbolic sine function equation and have been usually adopted in FEM simulations. Because Hansel-Spittel equation is a purely statistic equation and has a poor performance in FEM simulation, hence only the other two equations are presented here.

3.7.1 Norton-Hoff equation

This equation is based on the Norton-Hoff behaviour law, written in the following stress tensor form (Chenot *et al.* 1996)

$$\boldsymbol{\sigma}_{N-H} = 2K(\sqrt{3}\dot{\boldsymbol{\varepsilon}})^{m-1}\dot{\boldsymbol{\varepsilon}} \quad (3.9)$$

where K is the material consistency and

$$\dot{\boldsymbol{\varepsilon}} = \sqrt{\frac{2}{3}\boldsymbol{\varepsilon}:\dot{\boldsymbol{\varepsilon}}} \quad (3.10)$$

m is the strain rate sensitivity index which can be a function of the temperature T , such as

$$m = m_0 + m_1T \quad (3.11)$$

3.7.2 Zener-Hollomon equation

The Zener-Hollomon flow stress, σ_{Z-H} , has already been defined in equation (2.8) and is represented as follows

$$\sigma = \frac{1}{\alpha} \ln \left\{ \left(\frac{Z}{A} \right)^{\frac{1}{n}} + \left[1 + \left(\frac{Z}{A} \right)^{\frac{2}{n}} \right]^{\frac{1}{2}} \right\} \quad (3.12)$$

with

$$Z = \dot{\epsilon} \exp \left(\frac{\Delta H}{GT} \right) \quad (3.13)$$

In this formulation ΔH represents the energy threshold required to obtain the dynamic balance between work hardening and softening at steady state. In most aluminium alloys the dynamic recovery mechanism is related to vacancy diffusion. The value of self-diffusion is close to the value of ΔH (Sheppard and Jackson 1997). Furthermore the temperature compensated strain rate parameter, Z , is a function of the process parameters and can therefore be used efficiently in other relations describing the extrusion process or the behaviour of microstructure.

Velay's study (2004, p.86) shows that, compared with the purely statistic Hansel-Spittel equation and the mostly statistic Norton-Hoff equation, the Zener-Hollomon equation is the only one that attempts to utilise the physical nature of the flow stress and the most appropriate equation to represent the flow stress in hot extrusion of aluminium alloys using the FEM.

3.8 Friction model

Three friction laws are available for the modelling of friction between a

deformable object and the rigid tooling: Tresca, viscoplastic and modified Coulomb friction. Velay *et al.* (2003) derived the friction coefficients for the three laws by comparing the computed peak load obtained from virtual extrusion with the experimental values measured by Subramaniyan (1989 , p.220-231). It was found that Coulomb friction law was one of the most suitable friction laws for aluminium extrusion. This law limits the friction to a maximum value after a fraction of the normal stress, σ_n .

The modified Coulomb friction law can be written as:

$$\begin{aligned} \tau &= \mu\sigma_n && \text{if } \mu\sigma_n < \frac{\bar{\sigma}}{\sqrt{3}} \\ \tau &= m\frac{\bar{\sigma}}{\sqrt{3}} && \text{if } \mu\sigma_n > m\frac{\bar{\sigma}}{\sqrt{3}} \end{aligned} \tag{3.14}$$

where $\bar{\sigma}$ is the Von-Mises stress, μ the friction coefficient and m is the Tresca friction coefficient.

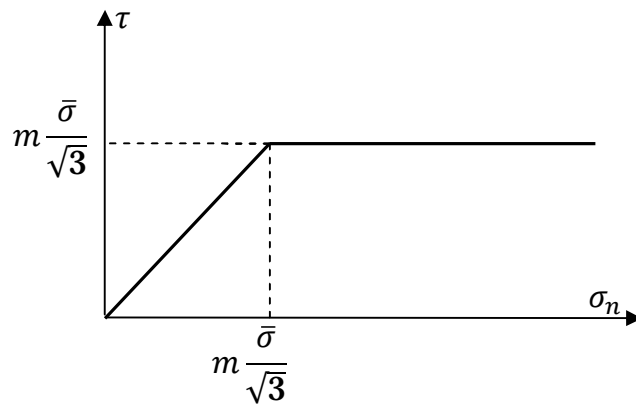


Figure 3.1 Modified Coulomb friction law

With this relationship the friction shear stress is equal to the normal stress σ_n multiplied by the friction coefficient μ or to a fraction of the maximum shear stress

sustainable by the material. Figure 3.1 illustrates this friction law.

3.9 FE approach of the coupled thermal and mechanical problem

In a thermal-mechanical coupled FEM simulation the temperature field is discretised in the same way as the velocity field according to

$$\mathbf{T} = \sum_n N_n(\xi) T_n = \mathbf{N} \cdot \mathbf{T} \quad (3.15)$$

The classical semi-discretised form is easily obtained from the equation

$$\mathbf{C} \cdot \frac{d\mathbf{T}}{dt} + \mathbf{H} \cdot \mathbf{T} + \mathbf{F} = \mathbf{0} \quad (3.16)$$

Where \mathbf{C} is the capacity matrix, \mathbf{H} , the conductivity matrix and \mathbf{F} , the vector contains the visco-plastic heat dissipation and boundary conditions.

The temperature field can be integrated with a second order scheme where

$$\mathbf{T} = a\mathbf{T}^{t-\Delta t} - (1.5 - 2a - g)\mathbf{T}^t + (a - 0.5 + g)\mathbf{T}^{t+\Delta t} \quad (3.17)$$

$$\frac{d\mathbf{T}}{dt} = (1 - g) \frac{\mathbf{T}^t - \mathbf{T}^{t-\Delta t}}{\Delta t} + g \frac{\mathbf{T}^{t+\Delta t} - \mathbf{T}^t}{\Delta t} \quad (3.18)$$

$$\mathbf{C} = (0.5 - g)\mathbf{C}^{t-\Delta t} + (0.5 + g)\mathbf{C}^t \quad (3.19)$$

where a and g are constants (Chenot *et al.* 1998).

3.10 Techniques used in the FEM simulation

A successful aluminium extrusion simulation demands an FEM software that at

least can handle the problems described by Bianchi and Sheppard (1987) and later more comprehensively by Chenot *et al.* (1999) as below

- Large deformation both for 2D and 3D cases,
- Remeshing,
- Complicated temperature evolution,
- Thermo-mechanical coupling,
- Possible changes of microstructure of the workpiece during deformation.

Haupp and Roll (1999) estimated that about 60 finite element (FE) software packages were used for the simulation of forming processes. In their study, initially three commercial software packages were selected for their further investigation. Against the features listed above a technical evaluation was carried out by them using a T-section extrusion as the benchmark problem for the chosen softwares. Finally they were convinced that the French softwares Forge2[®] and Forge3[®] (currently the latest version is named Forge2009[®]) performed best during the T-section extrusion simulation.

The French-developed FEM software Forge2009[®] that incorporates the 2D and 3D module is used in this study. Forge2009[®] is dedicated to the simulation of hot, warm and cold forging of both 3D parts and 2D geometry parts (axisymmetric (revolution) parts and parts with high length-to-width ratios).

FEM has long been proven to a powerful tool to aid engineers and researchers to solve problems in a wide range of fields and the hardwares for computers have also been improved or even innovated greatly in the past decades. However it seems that it is still very difficult for these electronically technological developments to meet scientists' requirements due to their ambition for more realistic simulation for the reality. The most notorious problem is the unbearably long time needed for a complete three dimensional extrusion simulation with a

complex shape.

The most common measure for a FEM software user to reduce computation time is to take advantage of the symmetry of the problem studied. If the configuration of the body and the external conditions (i.e. boundary conditions) can be regarded as symmetric, then only the repeated part of the structure needs to be modelled. There are three common types of symmetry encountered in engineering problems: reflective (or mirror) symmetry, rotational (or axial) symmetry and inversion symmetry.

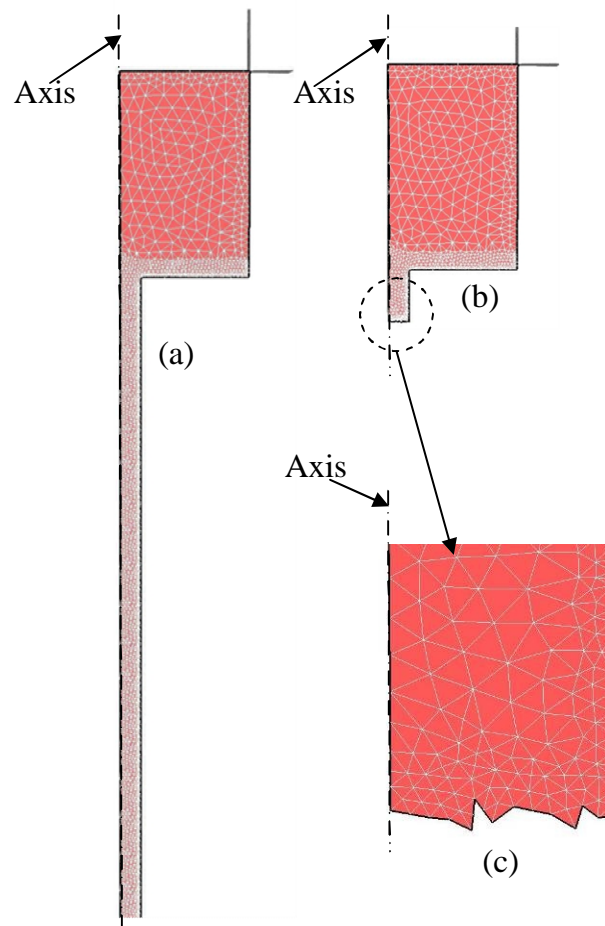


Figure 3.2 Symmetry and auto-trim used in 2D simulation

For an extrusion simulation, a very fine mesh has to be used in the areas of die

mouth, die land and in the following extrudate. Therefore in a complete extrusion simulation, as the ram travels, many small elements in the extrudate will cause congestion, which makes the simulation practically impossible. To solve this problem and facilitate extrusion simulation, an auto-trim technique that so far has not been found in other similar FEM softwares was invented with the collaboration between Sheppard's group and Transvalor. Auto-trim involves killing the elements that are some distance from the die orifice and does not affect the correct calculation, the number of elements in use are significantly reduced.

Figure 3.2 shows a rod extrusion is simplified into a 2D axisymmetric FEM model. Figure 3.2 (a) and (b) are at the same ram travel without and with auto-trim respectively. Figure 3.2 (c) is a magnified view of the extrudate after auto-trim. Because auto-trim reduces the calculated elements, computation time will be saved and focus can be concentrated on the part of interest without having to waste elements in the material far away from die exit.

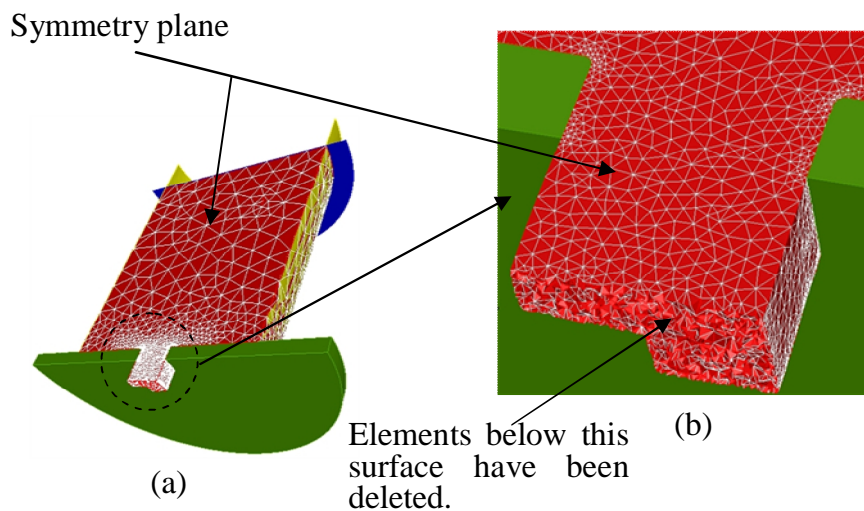


Figure 3.3 Symmetry and auto-trim used in a 3D simulation

Figure 3.3 indicates a 3D simulation that utilises the mirror symmetry and auto-trim technique. It should be noted that excessive time is still required for a

complete extrusion cycle simulation of a complex section even when the symmetry and auto-trim are employed. To further expedite the computation, a cluster version of Forge[®] software would be necessary.

3.11 Data file and user-subroutine

3.11.1 The data file

Before starting a simulation, all the information needed for the simulation must be compiled and input into Forge2009[®]. This can be completed by using the graphic user interface of the pre-processor of the Forge2009[®] or modifying the formatted file (the data file) created by the pre-processor with specific syntax (usually for advanced users).

The data file is composed of a certain number of modules into which the variables are entered using key words. These variables are naturally regrouped by themes into the same module. Depending on which options of Forge2009[®] are used the data file for Forge2[®] can provide up to 17 different modules while the Forge3[®] offers up to 13 modules. Each of the modules presents a category of variables to define. Details of the structure of the data file can be found in the online documents of Forge2009[®] (Transvalor 2009a, 2009b). The main modules used in the simulations in this study are as follows:

- The Unit system module: This module allows the user to choose the unit system for the computation. The keyword ‘*mm-Mpa-mm.kg.s*’ was used, which means the length unit is in *mm*, the stress and pressure in *Mpa* and the units for thermal quantities are the derivatives of *mm*, *kg* and *second*.
- The Rheology and Interfaces module: this module defines the thermo-mechanical characteristics and the contact conditions of the workpiece and the tools.
- The Thermal Computation module: it activates a coupled thermo-

mechanical simulation; otherwise Forge2009[®] will only perform an isothermal simulation.

- The Tooling kinematics and setup module: it imposes general conditions linked to the dies.
- The Numerical Sensor module: Numerical sensors are used to follow the time evolution of several variables which are calculated by the software, which is also a powerful tool to investigate the material flow.
- The Remeshing module: If this block exists, the program will remesh the specific deformable object at a given frequency.

A datafile used for a T-section extrusion was attached in Appendix A.

3.11.2 The user subroutine and its integration with Forge2009[®] solver

A good FEM software must have a user-friendly subroutine interface such that the software becomes an open system and its users can take best advantage of its flexibility and versatility to integrate the knowledge that is beyond the software's original developers and finally, in turn, the feedback from the user can improve the software.

Using Forge2009[®]'s user subroutine, the user can incorporate his own material model, friction model and much more complicated models for structure evolutions during the whole forming process.

Forge2009[®] manages different types of computed variables, some are defined at the mesh nodes (nodal variables) and some are defined inside the volume elements at the volume integration points or inside the surface elements at the surface integration points. The nodal variables number is fixed and limited to the simulation computation direct unknowns. For the thermal computation it is the TEMPERATURE and the temperature variation DELTA_TEMP. For the

mechanical computation it is the VELOCITY vector, the PRESSURE and some auxiliary variables like the previous increment pressure PREV_PRESS and the DISPLACEMENT (Transvalor 2009c).

The detailed procedure to use the Forge2009[®] subroutines can be found in the online documents of the Forge2009[®] (Transvalor 2009c). Its basic steps are:

1. Creation of a new user law using a Fortran editor
 - 1.1. Choose the type of law to use among the existing ones (LOIV EVOL, LOIV MECA, LOIV UTIL *etc*).
 - 1.2. Start editing the Fortran file corresponding to the law type.
 - 1.3. Choose the law name (string with 16 characters maximum), define the parameters, DV and SV (with their respective dimensions) of the user law, in the order in which they will be read in the data file.
 - 1.4. Add the Fortran line: « elseif (nom.EQ.'MY_LAW') then » in which “Nom” is the Fortran variable containing the name of the user law read in the data file and MY_LAW is the user law name defined by the user.
 - 1.5. Write the Fortran code computing the values of gs_var and gs_eta (and gs_etat_point for the UTIL law type) as a function of gs_par and the other values transferred to the routine by arguments.
2. Activation of the new user law in the data file: the user law MY_LAW is activated in the datafile with the sub-module (in the .RHEOLOGIE module):
3. Compiling the new user routines. After the compilation, the user will find in the Forge2009[®] installation directories named “bin/ UserF2 and bin/UserF3” the newly created user dynamic link library;
4. Register the new solver using the new dynamic link library generated in step 3 through the Transvalor Solution Launcher;
5. Run a User solver: as soon as the user solver is registered, it may be chosen for computations by selecting its name in the Solver name field of the launch menu;

6. Using the Forge2009[®] post-processor to display the user created variables.

The calculation of the grain boundary area per unit volume using tetrakaidecahedron grain model was briefly described in Appendix B to demonstrate the procedure to use the subroutine of the Forge2009[®].

3.12 Concluding remarks

In this chapter the thermal-mechanical coupled FEM was briefly reviewed and some special techniques of the FEM software were highlighted. Several conclusions are drawn as follows:

1. The Lagrangian formulation is the suitable method to simulate extrusion process.
2. The Zene-Hollomon formulation is the most appropriate constitutive equation to describe the flow stress in hot extrusion of aluminium alloy using FEM.
3. The Coulomb friction law best represents the friction mechanism during the aluminium extrusion and can give good results in FEM simulation.
4. The user routine interface of the Forge2009[®] is an important tool for user to implement secondary development. Through the user subroutine it is possible to integrate different models with FEM.

4. Forge[®] validation using both original observations and results from the literature

This chapter validates the use of Forge[®] FEM by discussing various simulations mainly conducted by the author and also data described in the literature. Hence some original observations were presented to support the validity of simulation predictions. The primary parameters of interest are those related to mechanical metallurgy; for example, load, temperature, friction; and those related to structural features such as Zener-Hollomon parameter, subgrain size and misorientation and discussion of the relationship between these parameters and continuum values.

4.1 Introduction of direct and indirect extrusion simulations

It has been noted that almost since the inception of the extrusion process there have been two modes of operations: direct extrusion and indirect extrusion. Figure 1.1 indicates the different sequences of movements for direct and indirect extrusion. The major difference is that in the indirect mode there is no friction between the billet and container whereas in the direct mode the outer shell of the billet is assumed to move relative to the container as the extrusion proceeds (Chadwick 1970; Sheppard and S.J. Paterson 1982; Tuschy 1971). The difference between the two modes can be found in great detail in previous studies (Sheppard and S.J. Paterson 1982). Thus in direct extrusion the surface of the billet is sheared at, or slides along, the container wall. In every case, part of the extrusion load, depending on the length of the billet, is expended in overcoming the friction between the billet and container, or in shearing the inner material from the slower-moving peripheral layer adjacent to the container wall. As one would expect, this results in considerable variation in flow behaviour which will be discussed.

4.2 Extrusion experiments for validation

4.2.1 Extrusion press

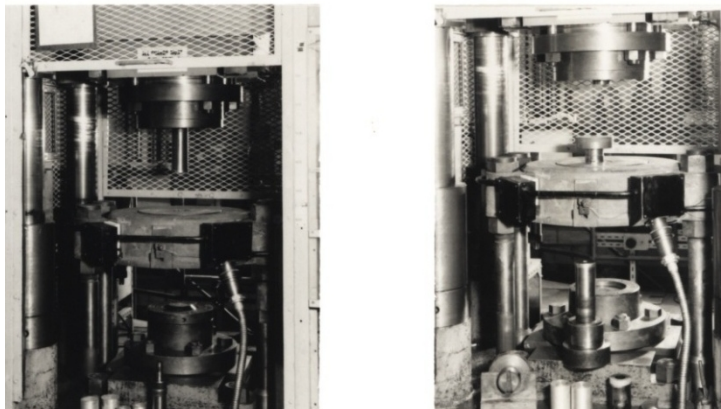
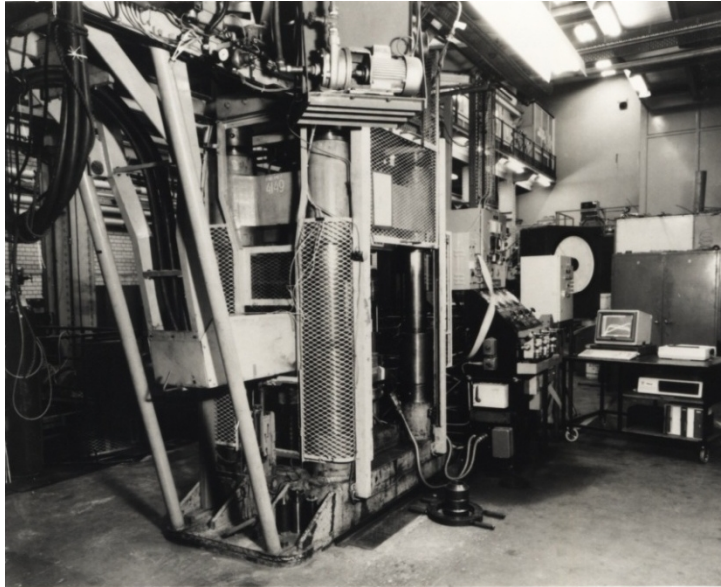


Figure 4.1 General layout of the extrusion press and the direct and indirect tooling (Subramanian 1989, p.49)

The layout of the extrusion press and the direct and indirect extrusion tooling are shown in Figure 4.1.

Experimental data was taken from Subramanian (1989)'s experiments. Extrusion

was performed on a 5MN press (at Imperial College, London) operating with tooling set up for direct and indirect extrusions. Both extrusion ratios are 40:1, the ram speed is 5mm/s and 3mm/s for direct and indirect extrusions respectively. The initial billet temperature was 400°C and the temperature for tools is 350°C. The billets were 75mm in diameter and 95mm long and were heated in an induction heater.

The load was measured by a Mayes load cell situated directly above the ram, the output from the cell being recorded on a Labmaster. Output from a pressure transducer situated at the inlet to the main cylinder was also recorded in order to check load measurements. Ram speed and displacement were measured by a rectilinear potentiometer fixed between the moving crossheads and the press bolster which transmitted to the Labmaster.

The container was hydraulically lowered into position and the ram removed to its highest point. Two semi circular rings were placed on top of the container to prevent any damage to the main ram.

The hot billet was transferred from the induction heater into the container. A pressure pad was dropped on top of the billet. The ram was then lowered, initially under a fast approach and then at a predetermined speed during the extrusion cycle. The ram, followed by the container, was then raised allowing the extrudate to be cut and pushed into the quench tank. The discard was then removed by raising the container, and pushing it out slowly using a tight fitting scrapper pad in front of the main ram.

The procedure for the indirect extrusion was essentially the same except that the 75mm ram was removed from the main ram and immediately prior to extrusion the container was raised such that the die assemble at the top of the mandrel was positioned in the bottom 50mm of the container. Upon transferring the preheated

billet, the dummy block was placed in the container and the extrusion cycle was initiated as for the direct extrusion. When the main ram hit the dummy block both the billet and container were pushed down onto the mandrel and moved simultaneously at the predetermined speed during extrusion.

4.2.2 Material compositions

The material used in the experiment was supplied by Alcan Labs, Banbury, in the form of semi continuous logs of 86mm in diameter. The quoted composition is given in Table 4.1.

Cu	Mn	Mg	Fe	Si	Zn	Ti	Al
4.66	0.69	1.35	0.19	0.08	0.02	0.01	Balance

Table 4.1 Chemical compositions (wt%) of cast alloy AA2024

4.2.3 Tooling

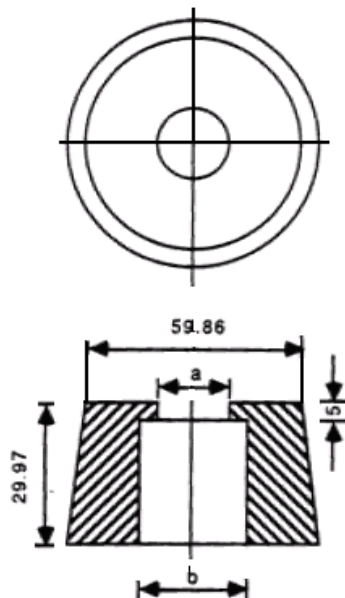


Figure 4.2 The die used for rod extrusion (in mm)

The geometry of the die used in the extrusion for validation is shown in plane and

section view in Figure 4.2, in which for an extrusion with extrusion ratio of 40:1, a is 11.54 mm, b , 15.63 mm.

4.2.4 FEM model setup

For hot extrusion, the elasticity effect can be ignored and hence the most economical constitutive laws are purely viscoplastic approximations. The above-mentioned equations (2.8) and (2.9) were used to describe the flow stress.

The aluminium alloy AA2024 was chosen as the material for all direct and indirect simulations. For the aluminium alloy AA2024, $DH=148880$ J/mol, $A=3.252 \times 10^8$, $\alpha = 0.016$, $n = 4.27$ (Sheppard and Jackson 1997; Sheppard and Wright 1979b).

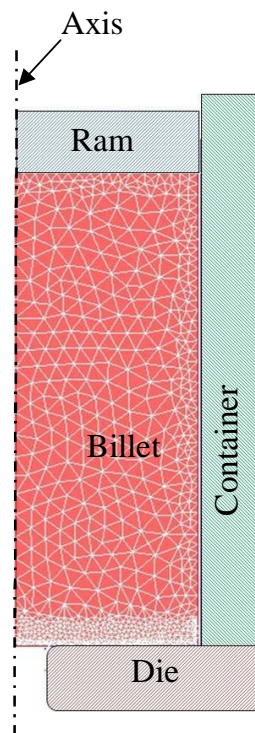


Figure 4.3 FEM model of the rod extrusion

In direct extrusion, the ram pushes the billet towards the die orifice to obtain the desired shape and properties. The container and die are fixed in this case (Figure

4.3). For indirect extrusion in an industrial environment the container and ram are fixed and the die moves towards the billet. However for the purpose of these simulations the die was fixed and both the container and ram were allowed to move together towards the die.

To reduce the computer analysis time, axisymmetric FEM model was used and ram, container and die are assumed to be rigid, which means there is no deformations considered for the tools and a single temperature value is assigned to each component during thermomechanical coupled computation. The radius of the die entrance is 1mm. The mesh size is a set value of 4mm with a meshing option of 'fine front' value of 2mm. This allows finer meshes near the surface of the billet or at the die corner (as shown in Figure 4.3). Six-node triangle elements are adopted to discretise the billet. Each element side is described by a second order curve. The heat transfer coefficient between the billet and tools (die, ram and container) is set as $20000\text{Wm}^{-1}\text{K}^{-1}$. The convective heat transfer coefficient is $10\text{Wm}^{-1}\text{K}^{-1}$. The emissivity is chosen as 0.05. The Tresca friction law is adopted. The friction factor ($0 \leq m \leq 1$) on the ram/billet is 0.4, and 0.85 for the container/billet. For the die, according to Paterson's study (1981), the friction factor on the die land contact region is much lower than that in other contact regions, in this study, the friction factor within the die land/billet interface is 0.1, and 0.8 for the remaining part of the die.

4.3 Extrusion load validation

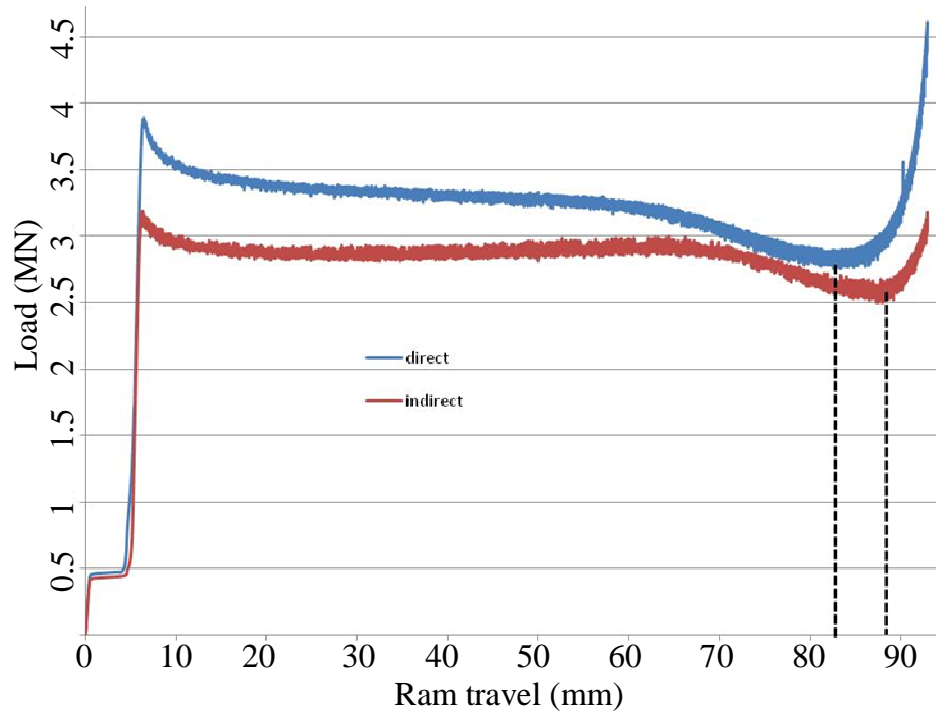


Figure 4.4 Variation of load with ram displacement for both modes of extrusion

Figure 4.4 compares the extrusion pressure/ram displacement diagrams obtained from the direct and indirect FEM simulations. The load loci differ for the direct and indirect extrusions but follow a similar pattern. As expected the indirect mode exhibits a load which is always lower than that in the direct case with a maximum difference of 0.75MN at the peak load, and the gap between them narrows from the peak until the end of the ‘steady state’ because the predicted indirect load increases slightly while the direct load has a considerable decrease. This is mainly caused by the different frictions and consequent temperature increase resulting from the differing extrusion modes. The difference is most pronounced during the period when the loads increase from zero to their peak values; the ‘steady state’ region being attained earlier in the indirect case. Most certainly this is because the

dislocation density will be lower in the indirect case. One interesting point is that the pressure rise at the finish of the ram stroke commences at 82mm for the direct case and is 87mm in indirect extrusion. This indicates that the discard depth should be 13mm for direct extrusion and 8mm if we are able to use an indirect press. This represents a small but significant increase in productivity.

The predicted peak load 3.9443 MN for the direct extrusion is exactly the same as the load obtained from experiment, 3.94 MN, whilst the predicted peak load of the indirect extrusion exceeds the experimental measurement by about 10%. This is largely because of possible overestimation of the friction between the billet and tools but is more likely to be due to an underestimation of the heat transferred across the die face. Nonetheless for an FEM simulation, the predicted load is acceptable.

4.4 Temperature evolution during extrusion

4.4.1 Comparison between predicted temperature and experiment

Grasmo *et al's* (1992) conducted experiment to determine temperature evolutions of ram, container and die during the extrusion of AA6060 alloy by inserting thermocouples to critical locations. Their results are shown in Figure 4.5 in which their experimental and calculated values for thermocouples 7, 8, 9 and 14 are presented.

Measurements of the thermocouple 7 represent the extrudate's temperature evolution at the die entry. By comparing their predicted results at the thermocouple 7 with Grasmo *et al's* (1992) results, Flitta and Sheppard (2005) validated the predicted temperature readings from Forge[®], which is displayed in Figure 4.6. Although small but acceptable deviations from the experimental results can be found a close agreement can be seen between Forge[®]'s simulation and the experimental results.

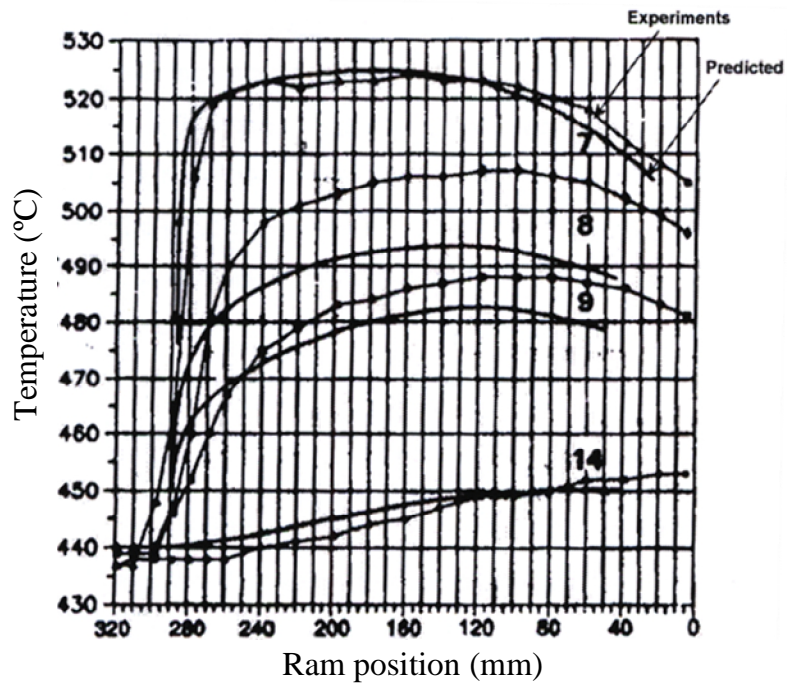


Figure 4.5 Temperature changes according to Grasmó *et al*'s experiment (1992)

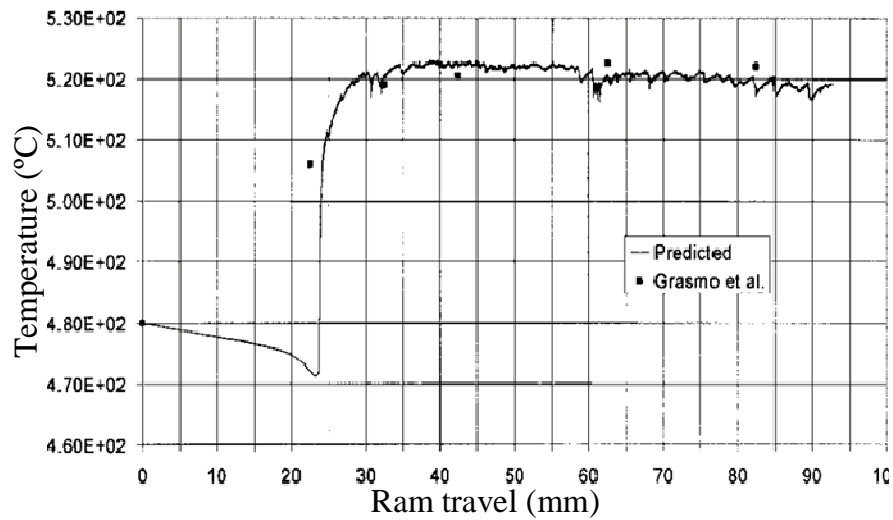


Figure 4.6 Forge[®] predicted temperature vs. Grasmó's experimental measurements at the thermocouple 7 (Flitta and Sheppard 2005)

4.4.2 Billet temperature distributions for both direct and indirect extrusions

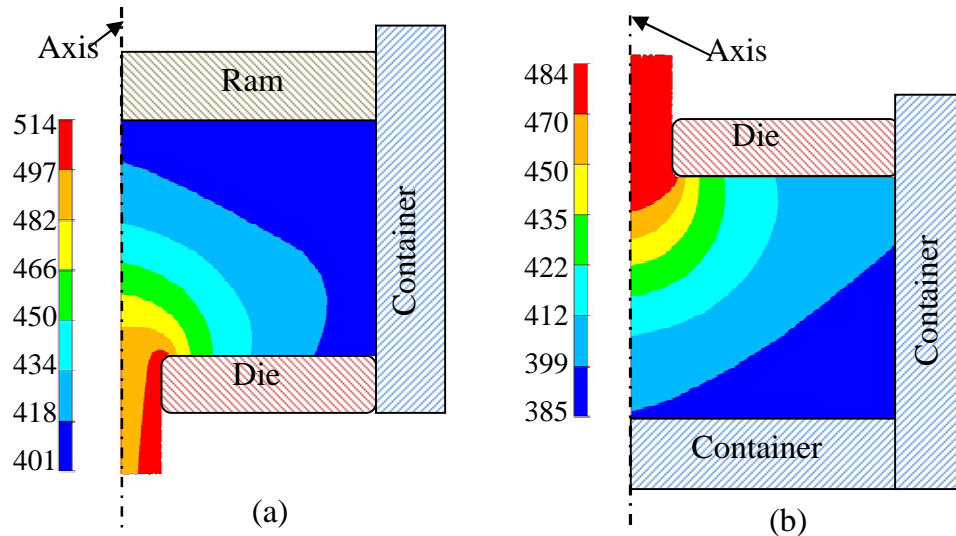


Figure 4.7 Temperature distribution for (a) direct and (b) indirect extrusions at the ram travel of 65mm (in °C)

The predicted temperatures at the ram displacement of 65mm for both extrusion modes are shown in Figure 4.7. The results show that with the same initial temperature, billets both direct and indirect extrusions experience considerable temperature rises, and they have similar distribution patterns. It can be seen that the further the material is from the die exit the lower the temperatures rise is with the lowest temperatures appearing at the corners farthest from the die exits. However, the increase is greater and more acute for the case of direct extrusion. Although in both cases the temperature difference within the billet is about 100°C, it can be seen that in direct extrusion, the cooler blue area occupies nearly half of the billet butt and there exists a temperature difference between the internal and the outer part of the extrudate while in the indirect mode the cooler is less widespread in the billet butt and an extrudate with even temperature distribution is acquired. Since temperature is an important parameter for microstructure evolution, it is safe to say that the indirect extrusion gives a greater possibility to achieve a

homogeneous structure. Critically the final temperature of the extrudate appears to be determined by the die-entry radius. However the lower final temperature in the indirect case will result in fewer propensities for damage to the surface of the extrudate and/or the possibility to utilise greater extrusion speeds. Each of these points may be relevant. The reduction in temperature could lead to some retained substructure in the heat treated condition: thus increasing strength, fracture toughness and corrosion resistance and the increased ram speed to additional productivity adding to that produced by the reduced discard length.

4.5 Metal flow and surface formation

Metal flow in the extrusion process is an important factor controlling the mechanical properties of the extruded products. The description of material flow during the extrusion process has been the focus of much interest in aluminium alloys (Castle *et al.* 1988; Clode and Sheppard 1990; Flitta and Sheppard 2002, 2003; Sheppard *et al.* 1998; Sheppard and Wood 1980; Valberg and Malvik 1996). Studies of the material flow during extrusion are well documented in the literature. The techniques range from commonly used techniques such as gridded billets (introducing pins of an aluminium alloy into the as-cast billet and then grinding and etching the surface after the end of the extrusion (Sheppard and Wood 1980; Subramaniyan 1989; Valberg and Malvik 1996)) to marking grids within the initial billet (Flitta and Sheppard 2000; Flitta and Sheppard 2002, 2003; Hou *et al.* 2000). These techniques did achieve practical results describing metal flow, but in contrast with their cumbersome procedures, numerical simulation with FEM is now a powerful and flexible tool to get a more comprehensive understanding of the extrusion process.

In Forge[®] there are two tools that are dedicated to predicting material movement during metal forming process. The first one is called ‘Grain Flow’ technique (once called Marking Grid). Besides its ability to track folds or other defects inside the

billet, it can visually display the material flow using grids. It was well-documented that reliable metal flow results can also be acquired from it (Flitta 2004; Peng 2005; Velay 2004). The second tool is called 'Sensor'. Compared with the macroscopic nature of the 'Grain Flow', a 'Sensor' can 'pinpoint' a material point's exact position plus its scalar information during the whole extrusion simulation at any time.

4.5.1 The application of Grain Flow technique

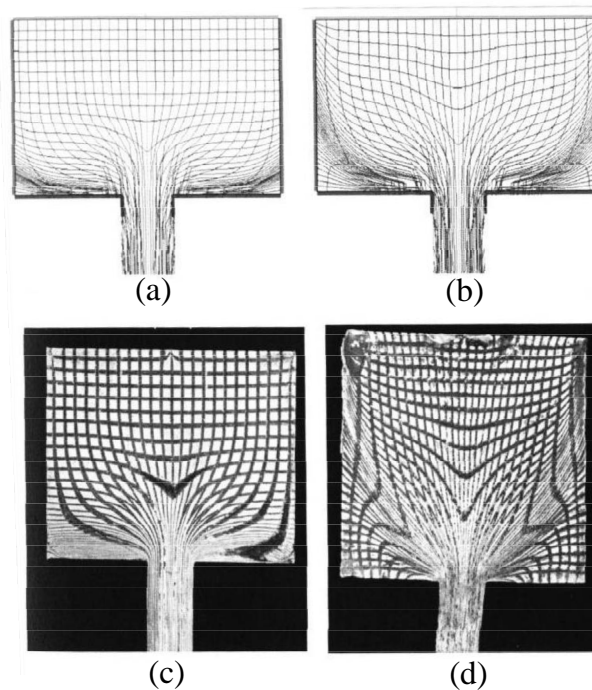


Figure 4.8 Simulated flow patterns (a) at 300°C (b) at 450 °C and the corresponding experimental flow patterns (c) at 300°C and (d) at 450 °C (Flitta 2004, p.125)

Flitta (2004, p.125) evaluated the effects of material flow at both high and low temperature direct extrusion using the Grain Flow technique and compared the simulation with the experimental results from experiments (Sheppard and Tutchter 1980) which are shown in the Figure 4.8 (c) and (d). It is obvious that the flow

patterns in the simulation and the experiment have an excellent agreement. Peng (2005, p.82 and p.84) applied this technique in the metal flow prediction to an indirect extrusion. Figure 4.9 also displays the simulation result is in a very reasonable correspondence with the experimental result.

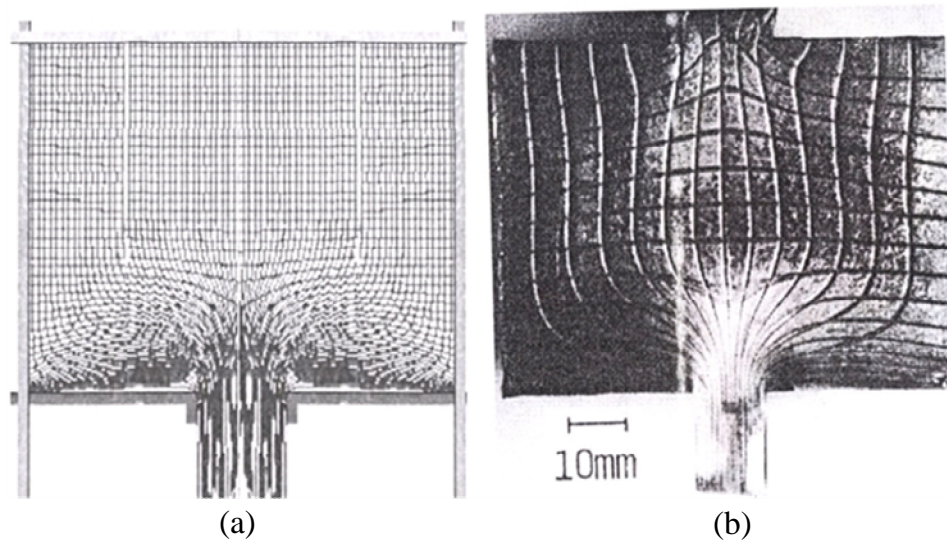


Figure 4.9 (a) Predicted flow pattern (Peng 2005, p.82) and (b) experiment result (Peng 2005, p.84) in an indirect extrusion

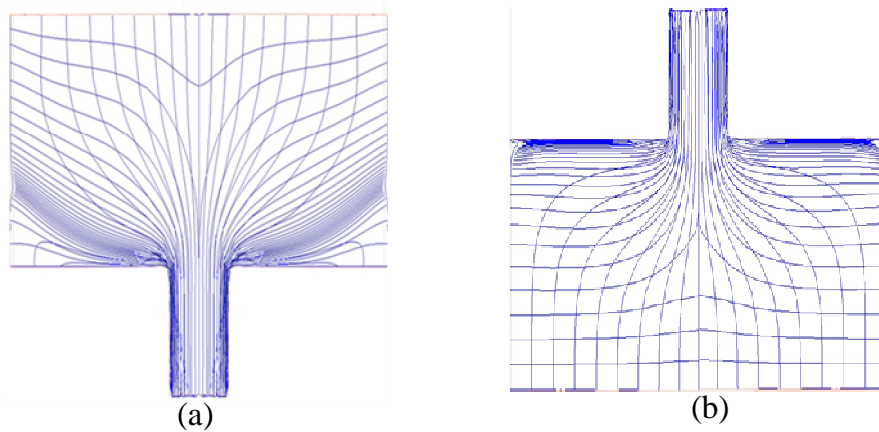


Figure 4.10 Simulated flow patterns (a) direct and (b) indirect extrusions

In this study, the simulated ‘Grain Flow’ results for the direct and indirect extrusion experiments are presented in Figure 4.10, which are also typical direct

and indirect extrusion material flow patterns.

4.5.2 The application of the Sensor technique

It can be seen from the literature that Grain Flow technique has been widely used to investigate the macroscopic metal flow mechanism of extrusion and good results can be achieved. To more accurately track the path of the movement of one material point such that the surface formation mechanism of extrusion can be understood, the simulation technique termed ‘Sensor’ has to be used.

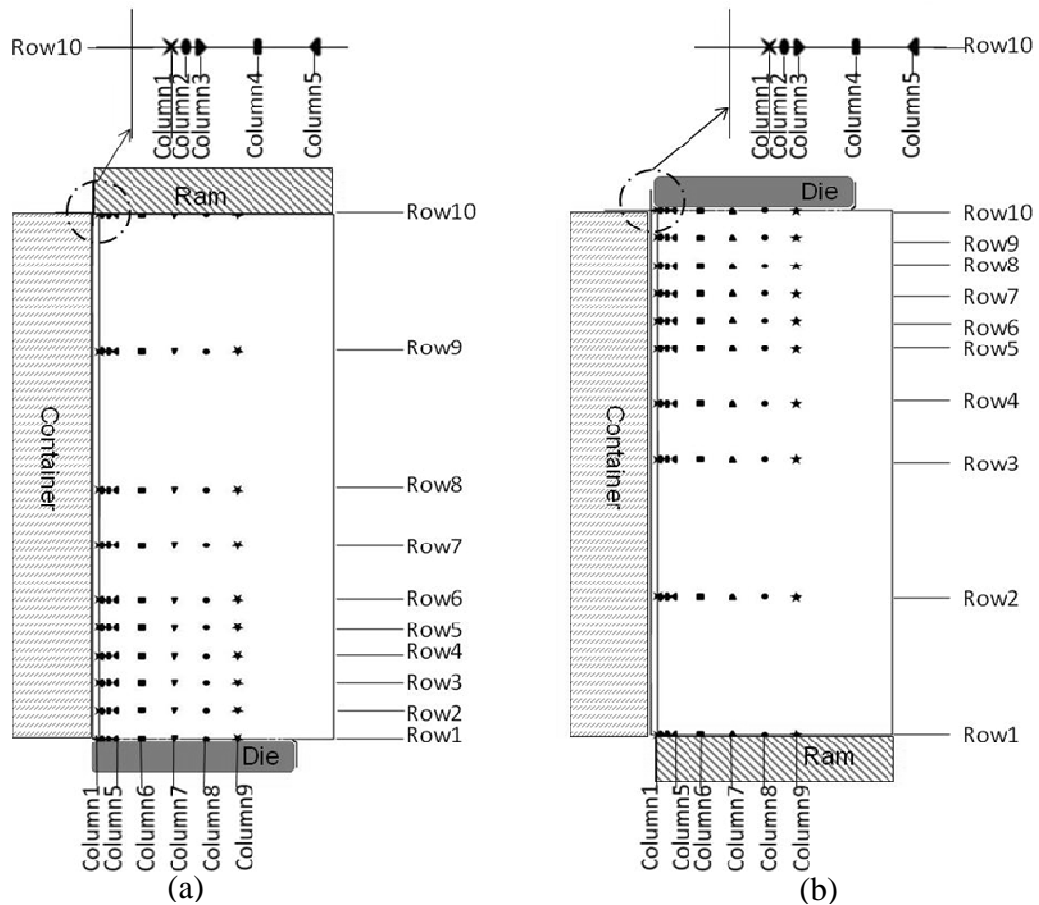


Figure 4.11 Sensors' initial positions (a) for direct and (b) indirect extrusions

Next is an investigation of the surface formation for both direct and indirect extrusions. The initial positions of the sensors are shown in Figure 4.11 for both

the direct and the indirect extrusions. For convenience, they are denoted according to their position in row and column.

For example, sensor (8,9) implies the sensor at the intersection of row 8 and column 9. Here for both cases distances of columns from the billet surfaces are: 0, 0.2, 0.5, 1.5, 2.5, 6.5, 11.5, 16.5, and 21.5mm for columns 1-9 and distances of rows from the die face are: 0, 5, 10, 15, 20, 25, 35, 45, 70, 95mm for row 1-10 in direct extrusion, and with all the distances in a reverse order for row 1-9 in indirect extrusion.

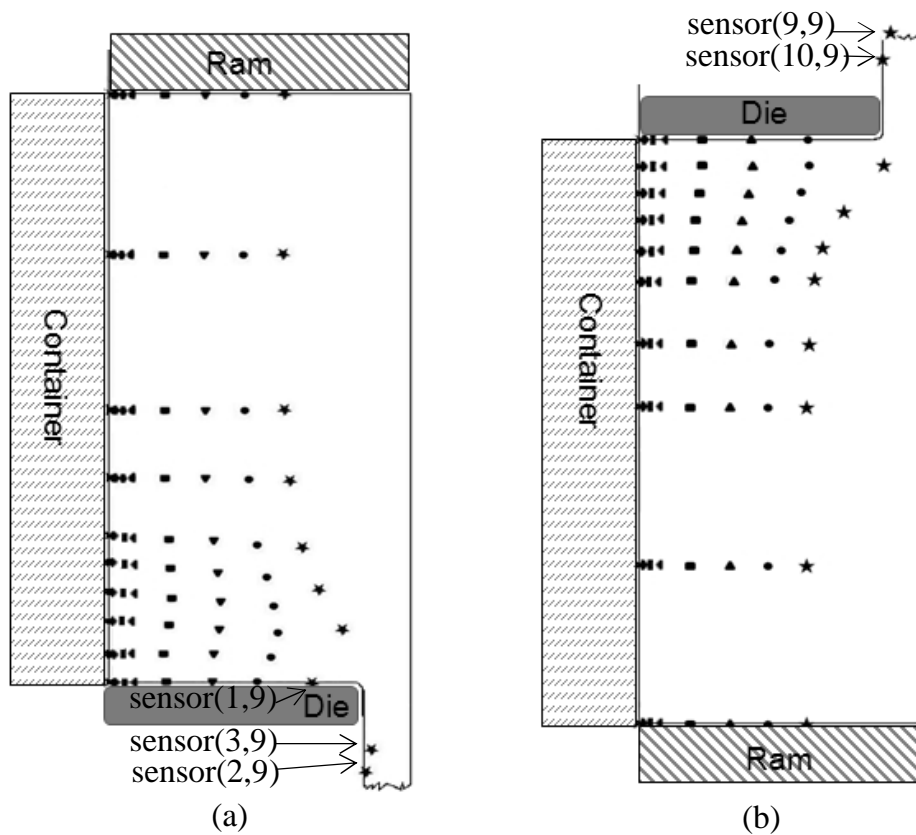


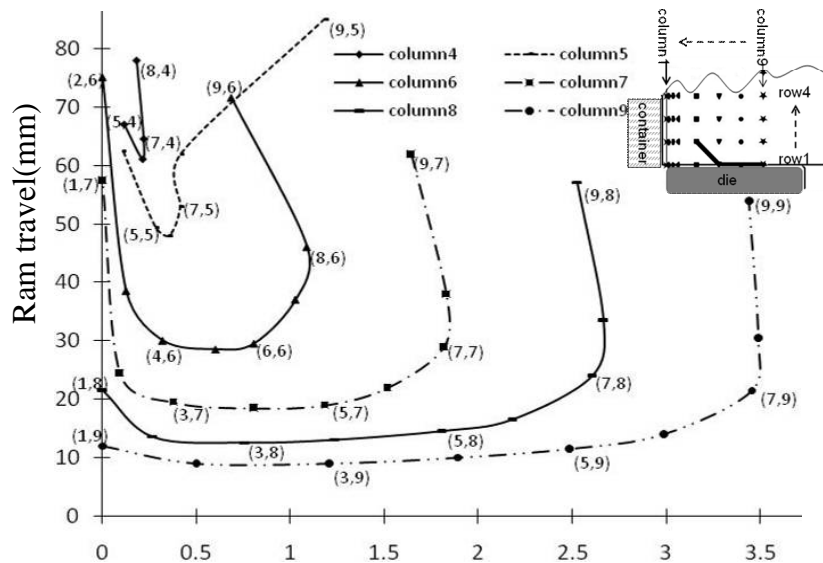
Figure 4.12 Positions of sensors (a) for direct extrusion at ram displacement 9mm and (b) for indirect extrusion at ram displacement 9.5mm

Two frames are captured from the FE simulation and presented in Figure 4.12. It demonstrates the material flow in the billet illustrated by the movement of the

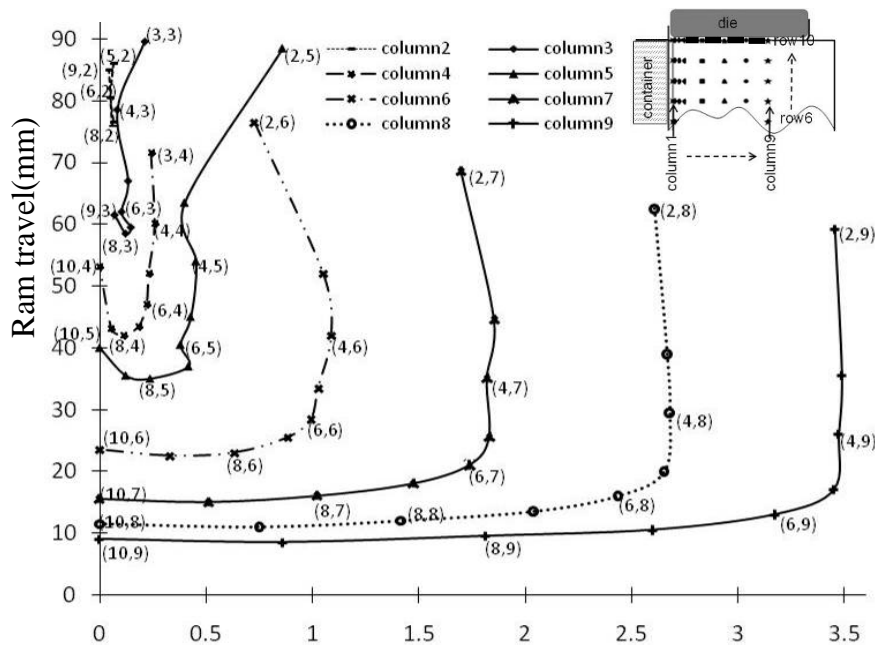
sensors at a ram displacement of 9mm (Figure 4.12 (a)) for direct extrusion and 9.5mm (Figure 4.12 (b)) for indirect extrusion. Figure 4.12 (a) shows significant movement of the sensors in direct extrusion at a ram displacement of 9mm. At this stage both sensors (2,9) and (3,9) have entered the extrudate but are not on the surface. Sensor (1,9) is moving along the die face and would reach the extrudate at a further stage. Little movement is observed for the sensors which are away from the die exit. In Figure 4.12 (b), with a 9.5mm of ram displacement, quite similar movement is achieved for the sensors in the indirect extrusion billet. There are also two sensors which have moved into the extrudate. Of them, sensor (10,9) slips into the extrudate along the die face, representing part of the material that forms the extrudate surface, whilst sensor (9,9) is in the inner part of the extrudate. As one can imagine, with the process of extrusion for both modes, more and more sensors will flow into the extrudates and by recording their position in the extrudates, we can get a better understanding of metal flow and the extrudate surface formation.

Figure 4.13 assists the reader to interpret the extrudate surface formation for direct and indirect extrusions by presenting the relation between distance from the extrudate surface and ram travel of each sensor that finally forms the extrudate. In the graph each curve represents the sensors on a specific column which finally moves into the extrudate. For direct extrusion, curves in Figure 4.13(a) show similar shapes, for each curve (column), the closer the sensors are to the die face, the nearer they would finally appear to the extrudate surface. However each column exhibits a reverse change in curvature which would appear to occur at points around sensors on row 7 (sensor (7,4), sensor (7,5), sensor (7,6), sensor (7,7), sensor (7,8) and sensor (7,9)). From this point the graph representing columns approaches the surface at a greater rate with increasing ram travel. However this does not apply to column 5 in which sensor (9,5)'s position is further from the extrudate surface than sensor (7,5), rather than being closer if it were to follow a similar path to the other sensor loci described above. It seems abnormal if we

further compare it with other sensors (sensor (9,6), sensor (9,7), sensor (9,8) and sensor(9,9)) with which sensor (9,5) is in the same row in the initial setup. The fact we can see from these four sensors is the closer the sensor is to the billet surface, the nearer it would finally appear to be to the extrudate surface (this trend even applies to other sensors in the same row). Actually it is evidence of the back-end effect during which surface material of the billet moves into the central part of the extrudate rather than the periphery at the final stage of extrusion. It appears that none of the sensors column 1, 2 and 3 are relocated to the extrudate during extrusion. Those closest to the container, appear to be relocated to the ram face or in the Dead Metal Zone (DMZ) and hence will be found in the discard and will not appear in this figure. It is thus clear that for the direct extrusion those defects which are located on the billet surface (and in general are not removed by machining) will not harm the quality required in the finished extrude since their eventual locations will be in the discard. The initial positions of those sensors which formed the extrudate surface were marked in the small inset initial sensor set-up figures for both cases. For the direct mode, only sensors (1,9), (1,8), (1,7) and (2,6) fell on the extrudate surface. All others either travelled to the interior of the extrudate, or were deposited in the discard or remained in the DMZ (where, of course, they did not move). Reviewing both Figure 4.12 and Figure 4.13(a) leads to the conclusion that extrudate-surface-forming material comes from near the line connecting sensors (1,9), (1,8), (1,7) and (2,6) and between column 6 and column 1. The DMZ exists behind this line in the corner of the container.



(a) Sensor's distance from extrudate surface for direct extrusion (mm)



(b) Sensor's distance from extrudate surface for indirect extrusion (mm)

Figure 4.13 Relation between ram travel and sensor distance from the extrudate surface (a) for direct extrusion and (b) for indirect extrusion

Overall, Figure 4.13(b) has a similar shape showing that for each curve there is a point at which the curvature reverses which also is approximately close to sensors located on row 7 and the closer-to-billet-surface-the-closer-to-extrudate-surface

observation applies as in direct extrusion except that in column 5 sensor (2,5)'s final position is further from the extrudate surface than those that are in the same row and is caused by that section which will become the back-end effect. It also shows that the surface of the extrudate will be formed mainly from the material located in the designation of row 10 (initial positions are marked in the inset figure), which are sensors (10,9), (10,8), (10,7), (10,6), (10,5) and (10,4). The figure indicates that in the early stage this material does not reach the surface of the billet which suggests that a 'dead metal zone' may be very temporarily formed in the centre region of the die face as previously reported by Sheppard and Patterson (1982) but will certainly not be a permanent feature as in the direct case. A striking difference between direct and indirect extrusion is that nearly all of the sensors were relocated in this process even for those not appearing in the Figure 4.13(b), such as sensor (9,2) near the die/container corner, which suggests there is a larger deformation zone but there is not a DMZ as in the direct extrusion. A larger deformation zone leads to a relatively homogeneous structure and the non-existent DMZ has even been reported as the cause of Geometric Dynamic Recrystallisation (GDX) and Peripheral Coarse Grain (PCG) by other investigators (Bandar *et al.* 2008). It would also seem improbable that PCG originates from these so-called GDX grains in a non-existent DMZ. Despite this fact, it is very clear that in indirect extrusion the subcutaneous layer of the billet will form the subcutaneous layer of the extrudate (see column 2 in Figure 4.13(b)) or even the extrudate surface if we take the computation tolerance of the FEM software into account. Combining information from both Figure 4.12(b) and Figure 4.13(b) the conclusion can be drawn that the extrudate surface is formed by material from the die/billet interface and could also contain material from the subcutaneous layers of the billet (but less than 0.2mm) that in the later stages slide along the die/billet interface. This implies that control of billet quality in indirect extrusion requires either no machining of the billet surface or very little careful pre-machining.

4.6 Microstructure prediction in simple 2D simulation

Integrating appropriate mathematical models into Forge[®], microstructure evolution information during different metal forming process can be predicted. Good results have been obtained by Duan (2001) for aluminium rolling combining the FEM with the microstructure evolution models through Forge[®]'s subroutine interface. Later this integrated modelling method was applied by Peng (2005) to a more complicated forming process, 2D rod simulation. Because of greater relevance to the current study, Peng's results will be briefly reviewed.

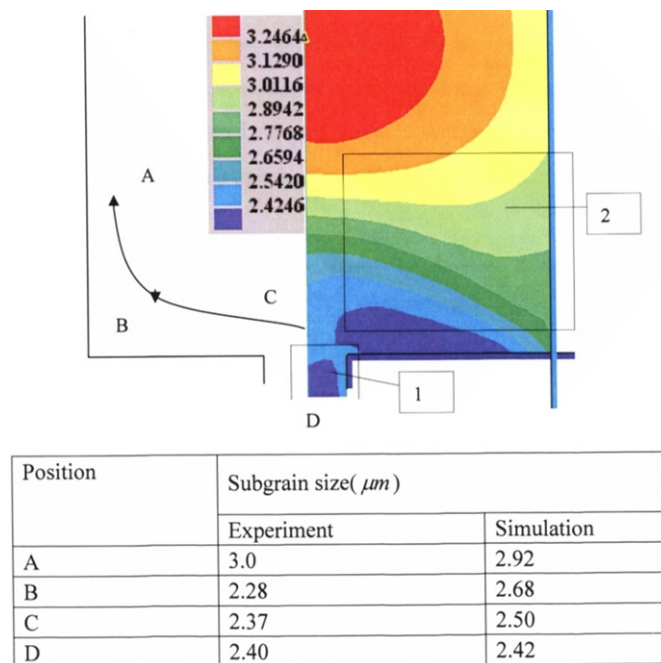


Figure 4.14 Subgrain size distribution (Peng 2005, p.89)

Figure 4.14 compares the simulated subgrain size with its experimental equivalent. Although the biggest error is about 17.5%, the prediction can be taken as reasonable for there is a relative error of 9% in any subgrain size measurement (Peng 2005, p.88). The phenomenon that subgrain size in the periphery is considerably larger than that in the centre shown in Figure 4.15 is in agreement with that observed previously (Sheppard 1993). Peng also predicted the average

volume fraction recrystallised along the extrudate longitudinally, which can be regarded approximately to be equal to the experimental value.

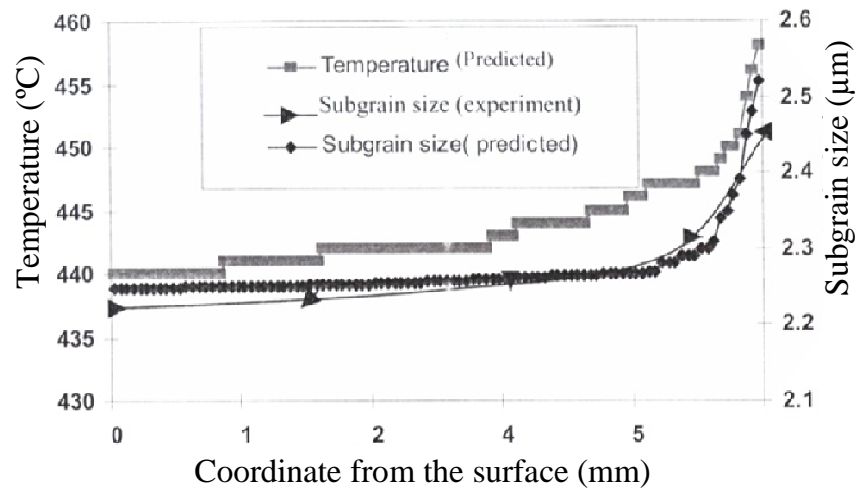


Figure 4.15 Transverse subgrain size and temperature distribution (Peng 2005, p.88)

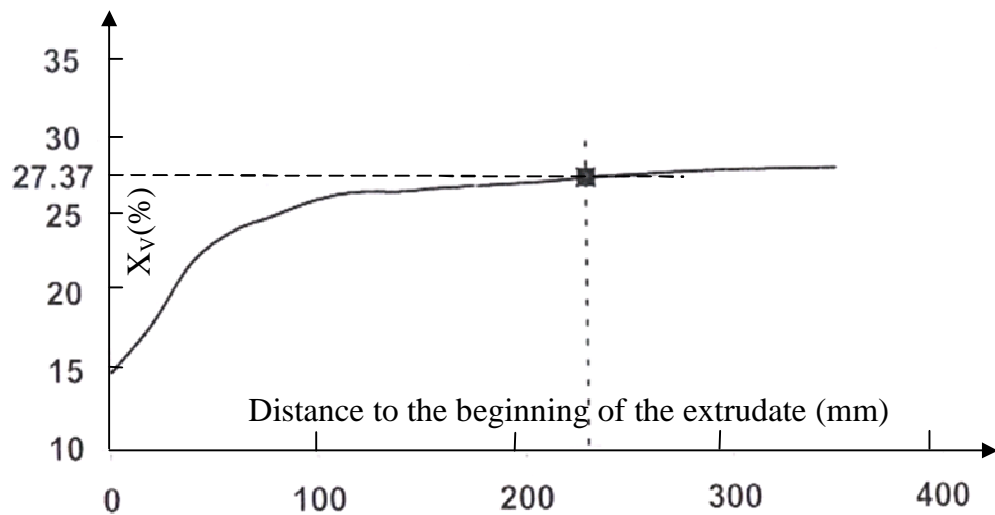


Figure 4.16 Predicted volume fraction recrystallised factor (X_v) along the extrudate surface and the selected point

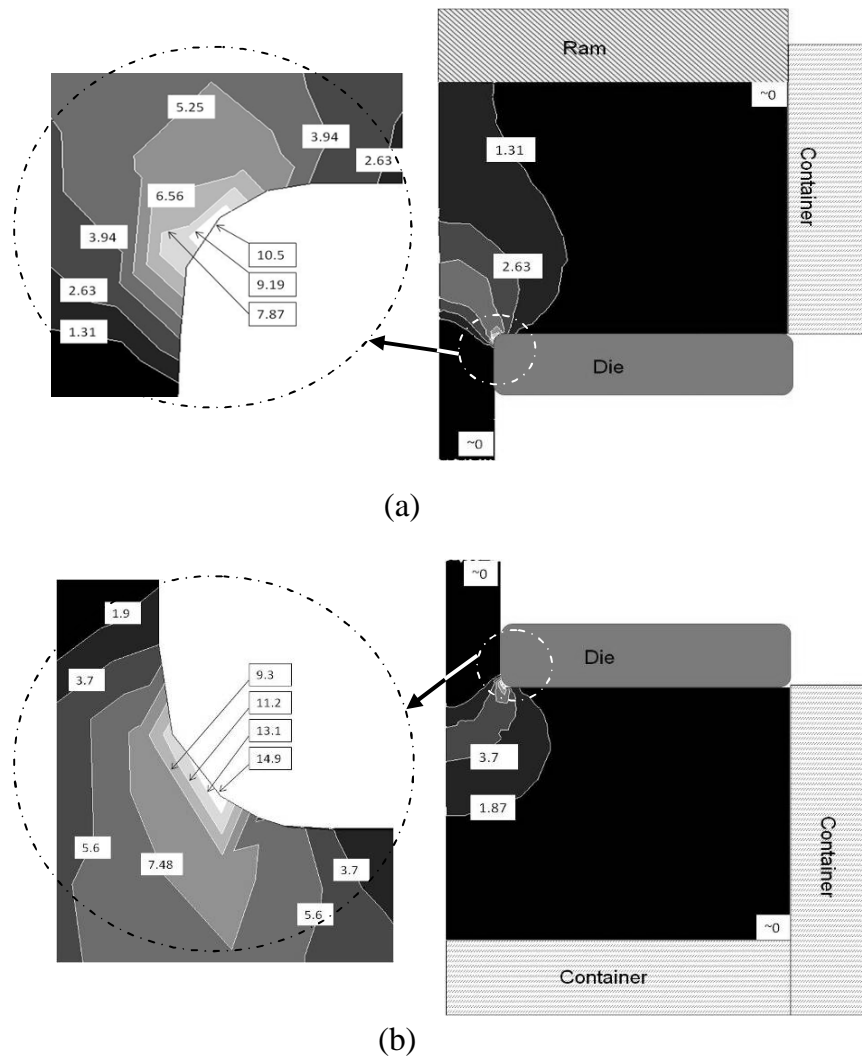


Figure 4.17 Distribution of parameter $Z (\times 10^{10})$ (a) direct and (b) indirect extrusions

In this study microstructure evolution for rod simulation will not be repeated. Efforts will be focussed on the investigation of microstructure evolution modelling of the more complicated sections. Nonetheless it is worthwhile to study the Zener-Hollomon parameter during extrusion process because it appears in many of the analyses necessary to determine the structure within the extrudate since it largely determines the subgrain size and by incorporating the ‘Holt’ relationship may also predict the dislocation density (Sheppard and S.J. Paterson 1982). Figure 4.17 shows the distribution of this parameter throughout the partially extruded billet at

65mm of ram travel. In direct extrusion in the vicinity of the die entry the parameter is at its maximum whilst in the dead metal zone the values are low. They are also of smaller magnitude at the rear of the billet. The fact that they exhibit values above zero is an anomaly caused by the temperature since the strain rate is very close to zero in these regions. The same comments apply to the indirect case where the die face and the material are the blocker/billet interface exhibit low values. This presents a problem in the incremental calculation of structural parameters (i.e. subgrain size, dislocation density, and misorientation).

This is thus one more fertile research area. Figure 4.17 indicates substantial differences in the Z parameter during direct versus indirect extrusion modes. Thus, it may be safely concluded that structure and properties resulting from the alternative processes will also vary.

4.7 Concluding remarks

In this chapter Forge[®] was fully validated with experimental results using both the author's and other workers' results. Several conclusions can be suggested:

1. Forge[®] is a powerful FEM software that can accurately predict the load variation, temperature change, metal flow and with proper models microstructure evolution can also be successfully simulated during extrusion.
2. The pressure and temperature loci analysed for the both direct and indirect processes indicate that, for the indirect mode, productivity may be increased by utilising an extended ram stroke producing a slimmer discard. The values predicted for the predicted pressure necessary to produce the extrudate was very close to the experimental value. Predicted contours for iso-temperature are also very sensible.
3. The origins of the surface of the extrudate are significantly different

between the two modes of extrusions. For the direct extrusion the original billet surface can be seen to reside either in the discard or in the dead metal zone at conclusion of the ram stroke. The surface is formed from the regions subcutaneous to the billet surface and located in a position between the experimental sensors defined by columns 1 and 2. In the indirect extrusion the surface is largely formed from the original billet face and not from the billet surface material (which is most generally accepted).

4. The predicted distribution of the Zener parameter is acceptable and varies in the differing modes. It is concluded that incremental calculation of substructural parameters requires intensive study and with a suitable model other microstructure parameter can be acquired from the Zener parameter.

5. Complex solid section extrusion simulation and integrated microstructure prediction

5.1 Introduction

One of the advantages of extrusion is to efficiently manufacture products with complex solid cross-sections. This chapter deals with the simulation of complex solid section extrusion and can be divided into two parts: 1) the establishment of the mathematical models for the microstructure evolution during extrusion and 2) the simulation of complex solid sections. The extrusion load, temperature evolution, material flow and surface formation mechanism of solid sections were predicted by FEM. The FEM results were then compared with experimental results. Microstructure evolution models were selected and then integrated with the FEM simulations. The results for simulated microstructure were compared with experimental measurements.

5.2 Mathematical model and the determination of the relevant parameters

5.2.1 Volume fraction recrystallised X_V

A great deal of effort has been expended on the analysis of the isothermal kinetics of recrystallisation, in the hope that this would cast indirect light on the mechanisms involved. In particular, it was hoped in this way to derive separate values for the nucleation rate, N , and the growth rate, G . Since these quantities themselves are often a function of time and G may be anisotropic, and moreover the analysis must allow for the mutual interference of growing grains in the later stages of recrystallisation, this type of analysis has rarely been fruitful. Most investigators agree on a resultant equation of the form (Cahn and Haasen 1996, p.2421):

$$X_V = 1 - \exp(-Bt^k) \quad (5.1)$$

where X_V is the fraction recrystallised, t is the holding time, B and k are constants. If t_{50} is the time to 50% recrystallisation from equation (5.1)

$$B = -\frac{\ln 0.5}{(t_{50})^k} \quad (5.2)$$

Combining equations (5.1) and (5.2), a most widely used Avrami equation is acquired:

$$X_V = 1 - \exp\left\{\frac{\ln 0.5}{(t_{50})^k} t^k\right\} = 1 - \exp\left\{-0.693 \left(\frac{t}{t_{50}}\right)^k\right\} \quad (5.3)$$

Where values of k are the most commonly in the range 1 to 2 (Cahn and Haasen 1996, p.2421). With constant growth rate in three dimensions n should be 3 and 4 for the site saturation and Johnson-Mehl (time-dependent) case, respectively (Humphreys and Hatherly 2004, p.233).

5.2.2 Time to 50% recrystallisation t_{50}

For the calculation of the time to 50% recrystallisation, t_{50} , in equation (5.3), the physical model is generally regarded as revealing the mechanics driving the transformation. t_{50} then can be calculated by (Vatne *et al.* 1996)

$$t_{50} = \frac{C_t}{M_{GB} P_D} \left(\frac{1}{N_V}\right)^n \quad (5.4)$$

where P_D is the stored energy per unit volume, M_{GB} is the grain boundary mobility, N_V is the nucleation sites per unit volume, n is a constant of $\frac{1}{3}$ on the assumption that the grain growth is homogeneously three dimensional. $\frac{C_t}{M_{GB}}$ is considered as a constant for a given deformation and temperature (Furu *et al.* 1999; Talamantes-

Silva *et al.* 2009). In their study of an Al-1% Mg alloy, values for $\frac{C_t}{M_{GB}}$ are 3.07×10^{11} at 385°C and 7×10^{10} at 400°C, respectively. However $\frac{C_t}{M_{GB}}$ is obviously not a constant when the temperature is clearly varying during deformation and will vary with each individual deformation process. One possible solution would be to incorporate C_t into the pre-exponential factor, M_0 in equation (5.5) since this constant must be temperature independent. Clearly this is an expedient but pragmatic solution and will produce a useable function in which C_t can be assumed to be unity.

5.2.3 Grain boundary mobility M_{GB}

M_{GB} , however, is temperature dependent (ignoring its orientation dependence) which is usually assumed to follow an Avrami-type behaviour

$$M_{GB} = M_0 \exp\left(\frac{-Q_{GB}}{RT}\right) \quad (5.5)$$

where M_0 is a constant better known as the prefactor of grain boundary mobility, Q_{GB} is the activation energy for grain boundary migration, R is the universal gas constant and T is the temperature in Kelvin.

A variant of the equation (5.5) is

$$M_{GB} = \frac{M_0}{T} \exp\left(\frac{-Q_{GB}}{RT}\right) \quad (5.6)$$

Although some researcher have used the equation (5.6) with an explicit temperature dependent prefactor (Janssens *et al.* 2007, p.112; Vatne *et al.* 1996), much more common practice is the use of equation (5.5) (Abbod *et al.* 2007; Huang and Humphreys 1999, 2000; Lens *et al.* 2005). There are three major

reasons for this:

- 1) under a wide range of practical conditions, the weak temperature dependence of the pre-exponential factor is negligible compared to the temperature dependence of the $\exp\left(\frac{-Q_{GB}}{RT}\right)$ factor;
- 2) the explicit temperature dependence of the prefactor makes determining the prefactor and activation energy from experimental data more complicate;
- 3) one most important reason is that Huang and Humphreys (1999, 2000) concluded that the equation (5.5) is valid to describe the migrations for both High Angle Grain Boundary (HAGB) and Low Angle Grain Boundary (LAGB) for aluminium alloys.

In Huang and Humphreys' (2000) study the mobility results are as follows

Material	Misorientation	M_0 ($\text{m}^4/\text{J s}$)	Q (kJ/mol)
30C	2.6	0.0005	134
30C	3.8	0.0038	134
70C	3.7	0.0019	134
70C	4.6	0.010	134
70H	4.5	0.005	134
70H	5.6	0.028	134
All	40° (tilt)	251	152
All	40° (twist)	25	152

Table 5.1 Mobilities of high and low angle grain boundaries

In Table 5.1 C means the experiment temperature is 20°C, H, 350°C.

Much attention was given to high purity aluminium alloys (Huang and Humphreys 1999; Lens *et al.* 2005) probably because it is more convenient for researchers to quantitatively and qualitatively ascertain the effect of a certain solute on the grain boundary mobility. Huang and Humphreys (1999) tended to support the opinion that such activation energy is controlled by the lattice diffusion of the solute

atmosphere although they also admitted the situation may be more complicated when it comes to the effects of solutes on the migration of high mobility boundaries whereas Lens *et al.* (2005) claimed that the activation energy for boundary migration is intermediate between that of solute diffusion in the lattice and along the grain boundaries.

Below are the results from Lens *et al.*(2005)

		$V(\times 10^9 ms^{-1})$	$P(KJ/m^3)$	$M(\times 10^{-14} m^4/Js)$	$M_0(m^4/Js)$	$Q(KJ/mol)$
Al0.1Mn	Std Rex	141	370	38	2.71	136
	Slow Rex	3.7	370	1.0	75.33	168
	Rapid Rex	1260	370	340	-----	-----
Al0.3Mn	Std Rex	6.6	440	1.5	0.09	135

Table 5.2 Estimation of the migration parameters at 280°C

In the Lens' study the typical behavior of the majority of the grain boundary migration experiments is denoted 'Standard Rex' (shown as 'Std Rex' in Table 5.2), in some experiments the phenomena that grain boundary migration is slower or even there is no recrystallisation at all is called 'Slow Rex' and very fast recrystallisation is referred as 'Rapid Rex. Obviously what matters more are the values about the more common 'Standard Rex' instead of the other two categories. However it is found that Lens' data is only about HAGB while Huang and Humphreys' data is more comprehensive and includes both HAGB and LAGB. In fact Lens also confirmed that one of his HAGB results is close to Huang and Humphreys' mobility values of $40^\circ \langle 111 \rangle$ representing the behaviour of 'random' high angle boundaries. This, coupled with the fact that Huang and Humphreys' data are of the same order with values from previous workers' estimations of $\frac{C_t}{M_{GB}}$ (Furu *et al.* 1999; Talamantes-Silva *et al.* 2009), further proves Huang and Humphreys' data is reliable. In Huda and Zaharinie's (2008) work kinetics of grain growth in a 2024-T3 heat-treated alloy was studied and the experimentally measured value of the activation energy of grain boundary migration in AA2024

alloy was calculated using below relations:

$$D^m - D_0^m = Gt \quad (5.7)$$

$$\log(D - D_0) = \log k - \frac{1}{m} \log t \quad (5.8)$$

$$G = G_0 \exp\left(-\frac{Q_{GB}}{RT}\right) \quad (5.9)$$

where D_0 is the pre-growth grain diameter, D is the grain diameter at any instant, t , during grain growth, G is the grain growth rate, G_0 is a constant, m is grain-growth exponent and k is a constant. From the experimental data, a value of 157 kJ/mol of the activation energy for grain growth was also calculated from the graph of $\ln G$ versus the reciprocals of three annealing temperatures (523K, 573K and 623K). Note that the unit for M_0 in equation (5.5) is different from the G_0 in the equation (5.9) although they have the same form.

It is widely accepted that the boundaries dominating the recrystallisation process are high angle boundaries, which is consistent with the values for the activation energy of grain growth. Its value from Huda and Zaharinie's experiment 157 kJ/mol would be reasonable because it is generally accepted that the rate determining mechanism in dynamic recovery is that of vacancy diffusion and a value of 153 kJ/mol for lattice self-diffusion even in highly alloyed aluminium has been established (Sheppard and Jackson 1997). Many reviews and studies in hot working aluminium alloys report activation energies of about 157 kJ/mol for hot working (Mcqueen 1977; Sheppard and Jackson 1997). It is also well recognised that alloy additions could decrease the grain boundary mobility of metals, therefore, instead of a M_0 from those papers, a much smaller value would be used in this study.

5.2.4 N_V and C_d in the equation (5.10)

During recrystallisation the phenomenon that the nucleation rate decreases so rapidly that all nucleation events effectively occur at the start of recrystallisation is termed site saturated nucleation (Humphreys and Hatherly 2004 , p233). Near-site saturated nucleation applies to the recrystallisation after hot deformation of aluminium has been confirmed experimentally and applied into the modelling and simulation of its recrystallisation process (Daaland and Nes 1996; Duan and Sheppard 2003b; Furu *et al.* 1999; Rossi and Sellars 1997; Vatne *et al.* 1996). Therefore

$$N_V = C_d \frac{S_V}{\delta^2} \quad (5.10)$$

where δ is the subgrain size, S_V is the grain boundary area per unit volume, C_d is a constant which has been acquired by first using nucleation models from Vatne *et al.*(1996) and Sellars (1997) to get $\frac{C_d}{\delta^2}$, then substituting experimental data at a strain rate of $2.5s^{-1}$ to get C_d , whose value is 1.48×10^{-4} (Furu *et al.* 1999). But Duan and Sheppard (2003b) have a value of 2.6×10^{-6} for C_d without reference that however could be more suitable for extrusion simulation while they used 0.0004 for rolling simulation of aluminium alloy AA5083 (Duan and Sheppard 2002a). 2.6×10^{-6} for C_d will be used in current study.

According to Vatne *et al.*'s work (1996) the procedure for the estimation of C_d is as follows, first N_V , S_V and d_{rex} were calculated using expressions from Mcqueen's (1977) work as below:

$$N_V = C_d f(\delta) S_V \quad (5.11)$$

$$S_V = \frac{2}{d_0} \{ \exp(\varepsilon) + \exp(-\varepsilon) + 1 \} \quad (5.12)$$

$$d_{rex} = \left(\frac{1}{N_V} \right)^n \quad (5.13)$$

where $f(\delta)$ is a function of subgrain size which will be determined later to be $\frac{1}{\delta^2}$, d_{rex} is the recrystallised grain size. Therefore first, N_V , assuming $n = 1/3$, can be calculated by the equation (5.13) using the measured d_{rex} from experiment; next, at a strain which is bigger than needed for the subgrain to reach a steady state (i.e. the subgrain size is a constant) when at a given strain rate, the $f(\delta)$ and S_V would be constants, therefore $C_d f(\delta)$ is obtained also as a constant; then, using the empirical equation (2.19) (Zaidi and Sheppard 1982) represented below

$$\frac{1}{\delta_{ss}} = A \ln Z + B \quad (5.14)$$

(where $Z = \dot{\epsilon} \exp(Q_{def}/RT)$ is the Zener-Hollomon parameter, δ_{ss} is the steady state subgrain size, A and B are constants) to estimate δ_{ss} ; finally a graph of $\log(C_d f(\delta))$ against $\log(\delta_{ss})$ was made, on the assumption of $f(\delta) = \left(\frac{1}{\delta_{ss}}\right)^2$, the constant C_d hence was determined.

5.2.5 Grain boundary surface area per unit volume S_V

For plane strain compression, representing the undeformed grains as cubes, the grain boundary area per unit volume can be expressed by equation (5.12) that can be used for rolling simulation. Although cube shape grain simplifies the mathematical analysis and the equation (5.12) is easy to use in FEM simulation, it cannot be used in more complex extrusion simulation because it is clear that cubes are poor approximations to the shapes of real grains.

Tetrapentahedra have sections with better space-filling geometry that

approximates closely to grain shapes observed metallographically.

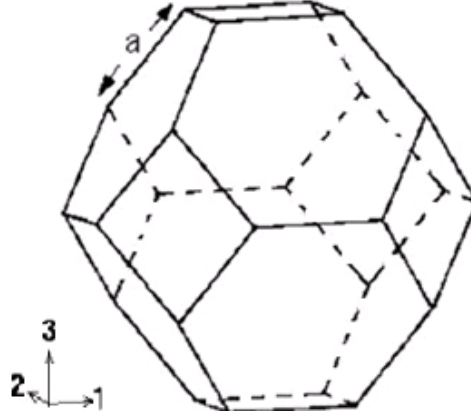


Figure 5.1 Tetrakaidecahedron (Zhu *et al.* 2007)

A general deformation matrix (engineering strain) S acts on a vector u to give a new vector v as follows (Zhu *et al.* 2007)

$$\begin{pmatrix} S_{11} & S_{12} & S_{13} \\ S_{21} & S_{22} & S_{23} \\ S_{31} & S_{32} & S_{33} \end{pmatrix} \begin{pmatrix} u_1 \\ u_2 \\ u_3 \end{pmatrix} = \begin{pmatrix} v_1 \\ v_2 \\ v_3 \end{pmatrix} \quad (5.15)$$

According to Zhu's work, in axisymmetric tension deformation (extrusion, wire drawing and rod rolling), $S_{22} = S_{33}$ and volume conservation requires that $S_{22} = \sqrt{S_{11}}$. For the tetrakaidecahedron oriented as in Figure 5.1

$$\frac{S_V}{S_{V_0}} = \frac{(3S_{11})^{\frac{1}{2}} + \left(\frac{2}{S_{11}^2} + S_{11}\right)^{\frac{1}{2}} + \frac{1}{3} + \frac{1}{3}\left(\frac{2}{S_{11}^2} + 2S_{11}\right)^{\frac{1}{2}}}{1 + 2\sqrt{3}} \quad (5.16)$$

where S_{V_0} is the grain surface area at zero strain.

$$S_{V_0} = \frac{3(1 + 2\sqrt{3})}{8\sqrt{2}a} \quad (5.17)$$

$$\varepsilon_{11} = \ln(S_{11}) \quad (5.18)$$

in which a is the length of the edge of the tetradekahedron.

Combining equations (5.16), (5.17) and (5.18),

$$S_V = \frac{3(1 + 2\sqrt{3})}{8\sqrt{2}a} \frac{(3e^{\varepsilon_{11}})^{\frac{1}{2}} + \left(\frac{2}{(e^{\varepsilon_{11}})^2} + e^{\varepsilon_{11}}\right)^{\frac{1}{2}} + \frac{1}{3} + \frac{1}{3}\left(\frac{2}{(e^{\varepsilon_{11}})^2} + 2e^{\varepsilon_{11}}\right)^{\frac{1}{2}}}{1 + 2\sqrt{3}} \quad (5.19)$$

The equation (5.19), only applies for axisymmetric extrusion, which should not be used as an approximation for complex shape extrusion.

However from a stereological point of view, the mean linear intercept representing the unreformed grain size measured on two-dimensional sections becomes

$$\bar{L}_0 = \frac{2}{S_{V_0}} \quad (5.20)$$

For a deformed grain, given that the number of boundaries per unit length $N_{L1} \leq N_{L2} \leq N_{L3}$, the surface area per unit volume is (Underwood 1970)

$$S_V = 0.429N_{L1} + 0.571N_{L2} + N_{L3} \quad (5.21)$$

and since $\bar{L} = 1/N$, for plastic deformation in which $\varepsilon_{11} \geq \varepsilon_{22} \geq \varepsilon_{33}$, the linear intercept are

$$\begin{cases} \bar{L}_1 = \bar{L}_0 \exp(\varepsilon_{11}) \\ \bar{L}_2 = \bar{L}_0 \exp(\varepsilon_{22}) \\ \bar{L}_3 = \bar{L}_0 \exp(\varepsilon_{33}) \end{cases} \quad (5.22)$$

so that

$$\begin{aligned} S_V &= (\bar{L}_0)^{-1} \{0.429 \exp(-\varepsilon_{11}) + 0.571 \exp(-\varepsilon_{22}) + \exp(-\varepsilon_{33})\} \\ &= \frac{1}{2} S_{V_0} \{0.429 \exp(-\varepsilon_{11}) + 0.571 \exp(-\varepsilon_{22}) + \exp(-\varepsilon_{33})\} \\ &= \frac{3(1+2\sqrt{3})}{16\sqrt{2}a} \{0.429 \exp(-\varepsilon_{11}) + 0.571 \exp(-\varepsilon_{22}) + \exp(-\varepsilon_{33})\} \end{aligned} \quad (5.23)$$

Equation (5.23) will be used to calculate grain boundary area per unit volume in this study. The equation (5.12) cannot be used for complex irregular section extrusion. Its derivation can be found in Appendix C.

5.2.6 The stored energy P_D

The total stored energy per unit volume (U) arises mainly from the dislocation density (ρ) and the energy per unit length of dislocation line (E), and recovery can be considered to reduce stored energy as

$$dU = E d\rho + \rho dE \quad (5.24)$$

The first term arises from reduction of dislocation density, e.g. by growth of links and annihilation by dislocations of opposite sign. The second term arises from a reduction in energy per unit length by polygonisation, which can be simply estimated from the standard relationships for elastic energy of distributed edge dislocation (Dieter 1987, p.163)

$$E_{el} = E_0 \ln \left(\frac{r_1}{r_0} \right) \quad (5.25)$$

where $E_0 = \frac{Gb^2}{4\pi(1-\nu)}$, G is the shear modulus, ν is Poisson's ratio and b is the magnitude of Burgers vector.

Taking the outer cut-off radius, r_1 , as $0.5\bar{l}$ (\bar{l} , the mean link length $\approx \rho^{-\frac{1}{2}}$) and the core radius as $5b$ (Read and Shockley, 1950, Humphreys and Hatherly 2004, p.95), with the core energy $E_{core} \approx Gb^2/10 \approx E_0$ (Dieter 1987, p.163), leads to a total energy per unit length for dislocations in the matrix

$$E_m = E_{core} + E_{el} \approx E_0 \left(1 + \ln \left(\frac{r_1}{r_0} \right) \right) = E_0 \left(1 + \ln \left(\frac{0.5\rho_i^{\frac{1}{2}}}{5b} \right) \right) = E_0 (1 - \ln 10b\rho_i^{\frac{1}{2}}) \quad (5.26)$$

For dislocations in low angle tilt boundaries the energy per unit length

$$E_{sb} \approx E_0 \left(1 - \ln \left(\frac{\theta}{\theta_c} \right) \right) \quad (5.27)$$

where θ is the angle of misorientation and $\theta_c \approx 15^\circ \approx 0.25$ radian, r_0 is the radius of dislocation core, usually taken as between b and $5b$ (Hirth and Loath 1982, p.741; Humphreys and Hatherly 2004, p.95).

For a simple low angle tilt boundary, the misorientation can be related to an equivalent distributed dislocation density ρ_e

$$\theta = b/h = b\delta\rho_e \quad (5.28)$$

$$\rho_e = \theta/b\delta \quad (5.29)$$

where h is dislocation spacing in the boundary and δ is the subgrain size.

Therefore the energies per unit volume for internal dislocations and for subgrain

boundaries from above equations are

$$U_i = E_m \rho_i = E_0 (1 - \ln 10 b \rho^{-\frac{1}{2}}) \rho_i = \frac{G b^2}{4\pi(1-\nu)} (1 - \ln 10 b \rho_i^{\frac{1}{2}}) \rho_i \approx \frac{G b^2}{10} (1 - \ln 10 b \rho_i^{\frac{1}{2}}) \rho_i \quad (5.30)$$

$$U_{sb} = E_{sb} \cdot 2\rho_e = E_{sb} \frac{2\theta}{b\delta} = E_0 \left(1 - \ln \left(\frac{\theta}{\theta_c}\right)\right) \frac{2\theta}{b\delta} = \frac{G b^2}{4\pi(1-\nu)} \left(1 - \ln \left(\frac{\theta}{\theta_c}\right)\right) \frac{2\theta}{b\delta} \approx \frac{G b^2}{10} \left(1 - \ln \left(\frac{\theta}{\theta_c}\right)\right) \frac{2\theta}{b\delta} \quad (5.31)$$

where the number before ρ_e is a geometric constant depending on the type of boundary (Sellars and Zhu 2000).

Finally, the total stored energy per unit volume (Sellars and Zhu 2000)

$$P_D \approx U_i + U_{sb} = \frac{G b^2}{10} \left(\rho_i (1 - \ln 10 b \rho_i^{\frac{1}{2}}) + \frac{2\theta}{b\delta} \left(1 - \ln \left(\frac{\theta}{\theta_c}\right)\right) \right) \quad (5.32)$$

5.2.7 The equations for evolutions for dislocation characteristics

5.2.7.1 Evolution of internal dislocation

5.2.7.1.1 Using Holt relation to calculate internal dislocation density and subgrain size at steady state

For steady state deformation, a generally recognised equation relating subgrain size to the internal dislocation density is written as:

$$\rho_i^{1/2} \delta_{ss} = C \quad (5.33)$$

where the subscript 'ss' stands for steady state, δ_{ss} is the subgrain size during steady state, C is a constant and 50 was used in this study.

Combining equations (5.14) and (5.33):

$$\rho_i^{1/2} = C(A \ln Z + B) \quad (5.34)$$

However equation (5.34) only applies to the steady state when the actions of work hardening and dynamic recovery reach a balance.

5.2.7.1.2 Evolution of internal dislocation at transient deformation state

The transient of dislocation evolution can be calculated in terms of dislocation density storage from working hardening and dislocation density decrease by recovery. During plastic deformation, internal ‘random’ dislocations are created by work hardening and annihilated by dynamic recovery. The plastic strain increase and the dislocation density storage can be related by Orowan equation:

$$d\varepsilon = \frac{b}{M} \Lambda_r d\rho_r^+ \quad (5.35)$$

where b is the magnitude of Burgers vector, M is the Taylor factor and Λ_r is the mean distance travelled by the dislocation before it is stopped. Here $\Lambda_r \propto \rho_r^{-1/2}$ is assumed.

At the same time, dislocation density decrease due to recovery may be described by (Nix *et al.* 1985):

$$d\rho_r^- = -\frac{2L_c \bar{v}_m \rho_r}{w} dt \quad (5.36)$$

where w is distance between the sites of cross-slip or climb events, L_c is the length of dislocations annihilated. For aluminium alloys $L_c/w \approx \text{constant}$ is acceptable. For Al-Mg alloys the mean velocity of mobile dislocation:

$$\bar{v}_m = Db\sigma_f/\beta \quad (5.37)$$

where D is the diffusion coefficient and β is the drag force, depending on the solute concentration and misfit in atomic size, and σ_f is the friction stress, effectively driving dislocation motion.

The total internal ‘random’ dislocation density is the balance between the increment due to strain hardening and annihilation due to recovery:

$$\begin{aligned} d\rho_r &= d\rho_r^+ + d\rho_r^- = \frac{M}{b\Lambda_r} d\varepsilon + -\frac{2L_c\bar{v}_m\rho_r}{w} dt = \frac{M}{b\Lambda_r} d\varepsilon + -\frac{2L_c\rho_r}{w} \cdot \frac{Db\sigma_f}{\beta} dt \\ &= \frac{M}{b\Lambda_r} d\varepsilon + -\frac{2L_c\rho_r}{w} \cdot \frac{D_0 \exp(-Q_{def}/RT) b\sigma_f}{\beta} dt \\ &= \frac{M}{b\Lambda_r} d\varepsilon + -\frac{2L_c\rho_r}{w} \cdot \frac{D_0 \exp(-Q_{def}/RT) b\sigma_f}{\beta} dt \\ &= \frac{M}{b\Lambda_r} d\varepsilon + -\frac{2L_c\rho_r}{w} \cdot \frac{D_0 \dot{\varepsilon} b\sigma_f}{Z\beta} dt = \frac{M}{b\Lambda_r} d\varepsilon + -\frac{2L_c\rho_r}{w} \cdot \frac{D_0 b\sigma_f}{Z\beta} d\varepsilon \\ &= \left(\frac{M}{b\Lambda_r} - \frac{2L_c D_0 b}{w\beta} \cdot \frac{\sigma_f}{Z} \rho_r \right) d\varepsilon = \left(\frac{M}{b\Lambda_r} - \frac{2L_c D_0 b}{w\beta} \cdot \frac{\sigma_f}{Z} \rho_r \right) d\varepsilon \end{aligned} \quad (5.38)$$

where $C_1 = \frac{M}{b}$ and $C_2 = \frac{2L_c D_0 b}{w\beta}$ are constants.

Two points to be noted about the equation:

- 1) At steady state deformation $d\rho = d\rho_r^+ + d\rho_r^- = 0$, therefore there is the relationship $C_2 = \left(\frac{Z}{\rho_r^{1/2} \sigma_f} \right)_{ss} C_1$;
- 2) The ratio $\frac{\sigma_f}{Z}$ can be assumed to be constant because of $\dot{\varepsilon} \propto \rho_r \sigma_f$ (Raj and Pharr 1986).

5.2.7.1.2.1 Evolution of geometrically necessary internal dislocation

Equation (5.38) can only be used to describe the evolution of ‘random’ internal dislocation density. To predict the total internal dislocation density, the ‘geometrically necessary’ dislocation density, ρ_g , which relates to the lattice curvature, must be taken into account. Baxter *et al.* (1999) observed that the subgrain structure was in the form of microbands with low misorientation subgrain boundaries within them and they concluded that the higher misorientation boundaries in the bands are geometrically necessary boundaries to accommodate local lattice curvatures. Assumed that the local lattice curvature arises both from the misorientation across these boundaries and from excess density of dislocations of the same Burgers vector within subgrains (geometrically necessary dislocations), Baxter *et al.* (1999) developed the model for the calculation of ρ_g shown as ρ_e in Figure 5.2.

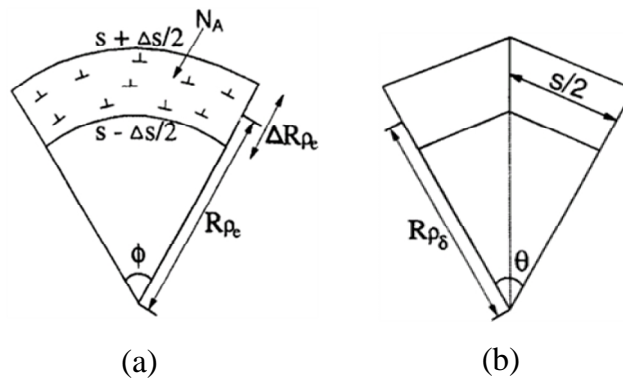


Figure 5.2 Relationships between local lattice curvature and (a) excess dislocations of a given Burgers vector and (b) subgrain boundary (microband) spacing and misorientation (Baxter *et al.* 1999)

In Figure 5.2, an area A of matrix in which there are N_A intersections per unit area of excess dislocation of a given Burgers vector b leads to a curvature of radius R_{ρ_e} (see Figure 5.2(a)) and there is a relation

$$\Delta s = \Delta R_{\rho_e} \phi = N_A A b$$

where $A = \phi R_{\rho_e} \Delta R_{\rho_e}$

hence

$$\frac{1}{R_{\rho_e}} = N_A b$$

Then considering a subgrain boundary between two subgrains shown in Figure 5.2(b)

$$\theta = \frac{b}{h} = b \bar{N}_L$$

where $h = 1 / \bar{N}_L$ is the spacing of dislocations in the subgrain boundary, \bar{N}_L is the number of intersections per unit length along the subgrain boundary.

And from Figure 5.2(b)

$$\tan\left(\frac{\theta}{2}\right) \cong \frac{\theta}{2} = \frac{\frac{1}{2}s}{R_{\rho_\delta}}$$

hence

$$\frac{1}{R_{\rho_\delta}} = \frac{\theta}{s} = \frac{b \bar{N}_L}{s}$$

therefore in two-dimension, the lattice curvature can be written as

$$\frac{1}{R} = \frac{1}{R_{\rho_{\delta}}} + \frac{1}{R_{\rho_e}} = N_A b + \frac{\bar{N}_L}{s} b$$

which can be rewritten as

$$\frac{1}{R} = \frac{1}{R_{\rho_{\delta}}} + \frac{1}{R_{\rho_e}} = \rho_e b + \rho_b b$$

where ρ_b is the dislocation density in the microband boundary. Finally according to experimental measurements, Baxter *et al.* (1999) modified the equation to relate misorientation, subgrain size, the geometrically necessary dislocation density and the local lattice curvature as below

$$\frac{1}{R} = \rho_e b + \frac{\bar{\theta}}{\delta} \quad (5.39)$$

Although Sellars and Zhu (2000) claimed that using equation (5.39), ‘the calculated data for the total internal dislocation density including and in reasonable agreement with experimental values for both constant and changing strain rate deformation’, doubt is cast about its application in extrusion. First because this equation largely based on the microband observed in rolling and plane strain compression at relatively small strains less than 2 while at large strains microband doesn’t appear to be encouraged; second substituting the data in Figure 5.3 and Figure 5.4 into equation (5.39) the geometrically necessary dislocation density $\rho_g = \left(\frac{1}{R} - \frac{\bar{\theta}}{\delta}\right) / b \cong \left(\frac{1}{5 \times 10^{-4}} - \frac{3.5 \times \pi}{180 \times 2.2 \times 10^{-6}}\right) / b = -2.5 \times 10^4 / b$ and a negative value for the dislocation density is impossible. The reason for this could be the model for ρ_g is over-simplified or the experimental data is wrong or maybe $\bar{\theta}$ can take a negative value when the curvatures are in opposite directions, which probably is a subject that needs more research. Since so far there is no reasonable explanation for this, it would not be meaningful to use this method to calculate the

internal dislocation density.

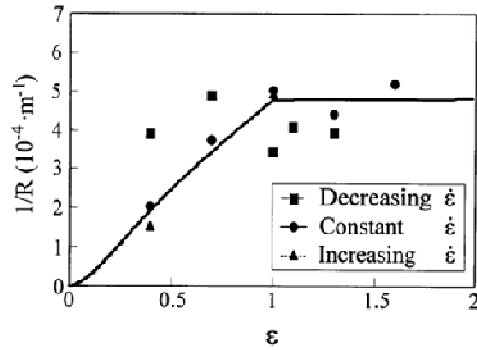


Figure 5.3 Local lattice curvature of Al-1%Mg deformed at 385°C (Sellars and Zhu 2000)

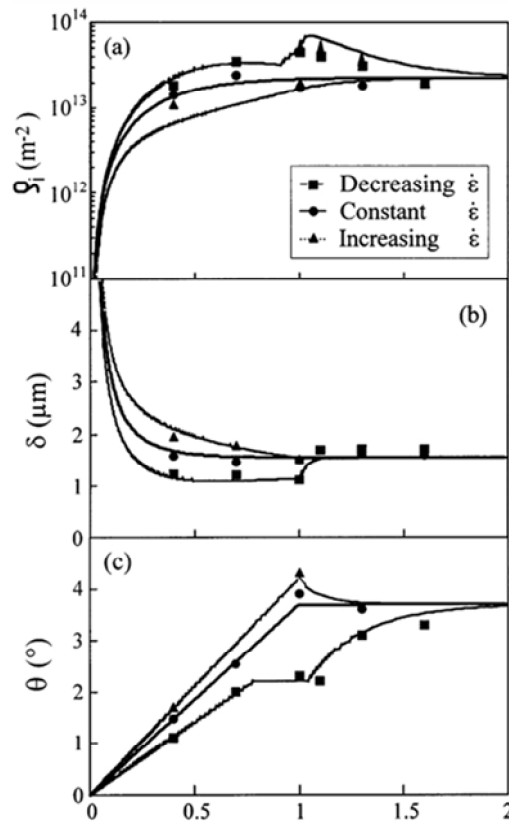


Figure 5.4 Comparison of calculated and experimental data of (a) internal dislocation density; (b) subgrain size and (c) misorientation between subgrains (Sellars and Zhu 2000)

5.2.7.1.2.2 Incremental equations for the evolution of subgrain structure

Zhu and Sellars (1996) noted that the observed microstructure was well approximated by an exponential evolution with strain and a general equation of the microstructure evolution was proposed as below

$$S_j = S_{j0} + (S_{js} - S_{j0}) \left[1 - \exp\left(-\frac{\varepsilon}{\varepsilon_{sj}}\right) \right], (\rho_i^{1/2}, 1/\delta, \theta) \quad (5.40)$$

The form of equation (5.40) can also be changed as follows (Zhu 1994)

$$S_j = S_{js} + (S_{j0} - S_{js}) \exp\left(-\frac{\varepsilon}{\varepsilon_{sj}}\right), (\rho_i^{1/2}, 1/\delta, \theta) \quad (5.41)$$

where ε_{sj} is a characteristic strain which controls the strain over which steady-state is reached, S_{j0} and S_{js} are the values of the microstructure state variable S_j at steady state before and after a change of deformation conditions.

In spite of a lack of theoretical analysis of the evolution of subgrain structure the semi-empirical equations (5.40) and (5.41) have been proved to be successful in modelling evolution of subgrain size and misorientation between subgrains during hot deformation at constant strain rate and temperature.

Substitute S with θ into equation (5.41), that is $\theta = \theta_{ss} + (\theta_0 - \theta_{ss}) \exp\left(-\frac{\varepsilon}{\varepsilon_\theta}\right)$ differentiate it with respect to ε ,

$$d\theta = \left(-\frac{1}{\varepsilon_\theta}\right) (\theta_0 - \theta_{ss}) \exp\left(-\frac{\varepsilon}{\varepsilon_\theta}\right) d\varepsilon = \left(\frac{1}{\varepsilon_\theta}\right) (\theta_{ss} - \theta) d\varepsilon \quad (5.42)$$

Likewise, if S is replaced by $\frac{1}{\delta}$, after differentiating, a similar form of equation (5.42) will be obtained:

$$d\left(\frac{1}{\delta}\right) = \left(\frac{1}{\varepsilon\delta}\right)\left(\frac{1}{\delta_{ss}} - \frac{1}{\delta}\right) d\varepsilon$$

$$\left(-\frac{1}{\delta^2}\right) d\delta = \left(\frac{1}{\varepsilon\delta}\right)\left(\frac{\delta - \delta_{ss}}{\delta_{ss}\delta}\right) d\varepsilon$$

$$\left(-\frac{1}{\delta^2}\right) d\delta = \left(\frac{1}{\varepsilon\delta}\right)\left(\frac{\delta - \delta_{ss}}{\delta_{ss}\delta}\right) d\varepsilon$$

Finally it becomes:

$$d\delta = \left(\frac{\delta}{\varepsilon\delta\delta_{ss}}\right) (\delta_{ss} - \delta) d\varepsilon \quad (5.43)$$

Equations (5.38), (5.42) and (5.43) can be also written in integral form:

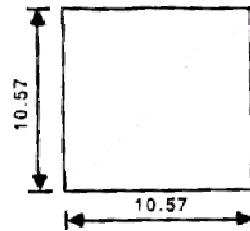
$$\rho_r = \int_0^\varepsilon \left(C_1 \rho_r^{1/2} - C_2 \cdot \frac{\sigma_f}{Z} \rho_r\right) d\varepsilon \quad (5.44)$$

$$\theta = \int_0^\varepsilon \left(\frac{1}{\varepsilon\theta}\right) (\theta_{ss} - \theta) d\varepsilon \quad (5.45)$$

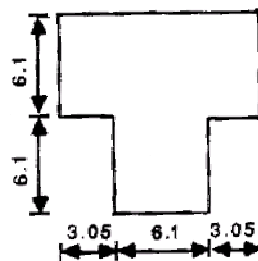
$$\delta = \int_0^\varepsilon \left(\frac{\delta}{\varepsilon\delta\delta_{ss}}\right) (\delta_{ss} - \delta) d\varepsilon \quad (5.46)$$

Their integration with FEM and the determination of the parameters will be discussed in following relevant sections.

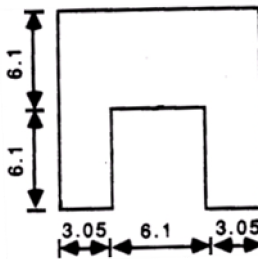
5.3 Simulation considerations



(a) Square



(b) T shape



(c) U shape

Figure 5.5 Dies geometries, dimensions in *mm* (Sheppard 1993)

Shape	ER	Mode	$T_i(^{\circ}\text{C})$	Ram speed(mm/s)	Peak load(NM)
Square	40:1	direct	350	5	4.38
T-shape	40:1	direct	350	7	4.58
U-shape	40:1	direct	350	5	4.71

Table 5.3 Experimental parameters and results

The shape extrusion experiments to be simulated are selected from

Subramaniyan's work (1989). The experimental parameters are shown in Table 5.3 in which ER means extrusion ratio and T_i the initial billet temperature. The press and material used are the same as those described in sections 4.2.2 and 4.2.3. The tooling is also basically the same and will not be repeated except that different dies were used and are shown in Figure 5.5.

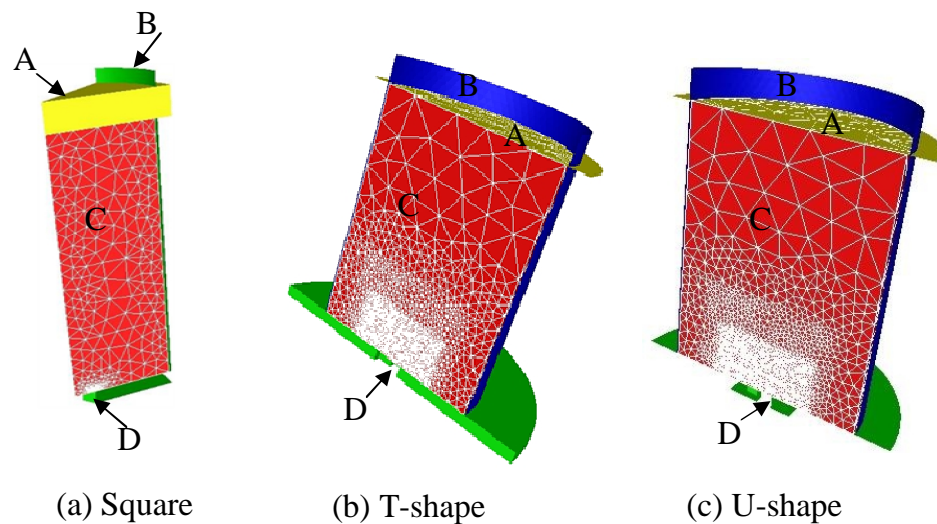


Figure 5.6 FEM configurations prior to simulation for (a) square, (b) T-shape and (c) U-shape where part A is the ram, part B, the container, part C the billet and part D the die (orifice)

The FEM models are shown in Figure 5.6 in which the tools (the ram, the container and the die) are modelled as rigid objects that will not deform. For the same reason as described in the 2D rod simulation that hot aluminium has rate dependent behaviour and the elastic deformations are small when compared with the large plastic deformations during extrusion, the viscoplastic constitutive model described by the equation (2.8) was used and the required constants can be seen in section 4.2.4. To shorten the calculation time the symmetric features of the problems studied were utilised. In Figure 5.6(a) only one-eighth of the actual billet was modelled in the square extrusion simulation whilst for the T-shape and U-shape simulations in Figure 5.6(b) and Figure 5.6(c) the FEM billets are half of the

real billet. To ensure the necessary accuracy and a successful simulation, ‘mesh box’ technique (i.e. regions enclosed by boxes were assigned with different mesh sizes) was used to get very fine mesh around the edges of die entry where severe deformation was expected. The acting mesh boxes can be seen from the very fine meshes near the die entries in Figure 5.6. The mesh box and the auto-trim settings are illustrated in Figure 5.7. All the elements 5mm below the die exit will be deleted since the microstructure of the material changes dramatically from the moment it enters into the die to the moment it goes out of the die exit. It has been proved to be an effective way to reduce the calculation time.

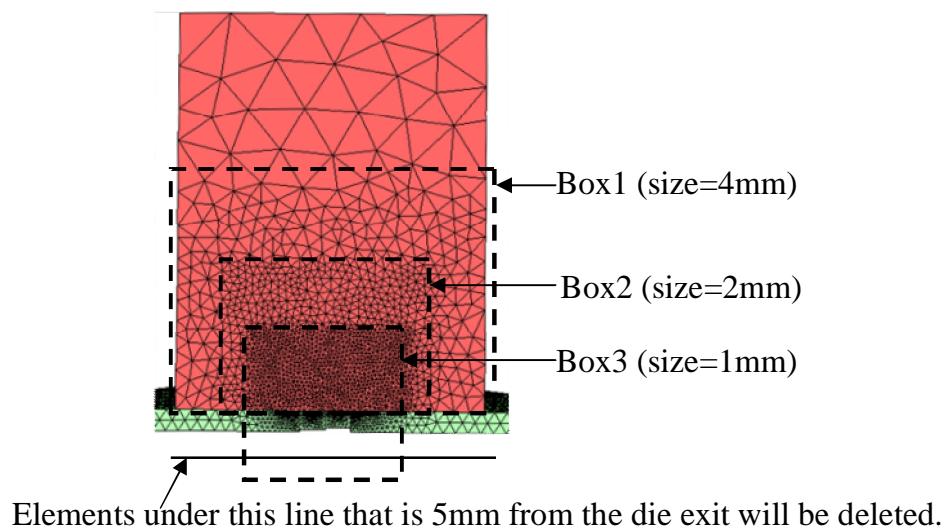


Figure 5.7 Schematic for multi mesh boxes and auto-trim settings

5.4 Simulated results of solid section extrusion

5.4.1 Load prediction

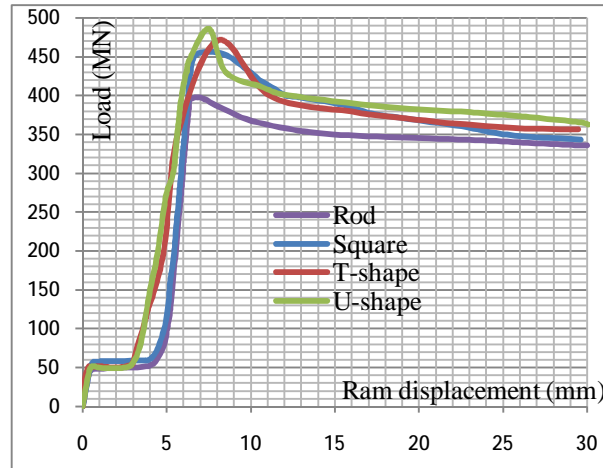


Figure 5.8 Predicted loads variations for different shape extrusions

The predicted load variations for different section extrusions are displayed in Figure 5.8. In addition, the predicted load vs. ram displacement in the Figure 4.4 for the direct rod extrusion was also represented here for discussion. Their comparisons with the experimental measurements are shown in Table 5.4.

	Rod	Square	T-section	U-section
Predicted load (MN)	3.9443	4.55	4.71	4.85
Experimental measurement (MN)	3.94	4.38	4.58	4.71
Difference (%)	0.1	3.7	2.8	1.2

Table 5.4 Predicted load results vs. experimental measurements

From the Table 5.4 it can be seen that generally speaking, the peak load can be accurately predicted for solid section extrusions. Figure 5.8 shows that within the first 1mm of the ram travel, for all cases the loads increase from zero to a level of about 0.5 MN that lasts for the next several millimetres of the ram displacement as the billet begins to upset. Following is a short ram displacement, during which the load increases rapidly to the peak, that actually can be divided into two stages: in

the first stage, the billets continue to upset to fully fill the containers and in the second the material was extruded out of the die passing through the die land and the peak load is reached. After the peak pressure has been reached the extrusion pressure falls as the billet length decreases until a steady state is realised.

Shape	λ
Rod	1
Square	1.16
T-shape	1.34
U-shape	1.68

Table 5.5 Peripheral ratios for different sections

The effect of the section shape on the load can be represented by the peripheral ratio, λ , defined as the ratio of the periphery of the section, Ω_s , to the periphery of a rod of equivalent cross-section, Ω_r (Wood and Sheppard 1975). By the definition the peripheral ratios were calculated as shown in Table 5.5.

The curves in Figure 5.8 clearly show that with same process conditions (billet size, initial temperature, extrusion ratio and ram speed) the extrusion pressure necessary to form complex sections increases with increasing peripheral ratio. Compared with the necessary pressure for the rod extrusion, it is mainly due to the extra forces required to overcome the additional shear resistance arising from the asymmetrical flow and more areas that contact the die land.

5.4.2 Strain, strain-rate and temperature distribution

Strain is one of the important variables in microstructure prediction that directly influence the calculation of the surface area per unit volume (S_V) of the grain. Compared with the equations (2.2) and (2.3) that only roughly estimate the strain and strain rate during extrusion, FEM is more reliable and accurate to calculate these process parameters.

At the ram displacement of 27mm, about one-third of the total ram travel, at which the steady state of extrusion is supposed to be realised, equivalent strain and strain rate and temperature data for different shape extrusions were captured and shown in Figure 5.9, Figure 5.10 and Figure 5.11 respectively.

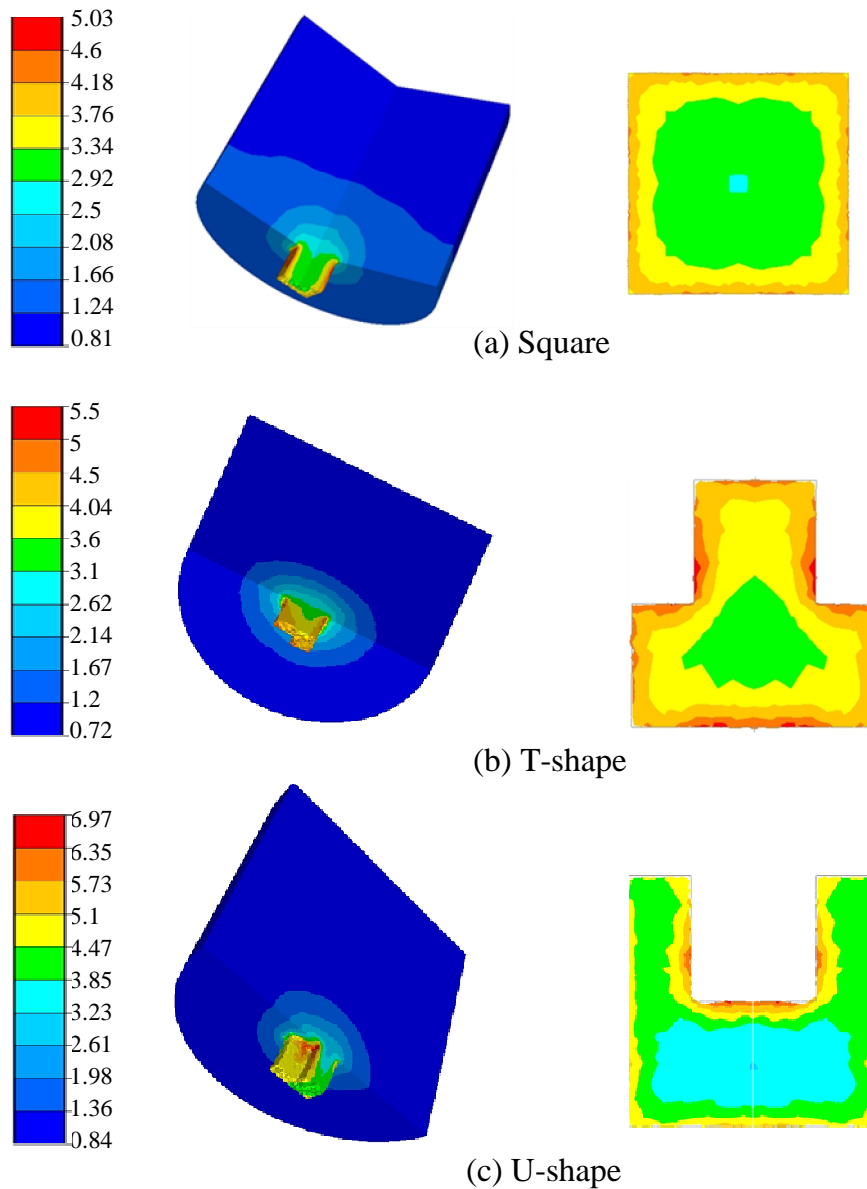


Figure 5.9 Equivalent strain distribution during steady state

In Figure 5.9 it can be seen that for all cases the equivalent strain distributions are

in the same pattern throughout the billets: the further the material is from the die entry, the smaller the equivalent strain is. For a clearer understanding of areas of interest, their corresponding distributions cross their cross-section below the die entry are shown side by side as well. Because of the same extrusion ratio, the predicted strain values are within a similar range. However as the complexity (denoted by the peripheral ratio, λ) increases, the maximum equivalent strain appears to increase and normally it happens in places where sharp corners exist and more severe deformation takes place.

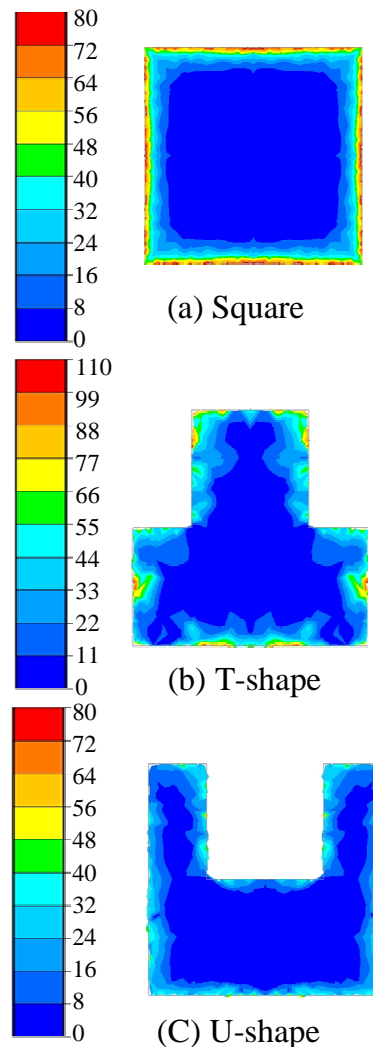


Figure 5.10 Strain rate (s^{-1}) distributions on the cross-sections

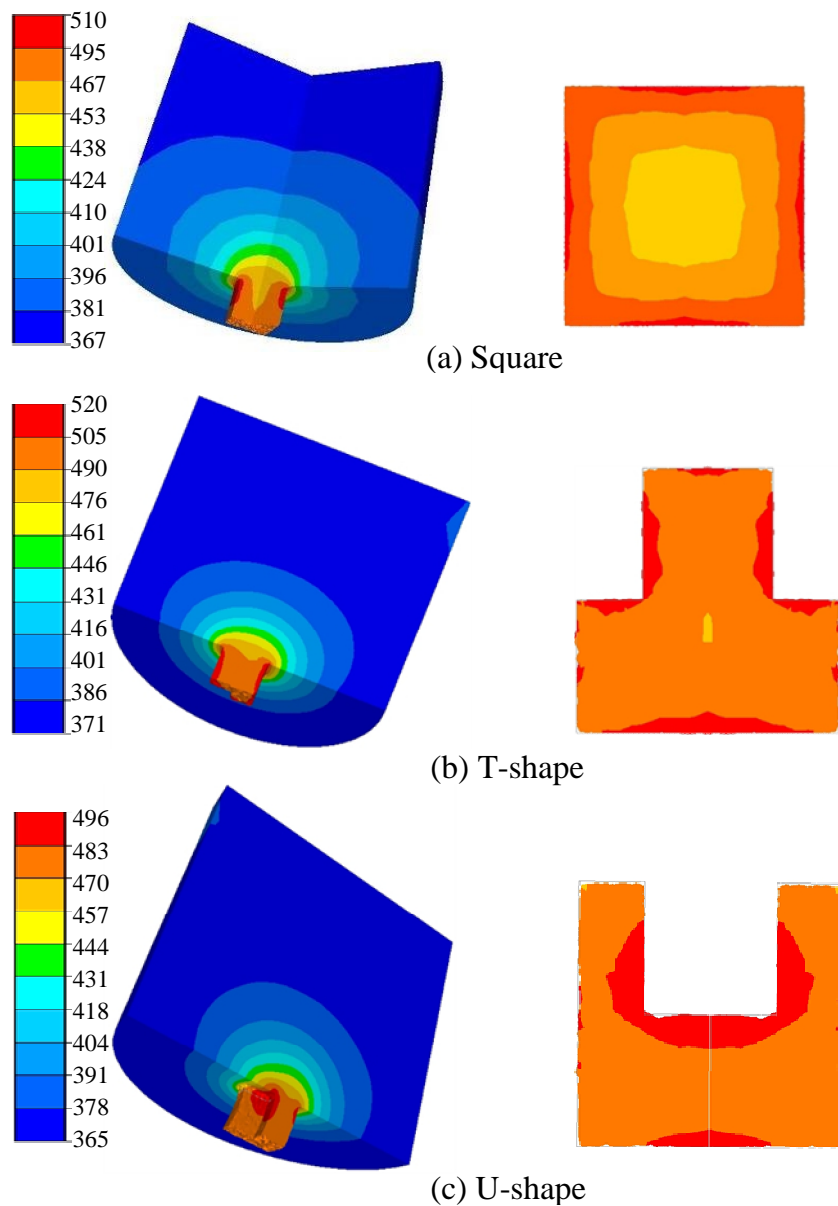


Figure 5.11 Temperature ($^{\circ}\text{C}$) distributions of different shape extrusions

The strain-rate is a crucial parameter because it appears in many analyses necessary to determine the structure within the extrudate. In Figure 5.10 only the strain-rate distributions on the cross-sections are presented because during steady state, the strain rate is nearly zero all over the billet except near the areas where the material approaches the die entry the strain-rate values change dramatically. Once

the material enters the die land, they drop rapidly to nearly zero again. The highest values appear around the profiles of the different shapes and the strain-rate is zero in the central areas. Furthermore, the value ranges of similar for the same reason of the same extrusion ratio and similar ram speed. T-shape cross section has higher values because its extrusion has a greater ram speed (see Table 5.3).

Temperature is another important variable that determines the Zener-Hollomon parameter together with the strain-rate and has great influence on the surface quality of the extruded product. In Figure 5.11 the farther from the die entry the smaller the value rule still applies for temperature distribution as that in the rod extrusion, but the temperature on the cross-section is not equally distributed along its contour mainly due to the irregular shape of the extrudate resulting in the inhomogeneous deformation. The similarity between Figure 5.9 and Figure 5.11 indicates the strong connection of the temperature rise and the deformation.

5.4.3 Material flow analysis

In this section, the grid method was used to study metal flow. A more figurative surface method that can disclose the 3D movement of arbitrary surface inside the billet was also employed.

Figure 5.12 shows the positions of the initial grids in different sections used for metal flow analysis. They are all in the middle of the billet and go through the symmetry planes of the dies. Their initial grid is the same of all the three sections and is shown in Figure 5.12(d).

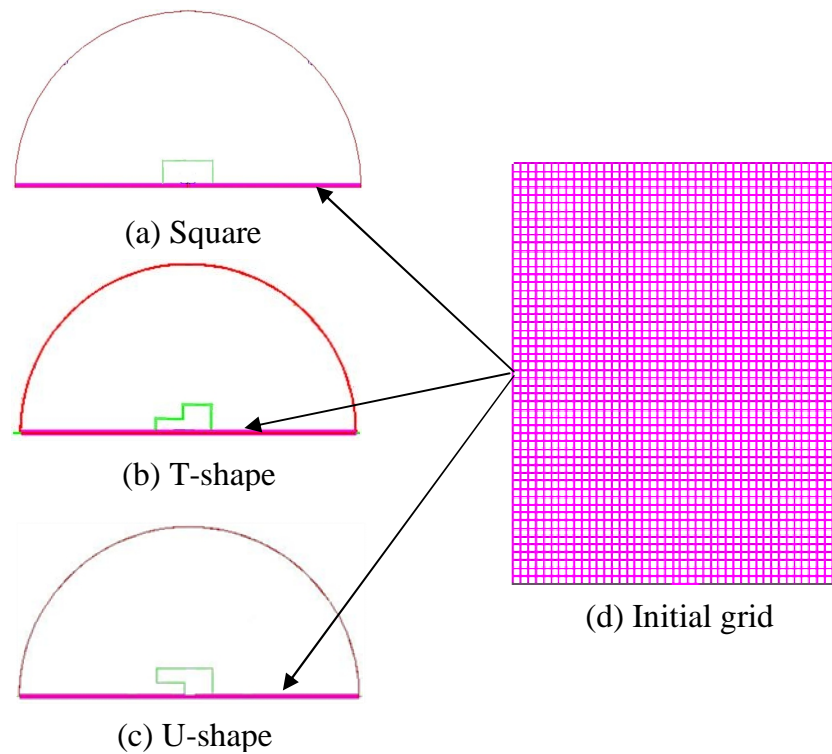


Figure 5.12 Grid section for metal flow study

Figure 5.13 displays the metal flows for different section extrusions that are represented by deformed grids. Three ram displacements, 10mm, 40mm and 80mm, were selected for each extrusion. Figure 5.13 (a), (b) and (c) are displaced grid patterns for square extrusion at the ram travel of 10mm, 40mm and 80mm, respectively. Likewise Figure 5.13 (d), (e) and (f) are for U-section extrusion and Figure 5.13 (g), (h) and (i) are for T-section extrusion at corresponding ram displacements.

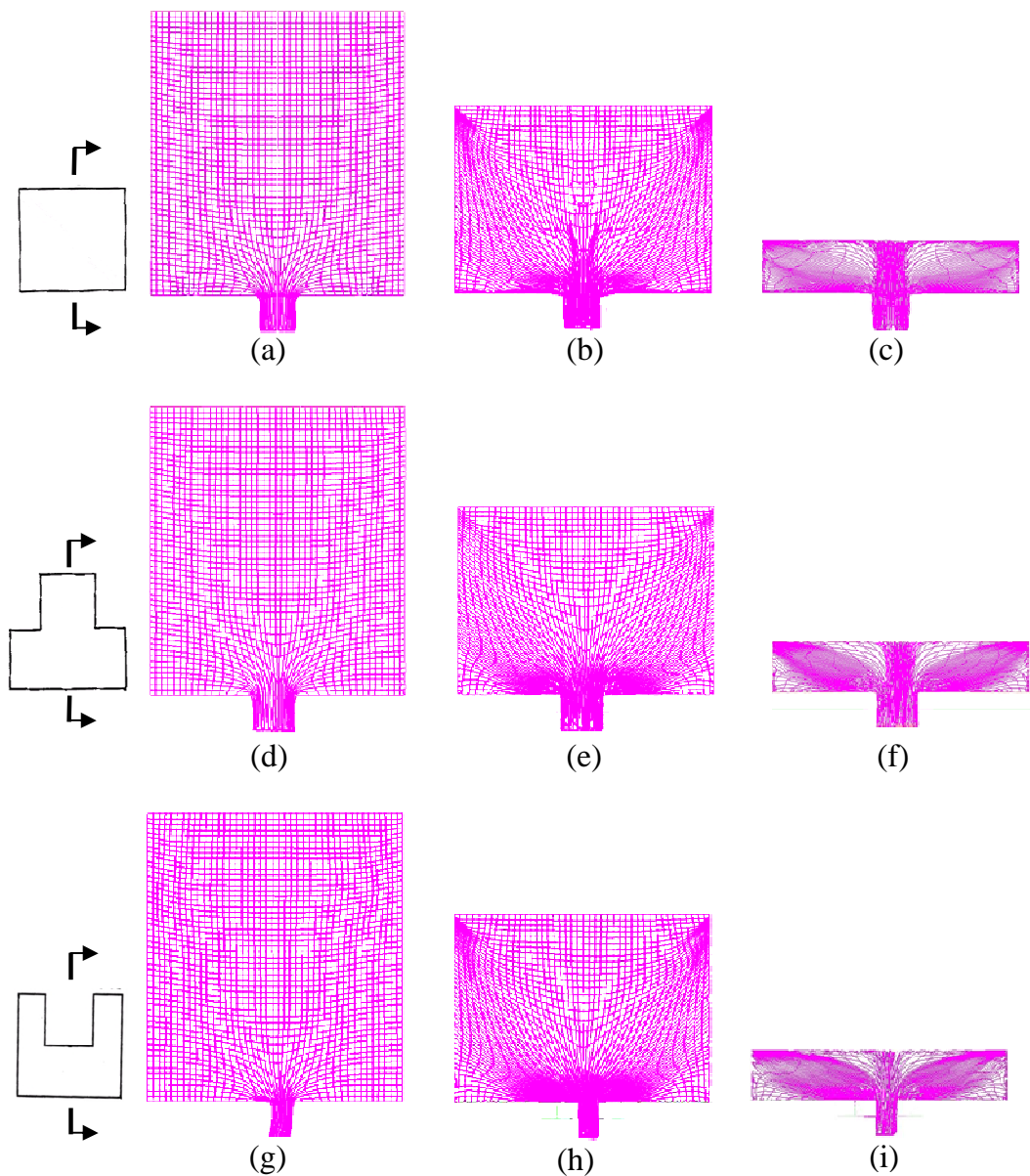


Figure 5.13 Metal flow in different section extrusions at different stages

It can be seen that basically metal flow patterns are similar for all three processes. At the ram displacement of 10mm deformation concentrates near the die entry, and most of the billet appears to remain undeformed. At the middle stage of a ram displacement of 40mm, an inverse conic deformed area formed in the billet and the dead metal zone developed at the bottom corner formed by the container and the die face. At the end of the extrusion, the dead metal stayed unchanged while

the heavily sheared bands can be seen and materials moving along the lower one are considered to form the billet surface. Another notable feature of this stage is: the ‘coring effect’ that means the material near the centre of the back end of the billet flows into the extrudate.

Difference can also be observed from Figure 5.13 that in the square extrusion, the grids are totally symmetric throughout the extrusion while in the other two extrusions the deformations are heavier at the left side than in the right side that can be attributed to the fact that the right side is at the wider side of the cross-sections of the extrudates so that the material at this side is easier to be extruded into the die orifice. The asymmetry of the deformation makes it difficult to produce a straight product.

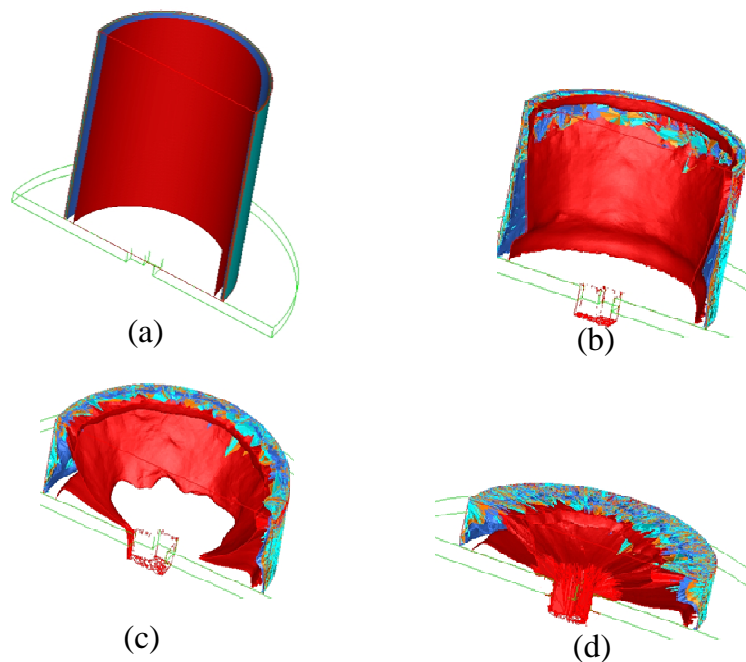


Figure 5.14 Metal flow near and at the billet surface for T-section

To view the metal flow more intuitively four cylindrical surfaces concentric with the billet outer surface were placed into the billet, which are shown in Figure 5.14(a) and whose positions are 0mm, 0.5mm, 1.5mm and 4.5mm from the billet

outer surface respectively.

Because of the highly similarity of the metal flow pattern of the three extrusions, only T-section is selected to be investigated. Figure 5.14(b), (c) and (d) are the deformed shapes of the four designed surfaces at the ram displacements of 40mm, 65mm and 80mm respectively. Throughout the process it can be seen that the subcutaneous layer and the surface material will stay in the discard. If proper discard length is chosen such that the back-end effect cannot bring them into the extrudate. Notably, the surface of the billet will stick on the inner container wall because of high friction on the interface between the billet and the container wall. Although the upper part of these materials represented by the cylindrical surfaces 0mm, 0.5mm and 1.5mm from the billet surface can move to the centre of the billet along the ram surface, they finally resided in the discard

5.5 Microstructure prediction

Note that in Subramaniyan's experiments (1989), specimens for mechanical testing, for heat treatment and for optical and electron microscopy were cut from a position one third of the total length from the extrudate head in order to ensure steady state conditions. Therefore the simulated microstructure results will be taken from a corresponding point that is just below the die entry when the ram travel is about 27mm because the billet length is 95mm and a 15mm thick discard was left in the container.

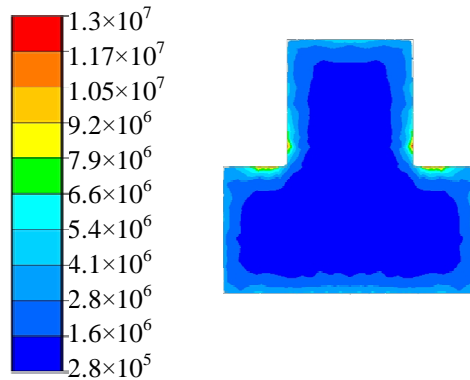
In the extrusion of AA2024, due to stored deformation energy within the extrudate, static recrystallisation usually occurs and extends to 100% of the material in some cases. The production of coarse grain during heat treatment is not beneficial because it causes a reduction in mechanical properties. Damage tolerance, fatigue crack propagation or corrosion resistance are three very important technical indices required by the aerospace industry. They significantly affected by the

recrystallised grain size and the volume fraction recrystallised. It has also been shown that this problem becomes greater as the complexity of section shape increases. Hence, knowledge of the variation of the recrystallised grain size with time and space assists optimisation of the extrusion process. In the following study, discussions are focussed on the simulated results using the microstructure evolution models described in section 5.2.

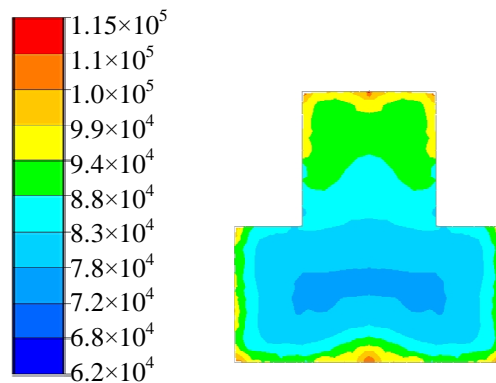
5.5.1 Grain boundary area per unit volume S_V and the density of recrystallisation nuclei N_V

To finally predict the volume fraction recrystallised, it is essential to calculate the grain boundary area per unit volume. As discussed in section 5.2.5, for complex shape extrusion like T-shape extrusion, the tetrakaidecahedron model with better space filling feature described as in equation (5.23) should be used. However because of the simple form of the equation (5.12) researchers tend to apply it erroneously to complex deformation taking the ε in it as effective strain for granted. In fact using the cubic grain model, the ε in the equation (5.12) equals to the effective strain only when the deformation is axisymmetric process (see Appendices C and D).

Figure 5.15 compares the results from these two methods, which shows that the cubic model appears to overestimates S_V . It displays that in the corresponding areas on the cross-section values from the cube model is two orders of magnitude higher than those from the tetrakaidecahedron model. Therefore to make a more accurate calculation, it is worthwhile to overcome the difficulties of incorporating the equation (5.23) into FEM.



(a) Result using plane strain cubic model



(b) Result using tetrakaidecahedron model

Figure 5.15 Comparison of the calculation of S_V using and (a) simplified plane strain cubic model and (b) tetrakaidecahedron model

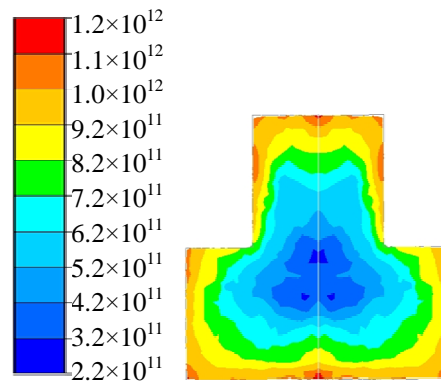


Figure 5.16 Density of recrystallisation nuclei

From Figure 5.15(b), the result shows that bigger values around the cross-section outer contour means there would have a higher density of recrystallisation nuclei,

which is supported by the simulated result in Figure 5.16, hence, higher possibility of being recrystallised.

5.5.2 The prediction of dislocation density ρ and subgrain size δ and misorientation θ

One way to calculate subgrain is to use the integral form of the equation (5.46) represented below

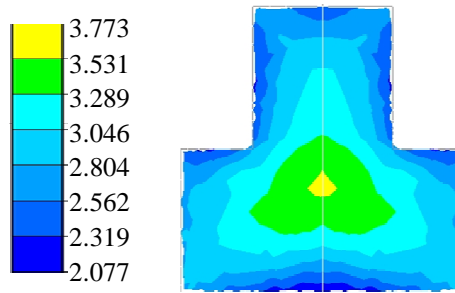
$$\delta = \int_0^\varepsilon \left(\frac{\delta}{\varepsilon_\delta \delta_{ss}} \right) (\delta_{ss} - \delta) d\varepsilon \quad (5.47)$$

in which ε_δ may be related to the Zener parameter and assumed to be proportional to $Z^{\frac{3}{4}}$ (Sellars and Zhu 2000) as follows:

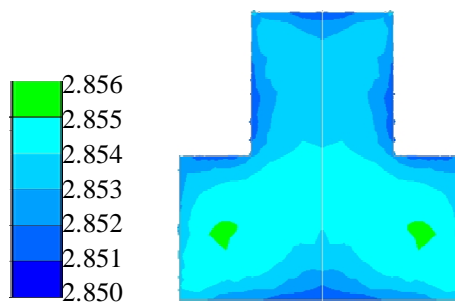
$$\varepsilon_\delta = AZ^{\frac{3}{4}} \quad (5.48)$$

and the δ_{ss} can be either decided by the equation (2.19) in which for AA2024 alloy $m=-1$, $A=-0.5778$ and $B=0.0378$ (Subramaniyan 1989, p.145) or be simply assigned a constant since experiment shows the spread of subgrain size is very small (Subramaniyan 1989, p.146). When using the equation (5.47) another problem is how to decide the initial subgrain size; an assumption has to be taken because the dislocations have not relaxed to form subgrains at this stage. An assumption of initial subgrain size of $40 \mu m$, which is about half of the initial grain size seems reasonable.

Figure 5.17(a) shows a predicted result for subgrain size distribution when the equation (2.19) was used to calculate the δ_{ss} in the equation (5.47) while Figure 5.17(b) displays when δ_{ss} was assumed to be a constant of 2.85 which is close to Subramaniyan's experimental results (1989, p.158).



(a) Using the equation (2.19) to calculate δ_{ss}



(b) Taking the δ_{ss} as a constant

Figure 5.17 Subgrain size distribution (μm)

It can be seen the both maps in the Figure 5.17 show similar subgrain distributions, in which subgrains in the centre are bigger than those near the edges and the predicted subgrain size is reasonably close to the experimental result. However it should be pointed out that in simulation for the case of using the equation (2.19) to calculate δ_{ss} , a steady state of the subgrain size can never be achieved, it reduces all the time during simulated extrusion process to unrealistic values, even to be negative, which are physically unrealistic. The subgrain size keeps nearly the same when its steady-state size δ_{ss} is regarded as a constant, which is closer to the real situation. In view of the only difference between two ways of the application of the equation (5.47) into FEM, this may be caused by the very small strain-rate value in the centre of the billet cross-section (see Figure 5.10) because anomaly will happen when a logarithm operation is done to a very small value or a negative value.

The misorientation result predicted using the equation (5.45) is shown in Figure 5.18. According to Zhu and Sellars (2000) the characteristic strain ε_θ is related with the Zener parameter by

$$\varepsilon_\theta = BZ^{0.25} \quad (5.49)$$

where B is a constant. The initial misorientation is obviously zero. Although so far there are no methods found in the literature to calculate the θ_{ss} , the steady-state average misorientation may be assumed to be constant for lack of evidence to the contrary (Shercliff and Lovatt 1999). A value of 3 degrees for θ_{ss} was used in this study.

Figure 5.18 shows that areas around the profile have higher misorientations, which is consistent with the fact in those areas higher energy is accumulated, hence, higher misorientations are needed to accommodate it.

However the most arguable question is that in the applications of these equations, either the empirical equation (for the equation (5.47)) or a constant value (for the equation (5.45)) has to be used to calculate the state variable at steady state. The predetermination of the subgrain size and the misorientation makes the calculations from the equation (5.45) and (5.47) superfluous. Actually the starting point to develop these equations is to deal with the microstructure evolution in the transient conditions with small strain range (from 0 to 1). It would not be worthwhile to use them to analyse a problem such as extrusion during which the strain is a lot higher and most of the time it is in the steady-state.

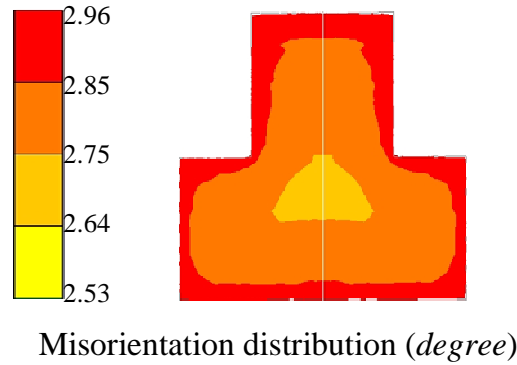


Figure 5.18 Misorientation results using differential equations

Figure 5.19(a) is the predicted subgrain size distribution using the empirical equation (2.19), Figure 5.19(b) is the dislocation density distribution result using the both physically and theoretically proved Holt relation (Holt 1970). This is described by the equation (2.17). For convenience, equation (2.19) and equation (2.17) are represented below.

$$\rho_i^{\frac{1}{2}} \delta = Constant \quad (5.50)$$

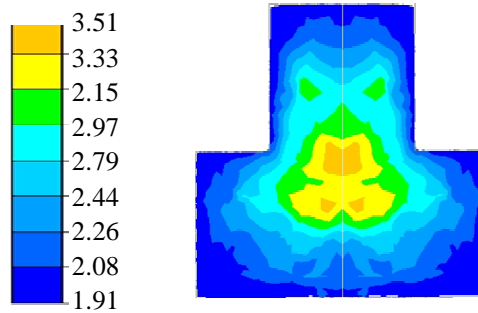
$$\delta_{ss}^m = A + B \ln Z \quad (5.51)$$

In this study the constant used is 50 for the equation (5.50).

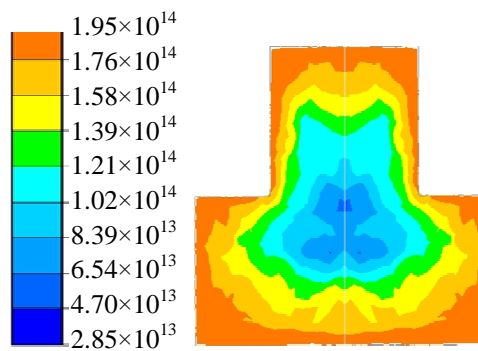
The predicted result is shown in the Figure 5.19(a). The distribution has a similar gradient with those in Figure 5.17 and the results are comparable with the experiment (Subramanian 1989, p.158). Figure 5.19(b) naturally displays a map with an inverse gradient because the inversely proportional relation between the subgrain size and the square root of the dislocation density. Experimental measurements for dislocation density are scarce, but the calculated values are reasonable for a hot aluminium extrusion process.

The map in Figure 5.19(a) means the subgrain size, in general, increases with

decreasing Zener parameter, which is associated with the phenomenon of a decreasing strain rate and increasing temperature shown in Figure 5.10(b) and Figure 5.11(b) respectively. This may be explained by remembering that at lower strain rates there is an increase in the time available for dislocation rearrangement and at higher temperature, increased thermal activation appreciably increases dislocation mobility, thus resulting in larger subgrain sizes and lower internal dislocation density.



(a) Subgrain size distribution (μm)



(b) Dislocation density distribution (m^{-2})

Figure 5.19 Dislocation density and subgrain size using Holt relation

5.5.3 The prediction of stored energy

The equation (5.32) represented as the equation (5.52) was used to calculate the stored energy per unit volume.

$$P_D \approx U_i + U_{sb} = \frac{Gb^2}{10} \left(\rho_i \left(1 - \ln 10 b \rho_i^{\frac{1}{2}} \right) + \frac{2\theta}{b\delta} \left(1 - \ln \left(\frac{\theta}{\theta_c} \right) \right) \right) \quad (5.52)$$

in which misorientation θ and the critical misorientation θ_c are assumed to be 3 and 15 degrees, respectively.

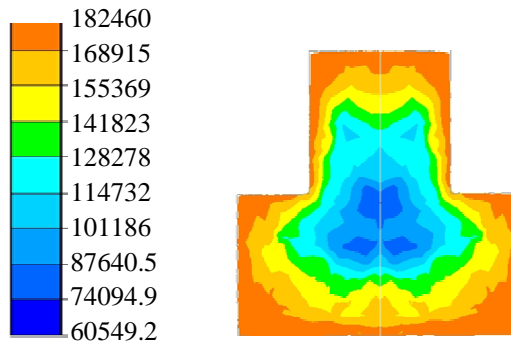


Figure 5.20 The stored energy, P_D , distribution (N/m^2)

Theoretically, the highest volume fraction recrystallised appears near the billet surface area because more stored energy for recrystallisation is accumulated due to higher temperature, strain, strain rate and dislocation density. It can be seen from Figure 5.20 the predicted highest values of the stored energy are near the billet surface that is around the edge of the cross-section. It decreases from the edges to the centre.

5.5.4 The volume fraction recrystallised

$$X_V = 1 - \exp\left\{-0.693\left(\frac{t}{t_{50}}\right)^n\right\} \quad (5.53)$$

Equation (5.3) that is represented here as equation (5.53) for convenience is widely accepted to be used to calculate the volume fraction recrystallised, and in which n is commonly reported as a value of 3. However to the calculation for the parameter t_{50} could be different. The related equations (5.4), (5.5) and (5.6) are relisted below

$$t_{50} = \frac{C_t}{M_{GB}P_D} \left(\frac{1}{N_V}\right)^n \quad (5.54)$$

$$M_{GB} = M_0 \exp\left(\frac{-Q_{GB}}{RT}\right) \quad (5.55)$$

$$M_{GB} = \frac{M_0}{T} \exp\left(\frac{-Q_{GB}}{RT}\right) \quad (5.56)$$

Therefore there are three methods that can be used to calculate t_{50} : one is to regard C_t/M_{GB} as a constant, the other two is to use either the equation (5.55) or (5.56) to calculate M_{GB} , then t_{50} .

Predicted volume fractions recrystallised, X_V , for all three sections are shown in Figure 5.21. Among it the first row of the Figure 5.21, Figure 5.21 (a), (d) and (g), are the simulated results when assuming C_t/M_{GB} is a constant; the second row, Figure 5.21 (b), (e) and (h), are the simulated results when using the equation (5.55) to calculate M_{GB} while the third row Figure 5.21 (c), (f) and (i) when using the equation (5.56). The comparison between the predicted average X_V and the experimental measurements (Subramaniyan 1989) is listed in Table 5.6.

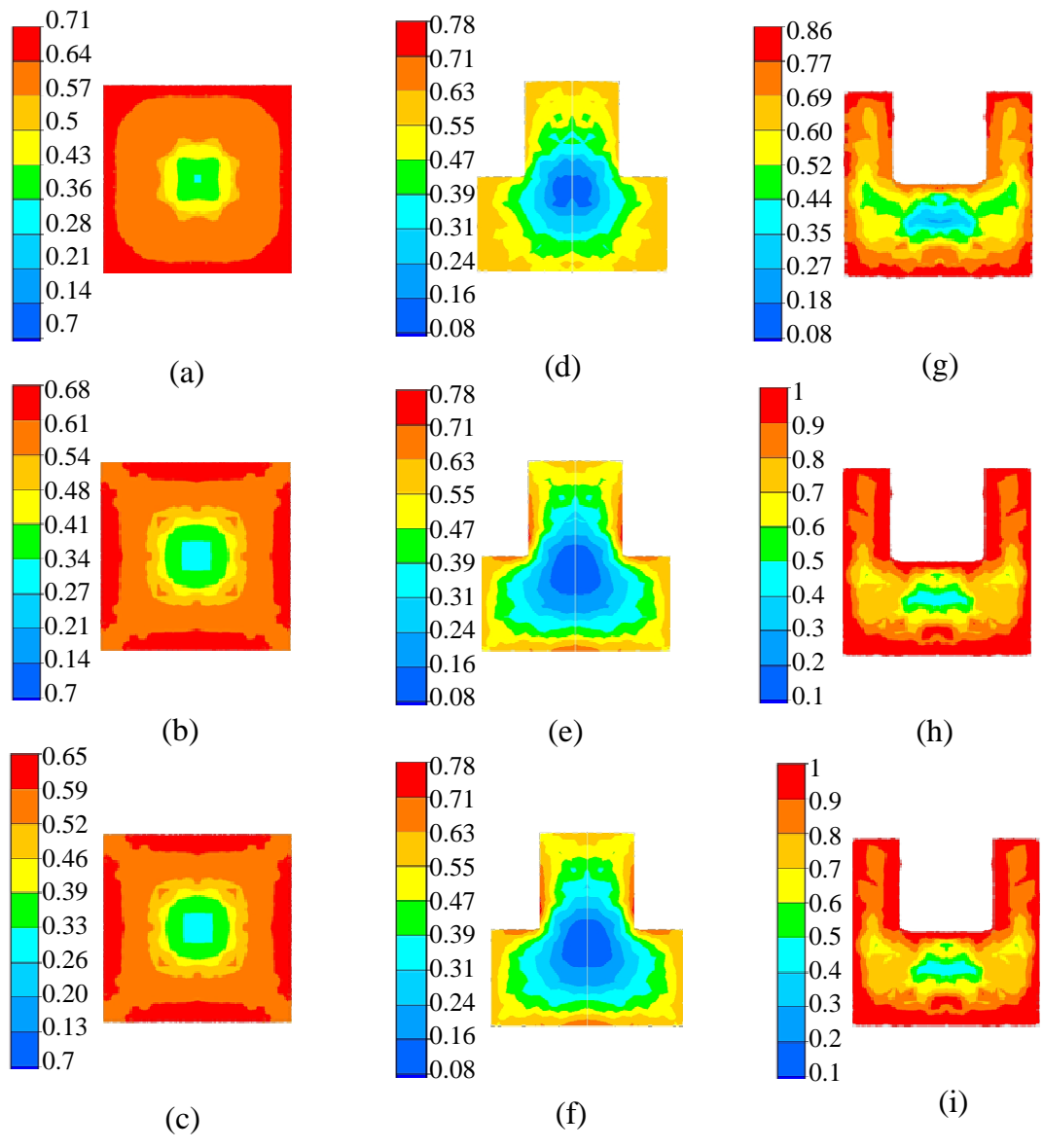


Figure 5.21 Predicted volume fraction recrystallised, X_V

It can be seen from the Figure 5.21 and the Table 5.6, the results from the first row where C_t/M_{GB} is a constant are least accurate ones, which can be attributed to the fact that it is not appropriate to simplified C_t/M_{GB} as a constant because M_{GB} is a variable. However when considering using either the equation (5.55) or (5.56) to calculate t_{50} , C_t may be treated as 1, which means its influence can be integrated into the constant, M_0 . It is interesting to see that maps in the second row don't have significant differences with their corresponding ones in the third row, which suggests that it is actually unnecessary to use an explicit temperature-dependent to calculate the grain boundary mobility, M_{GB} , in other words, the temperature's influence on the grain boundary mobility is well represented by the temperature in the exponential term in the equation (5.55). It can also be noticed that the predicted X_V for T-section and U-section in Figure 5.21 (e) (h) agree better with the experimental measures than does that for Square-section in Figure 5.21 (b), the possible reason is that U-section and T-section have a similar degree of shape complexity. However it is sensible that it needs to adjust the value of M_0 , the most influential parameter to t_{50} , hence to X_V , to get better simulated X_V value for the square section. This implies that the grain boundary mobility could be a shape-related constant.

	Square	T-section	U-section
Predicted X_V (%)	~63.5	~68	~100
Experimental X_V (%)	~54.66	~74.89	~98.22
Difference (%)	+16	-9	+1.81

Table 5.6 Predicted X_V vs. experimental measurements

Another notable feature in all the maps in the Figure 5.21 is that the X_V values increase from the centre to the outside edges and increase markedly near the corners, which clearly shows that the extent of recrystallisation varied along the periphery of shaped extrusions in the non-circular sections. This phenomenon can be confirmed by experimental micrograph in Figure 5.22. It can be attributed to the higher stored energy (see Figure 5.20) arising from severer deformation, higher

temperature near these corners (see Figure 5.9 and Figure 5.11).

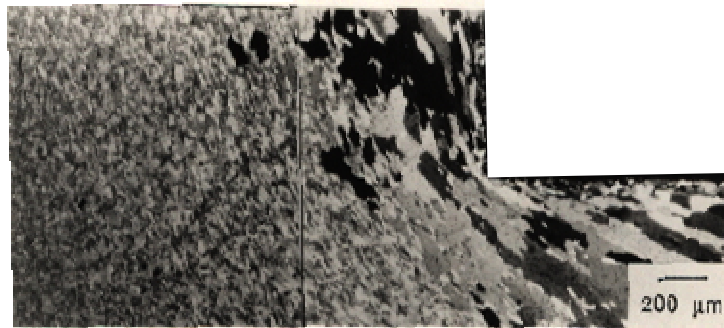


Figure 5.22 Microstructures in the transverse plane of a solution soaked T-section extrudate (Subramaniyan 1989, p.131)

5.5.5 The predicted recrystallised grain size

The typical heat treatment to alloy 2024 is a solution treatment at 500°C for 1 hour in an air circulating furnace, followed by quenching to room temperature and subsequent age hardening in an air circulation oven. Thus during the extrusion and soak cycle of AA2024 the stored deformation energy within the extrudate ensures that some static recrystallisation usually occurs after the extrusion and soaking process. As mentioned before the production of coarse grains is detrimental to the damage tolerance, fatigue crack propagation or corrosion resistance. Therefore, prediction and control of the grain size is of importance.

FEM predicted results of the recrystallised grain size, d_{rex} , are shown in Figure 5.23. They are the sizes right after the solution treatment and the water quenching. It indicates that d_{rex} decreases from the centre to the surface over the extrudate cross-section. This agrees with the experimental observations (Subramaniyan 1989; Vierod 1983). The recrystallised grain of an extrudate extruded from a billet with initial temperature of 350°C, after solutionising and quenched by water, is shown

in Figure 5.24 The predicted d_{rex} at the centre is 364 μm and for the measurement at the surface, the d_{rex} is 244 μm , which fit reasonably well with experimental measurements 400 μm at the centre and 250 μm (Subramaniyan 1989, p.166) at the surface. This grain size distribution is due to a larger number of nucleation sites for static recrystallisation resulting from the heavily strained periphery.

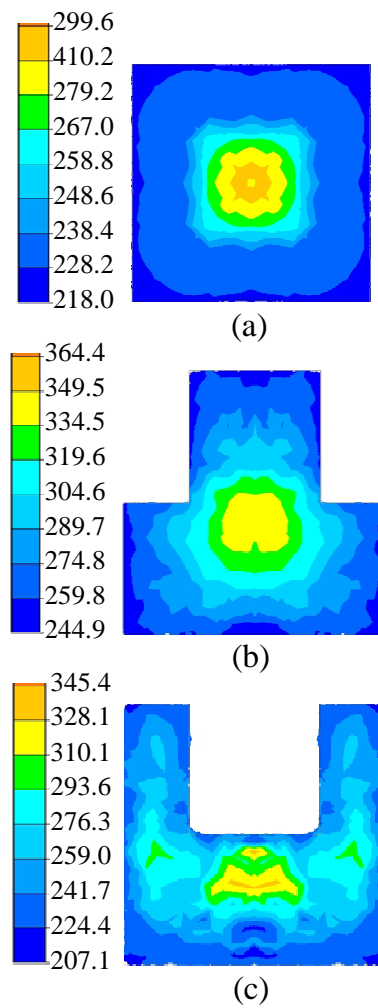


Figure 5.23 Predicted recrystallised grain size (μm)

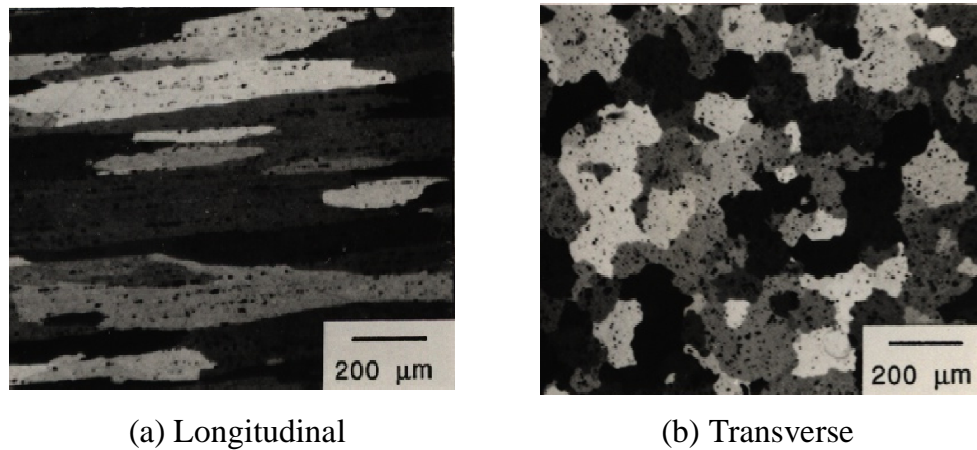


Figure 5.24 Recrystallised grain of the extrudate after 500°C solutionising followed by water quench (Subramaniyan 1989, p.162)

It is also interesting to find that the similarity of the gradient map between the grain and the subgrain (in Figure 5.17) for the T-section. It has been reported by Zaidi and Sheppard (1983) that the recrystallised grain size can be directly related to the hot worked subgrain size. This correlation indicates that the recrystallisation occurs primarily by subgrain coalescence.

5.6 Concluding remarks

Based on the discussion of this chapter, following conclusions are suggested:

1. Forge2009[®] is a powerful FEM software that can accurately predict the load variation, temperature change and metal flow for complex section extrusion. Predicted results show that the extruded load increase with the complexity of the section, represented by the peripheral ratio; higher temperature appears at the corners of the section because of higher degree of deformation; because of high friction between the container and the billet, the outer surface of the billet doesn't have to be machined; because of the 'coring effect', the back end of the billet must be clean.
2. The exponential term in the equation (5.5) is sufficient to represent the

influence of temperature on the grain boundary mobility. It is not necessary to use an explicit temperature-dependent prefactor when calculating the grain boundary mobility.

3. The tetrakaidecahedron grain model that has better space-filling features and approximates closely to the grain shape observed metallographically. It was first integrated into the FEM simulation for complex section extrusion. Simulated results show that the simply cube grain model overestimated the grain boundary surface area per unit volume.
4. The micro-band based model to calculate the probably cannot be applied to extrusion simulation because during extrusion micro-bands are not encouraged. The model to calculate the geometrically necessary dislocation density needs further investigation.
5. The user-subroutine interface makes Forge2009[®] an open, flexible and versatile simulation system. With the aid of the Fortran[®] sub-routine, the user can integrate a variety of constitutive models, boundary conditions models and structure models into Forge2009[®]. Special functions to enhance the simulation such as auto-trim technique can also be realised through the subroutine interface.
6. With proper models microstructure parameters can also be successfully predicted during extrusion using Forge2009[®], these models can be either physically-based or empirical. Although physically-based model are preferred empirical methods have to be resorted to on occasions where physically-based model cannot be established perfectly.
7. The predicted volume fraction recrystallised X_V and recrystallised grain size d_{rex} agree well the experimental measurements. The higher X_V happens around the corner areas and X_V appears to increase with the complexity of the section. The predicted recrystallised grain size distribution shows grains in the central area of the section are bigger than those in the periphery.

methods, combining both grid and surface tools, were used to define in detail the flow of material. These showed clearly the inner and outer surface formation mechanisms of the tube extrusion. The seam weld, an important quality indicator, was also evaluated by selecting an appropriate criterion. A one-third self-contact model was developed in order to evaluate the suitability of a simpler one-sixth model for the modelling of microstructure evolution.

6.2 Experiment procedure

The experimental data used in this part are extracted from the literature (Nisaratanaporn 1995). The material used in the study is AA6063 whose major chemical compositions are listed in Table 6.1, which is a commonly preferred alloy to produce hollow extrudate because of its good plasticity.

Cu	Mn	Mg	Fe	Si	Zn	Ti	Ni	Pb	Al
0.003	0.0062	0.436	0.186	0.431	0.018	0.0054	0.001	0.001	Balance

Table 6.1 Chemical composition (wt%) of the AA6063 alloy (Sheppard *et al.* 1998)

The press used for this experiment is identical to the one shown in Figure 4.1. The ram speed in the experiment was 3mm/s. The dimensions of the billet are 73mm in diameter and 100mm in length. Its initial temperature is 450°C and the other tools' temperatures are 50°C below the billet's. The inner diameter and outer diameter of the extrudate are 8mm and 16mm respectively. The picture of the die and its schematic drawings are in Appendix E.

6.3 FEM simulation

6.3.1 The determination of the constants of the constitutive equation for AA6063 alloy

In this study, the flow stress data are from Akeret's work (1978) in which data are presented in the form of a series of graphs with true stress-true strain curves of

different temperatures at a certain strain rate. To keep the influence of the temperature rise during the test as least as possible, only the peak stresses were selected for the constitutive equation constants calculation. These stresses are presented in Table 6.2 corresponding their experimental temperatures and strain-rates.

Stress (Mpa) / Strain-rate(s ⁻¹) / Temperature (K)	Strain-rate(s ⁻¹)							
	0.05	0.1	0.2	0.5	1	2	5	10
623	44	47	50	54	57.5	61	67	72
673	28	32	35	39	43	46.7	53	58
723	21	24.5	27	30.5	34.5	37.5	44	49.5
773	16.7	19.17	21	25	28.5	31.5	37	42
823	12.5	14.17	16	19.17	21.5	24.5	27.5	31

Table 6.2 Flow stress at different temperature and different strain rate Akeret's experiment (1978)

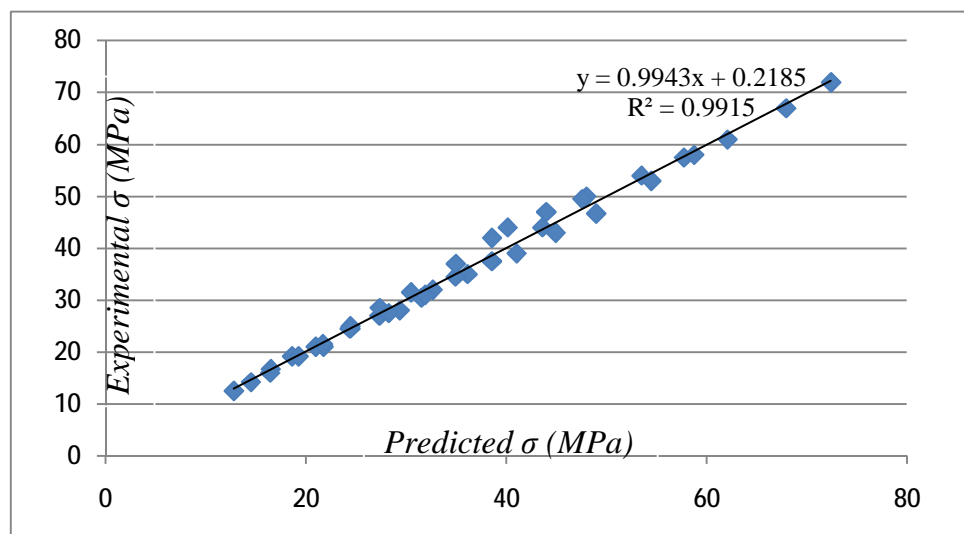


Figure 6.2 Comparison between predicted and experimental stress

The multi-regression method presented by Sheppard and Jackson (1997) was used to process the data in Table 6.2. $\alpha=0.0283 \text{ m}^2/\text{MN}$, $n = 5.267$, $\Delta H = 149.103 \text{ KJ/mol}$ and $A = 2.75 \times 10^{10} (\ln A = 24.04) \text{ s}^{-1}$ were obtained from the analysis (see Appendix F). Figure 6.2 shows using these constants an excellent agreement

between predicted stress and experimental stress was achieved and the equation (3.12) can well characterise the flow behaviour of AA6063 aluminium alloy at elevated temperature.

6.3.2 One-sixth FEM model

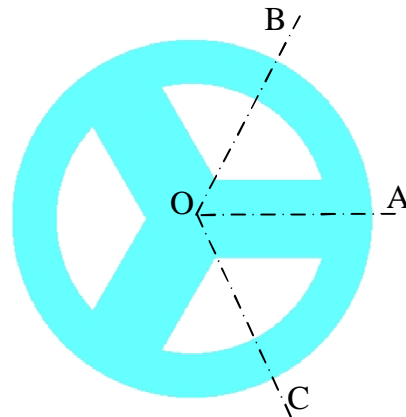


Figure 6.3 Top view of the bridge die

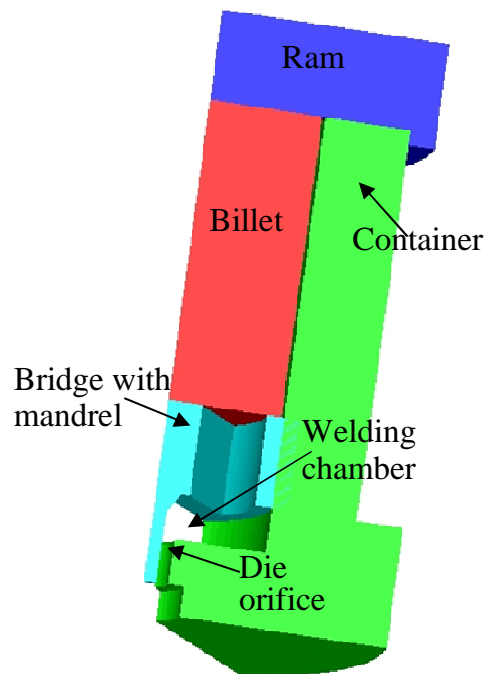


Figure 6.4 The one-sixth FEM model for tube simulation

As in previous simulations, the symmetry of the extrusion was utilised in tube simulation to reduce the calculation time. In the case of round tube extrusion the symmetry of the extrusion is solely determined by the symmetry of the bridge die. It can be seen from Figure 6.3 two symmetry planes can be placed along lines OA and OB so that in the simulation the tools and the billet as a whole can be represented by a one-sixth FEM model that only uses the elements that are enclosed by the two symmetry planes. The one-sixth FEM model is shown in Figure 6.4.

6.3.3 Load and temperature evolution prediction

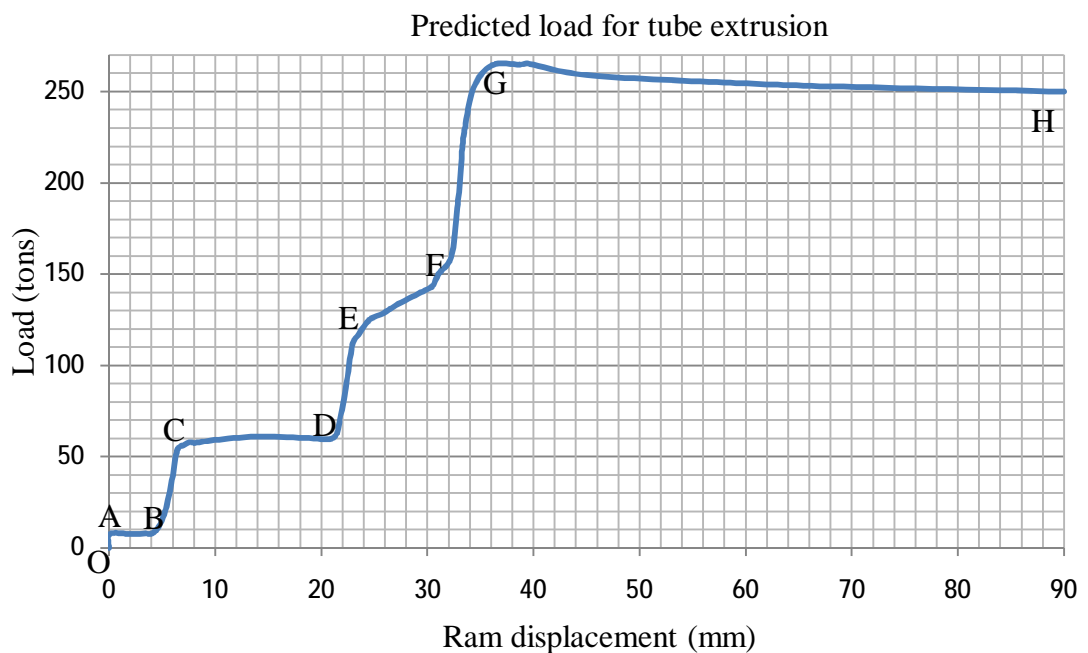


Figure 6.5 Load evolution with ram displacement of tube extrusion

The predicted load-displacement curve for tube extrusion is shown in Figure 6.5. Points A, B, C, D, E, F, G, H are key points on the curve, whose corresponding positions in the simulation are captured in Figure 6.6. The predicted peak load of

266 tons agrees perfectly with the experimental measurement of 261 tons (Nisaratanaporn 1995). Because of the complexity of the material flow in tube extrusion using bridge dies, its load-displacement curve is correspondingly complicated compared with those of solid section extrusions using conventional dies (see Figure 5.8). Nonetheless this process can be conveniently divided into several stages:

- (1) Segment OAB obviously represents the billet upsetting period during which the billet was upset until it totally contacted the container at point B;
- (2) Segment BCD is the billet-dividing stage in which from point B billet began to be split by the bridge die into three individual legs and the load needed increased rapidly until the breakthrough point C was reached. Then the legs continued to flow in their own portholes while the load kept nearly unchanged. At point D the legs reached the bottom of the welding chamber;
- (3) Segment DEF can be called welding-chamber filling stage although it probably is that the material could have flowed into the die orifice before the chamber is completely filled. It is interesting to note that during segment DE, the load increased much faster (steeper slope) than it did during the segment EF, which is because DE largely is a period in which part of the leg in the welding chamber is upsetting such that a higher increasing rate of load is needed; while during EF, this part of material gained enough momentum to flow inside the chamber circumferentially, the increasing rate of load necessary to push the material to move thus becomes smaller;
- (4) From point F, welded material started entering the die orifice, a tubular extrudate formed and the welding chamber was fully filled, finally the peak load for the tube extrusion was reached at point G. The load subsequently reduced to a steady state until the end of the extrusion at point H.

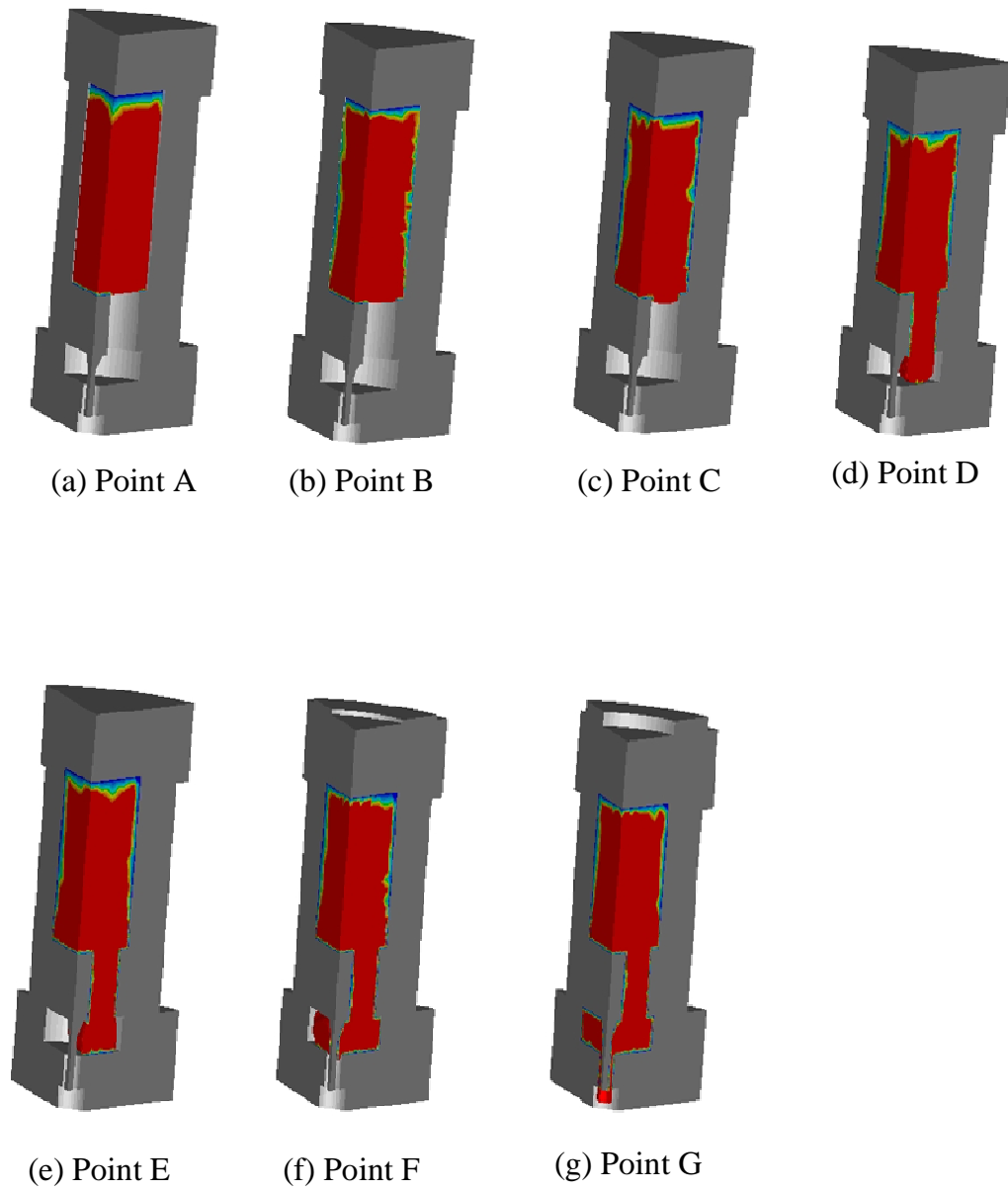


Figure 6.6 Deformed billet at different key points

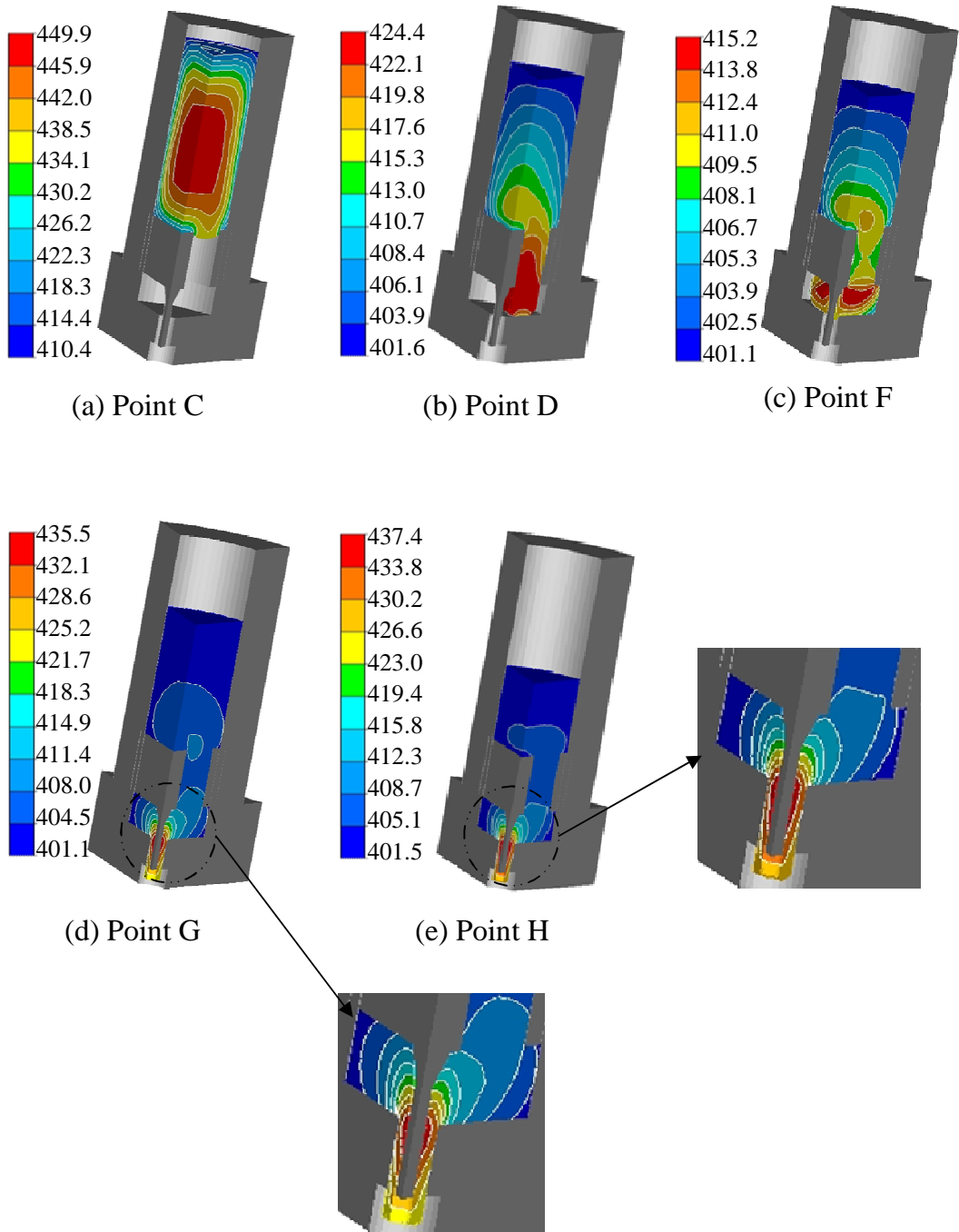


Figure 6.7 Temperature evolution during tube extrusion (°C)

Figure 6.7 reflects the billet temperature evolution during the tube extrusion. Figure 6.7(a), (b), (c), (d) and (e) correspond to the ram displacements of points C, D, F, G and H in the Figure 6.5. It can be seen from Figure 6.7(a) that because the heat loss between the billet and container, bridge die and the ram, only the centre of the billet can hold the initial temperature, the temperature of the contacted surface of the billet has decreased substantially. The lowest temperature 410.4°C appears at the end of the billet that transferred the heat to the cooler ram. In Figure 6.7(b) and Figure 6.7(c) the overall temperature of the billet continued to decrease. The lowest temperature dropped to 401°C and the highest temperature moved to material flow front. However, because the billet was divided by the bridge die into three legs there was a larger contact area between the material and the bridge die and welding chamber, both of which had an initial temperature 400°C, the highest temperature decreased to 415°C. At point G the temperature shown in Figure 6.7(d) with the metal flowing into the die orifice and through the die land, more mechanical work was converted into heat and the highest temperature rose to 435.5 °C whilst the lowest stayed at 401.1 °C. After the point G until the end of the extrusion, point H, the extrusion process was well under a steady state, the highest and lowest temperatures and temperature distribution remained almost constant.

Unlike in the solid-section extrusions discussed previously, the extrudate's exit temperature in tube extrusion is lower than the initial billet temperature. This could be partly because the split metal by the bridge die enhances the heat transfer from the billet to the bridge die. Another more important factor is that for this particular alloy (AA6063), the non-steady-state characteristics of the process may not be strong, as strain hardening at elevated temperatures is relatively weak and dynamic recovery leads to relatively stable flow stresses in most part of an extrusion cycle. In association with these, thermal effect is not pronounced and the process may be approximated as an isothermal one (Li *et al.* 2008). The low ram speed used in the simulation is also likely to be a reason for this phenomenon.

The other difference from the solid extrusion about the temperature distribution is that in the die land over the extrudate's cross-section the higher temperature is at the inner side of the tube, which can be explained by two facts: first in Figure 6.7(c) the material with the highest temperature flowed to the mandrel surface, which can be seen in the investigation of the metal flow in the following section; second and probably the major reason is that heat resulting from the severe deformation that happened near the mandrel surface shown in Figure 6.8.

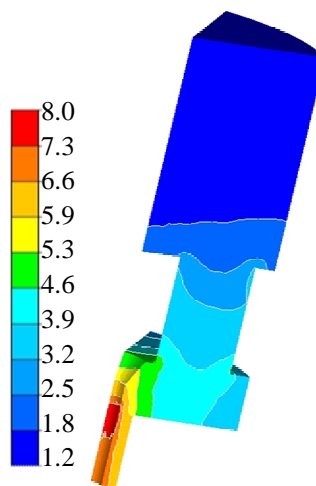


Figure 6.8 Strain distribution of tube extrusion

6.3.4 Metal flow and surface formation

Because the bridge die greatly influences the metal flow, material movement during bridge die extrusion is much more complex. Forge2009[®] can help researcher to understand the metal flow mechanism of complicated forming process using the virtual gridded planes. Five gridded planes numbered from (1) to (5) were used to study the metal flow, which are circumferentially distributed every 15° through the centre axis of the billet. They are shown in Figure 6.9(a) and Figure 6.9(b) is their initial shape before deformation. Among them, planes (1) and (5) sit on the symmetry planes of the one-sixth FE model. Figure 6.10 displays the metal flows on the two symmetry planes. Figure 6.10 (a), (b) and (c) are the

deformed shapes of the plane (5) at the ram displacements of 10mm, 40mm and 80mm respectively. Figure 6.10 (d), (e) and (f) are deformed shapes of plane (1) at the same ram displacements.

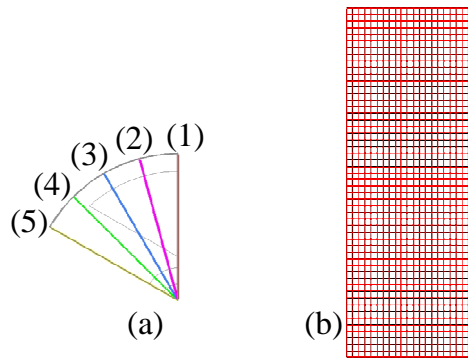


Figure 6.9 Gridded planes and their positions in the billet

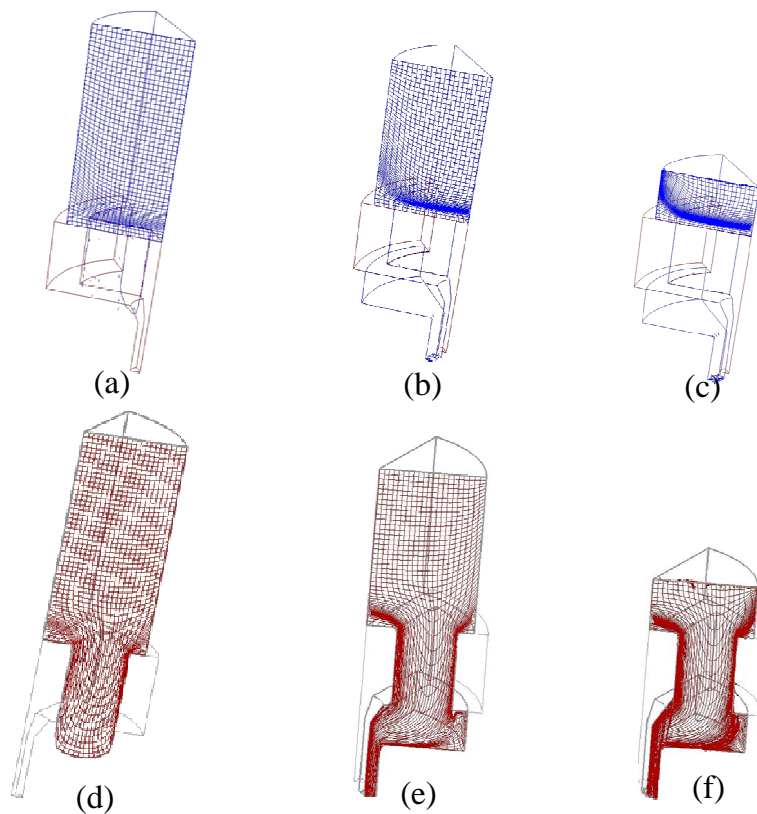


Figure 6.10 Metal flow on the symmetry planes in tube extrusion

Because planes (1) and (5) are on the symmetry planes of the deformation of the

billet they can keep straight during the process. Furthermore, for grid plane (5), the deformation concentrated within a belt whose vertical segment is close to the container wall and whose horizontal segment is several millimetres above the top of the bridge. Connecting this horizontal and vertical severe deformation segments is the curve segment above a dead metal zone at the corner formed by the bridge top and the container wall.

Plane (1) is a much-studied plane, Sheppard *et al* (1998) has used Forge2[®], an early version of Forge2009[®], to get an approximate description of it. Later Flitta and Sheppard (2002) achieved more realistic result of the metal flow on this plane using Forge3[®], another early version of Forge2009[®]. In this study a finer grid plane in a 3D model was employed to represent the material movement. It can be seen from Figure 6.10(e) at the ram travel of 40mm, the DMZ between the bridge top and the container has well formed. In the welding chamber the DMZ was also established. It can be also noted that the right part of the flow front will first moved toward the welding chamber wall, later moved upward until it contacted the bridge bottom, and finally filled the corner area of between the bridge bottom and the container. In the subsequent stage of extrusion, material that contacted with this flow front in the weld chamber could generate a certain amount of material fold. However this fold will not influence the extrudate because it will stay in the welding chamber as a DMZ which can be seen from Figure 6.10 (f). Figure 6.10 (f) also indicates clearly that at the end of the extrusion the material next to the billet surface flowed to the extruded tube's outer surface and the inner wall of the tube extrudate was formed by the material in the centre of the billet. It explains the fact that unlike the solid section extrusions the inner side of the tube has a little higher temperature because the inner tube wall was formed by the material initially at the centre of the billet with a higher temperature (see Figure 6.7).

Figure 6.11 is a comparison of the predicted metal flow pattern on the grid plane

(1) with its corresponding experimental macrograph in the welding chamber. They agree quite well with each other, which clearly show the metal at the outer surfaces of the tube originated from the virgin metal in the surface generation zones (locations a and a') and the metal forming the inner surfaces, came from the metal in the surface generation zones adjacent to the mandrel (locations b and b').

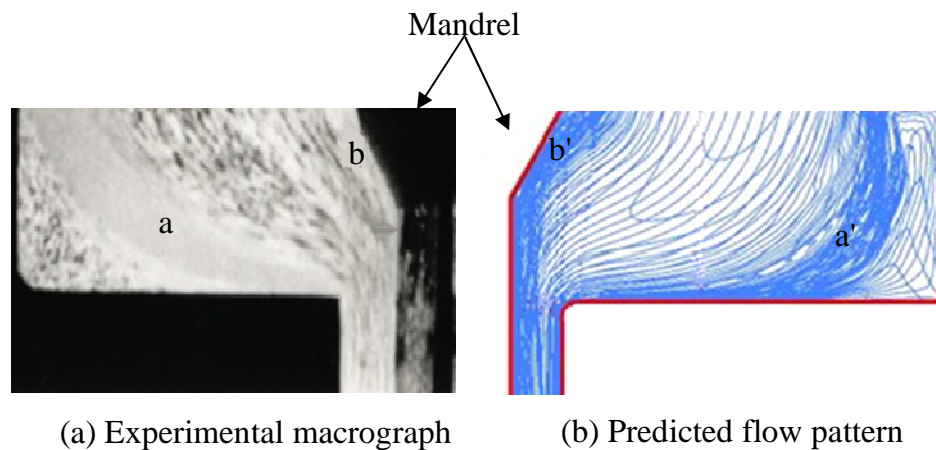


Figure 6.11 Comparison between (a) experimental result (Nisaratanaporn 1995, p.101) and (b) predicted metal flow in the welding chamber

Figure 6.12 shows the deformation of the other three grid planes, in which Figure 6.12 (a) and (b) are the shapes of the grid plane (2) at the ram travel of 40mm and 80mm respectively; Figure 6.12 (c) and (d) are those for the grid plane (3) and Figure 6.12 (e) and (f) for the grid plane (4) at the corresponding ram displacements. These figures indicate that for grid planes (2), (3) and (4) it still holds true that the material at the centre of the billet forms the tube's inner wall. However, it can be seen from Figure 6.12 (b) that at the end of the extrusion part of the outer material close to the billet surface on the plane (2) flowed into the tube's outer surface. But the materials on the other two planes did not contribute on the tube's outer wall formation. This implies that the material that forms the tube's outer surface mainly is from between the plane (1) and the plane (2) on the outer part of the billet. The DMZs are same as those indicated in the grid plane (1)

shown in Figure 6.10 except that in the porthole and the welding chamber the planes cannot keep straight anymore because of the influence of the bridge. In the welding chamber they obviously lurch to the welding plane. For both planes (2) and (3) their flow fronts can still reach the bottom of the welding chamber while for the plane (4) the Figure 6.10 (e) and (f) indicate that the material on this plane is much closer to the bridge surfaces so that during the extrusion it will not contact the bottom of the welding chamber and material between this plane and the symmetry plane (5) will mainly proceed to the inner side of the tube. This suggests that only small part of its material near the billet centre forms the inner wall of the tube extrudate and most of this plane will stay in the DMZ in the welding chamber which will be displayed in Figure 6.15.

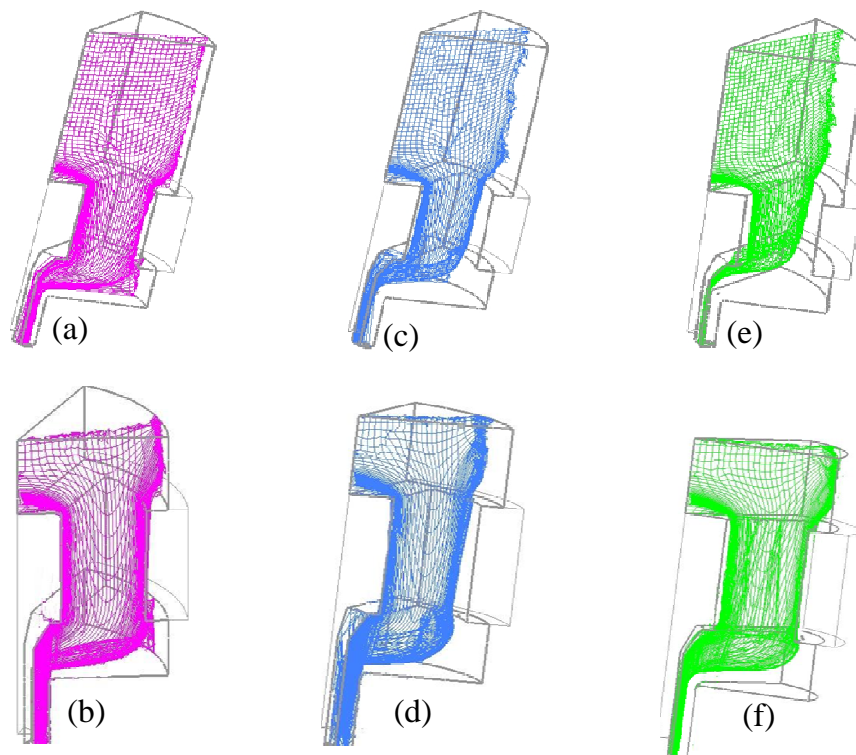


Figure 6.12 Flow patterns that are not on the symmetry planes in tube extrusion

In Figure 6.13 ten cylindrical surfaces that are coaxial with the billet were devised to observe the metal flow represented by their topological changes during

extrusion. They are numbered as surface 1 to 10 from the outside to the centre. Their distances from the billet surface are shown in Table 6.3.

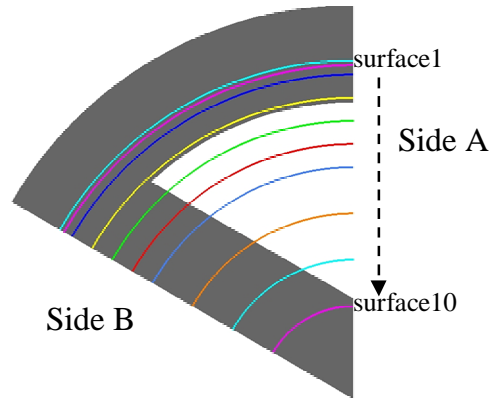


Figure 6.13 Positions of ten cylindrical surfaces inside the billet

Surface No.	1	2	3	4	5	6	7	8	9	10
Distance from the billet surface (mm)	0	0.5	1.5	4	6.5	9	11.5	16.5	21.5	26.5

Table 6.3 Distances from the billet surface of the 10 cylindrical surfaces

Figure 6.14(a) shows the metal flow of the cylindrical surfaces coaxial with the billet surface from side A marked in Figure 6.13 at the ram displacement of 40mm; Figure 6.14(b) is observed from the side B shown in Figure 6.13 at the same ram travel.

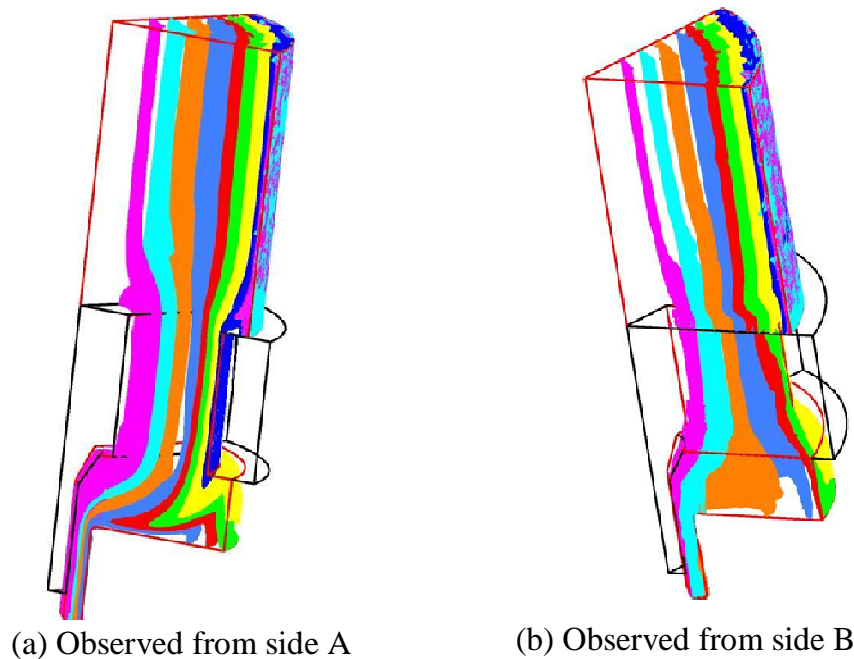


Figure 6.14 Metal flow of surfaces coaxial with the billet surface

It can be seen from Figure 6.14 as a direct extrusion the surface material of the billet will stick onto the container wall. At a ram travel of 40mm, the dark blue surface 3, which is very close to the billet surface, if observed from side B, had shown little flow whilst the surface observed from side A was flowing along the outer wall of the porthole. All other surfaces seen from side A have already reached the bottom of the welding chamber. For surfaces numbered from 4 (yellow) to 7 (blue) their flow fronts, after touching the welding chamber bottom, moved outward and upward to fill the welding chamber first, then when the welding chamber was fully filled they began to flow into the extrudate. But this process is slower if observed from side A to side B around the billet axis for the every single one of surface 4 to 7. It can be seen from side B at the same ram displacement they were still moving outward to the outer wall of the welding chamber. It is notable that observing from side A surface 8 (brown) will not experience a welding chamber filling process, but enters the extrudate directly. As mentioned above, this change is slower if the metal flow is observed rotationally around the billet axis from side A to side B. It is shown in Figure 6.14 (b) that

surface 8 was moving outward in the welding chamber although finally the upper part of the material of it will also flow into the die orifice to form the extrudate. Surface 9 and surface 10 travelled to the extrudate and formed the inner surface of the tube extrudate. The formation of the outer surface of the tube is complex because observed from side A it can be seen in Figure 6.14(a) the outer surface formation material is on surface 7 while it becomes surface 8 when the view orientation is changed. Therefore it is safe to say that the outer surface formation material is moving towards the billet surface direction as the ram progresses. Nonetheless, in general the central material of the billet forms the inner wall of the tube extrudate and the outer material of the billet forms the outer wall of the tube extrudate.

It is not surprising that the dead metal zone (DMZ) will form between the bridge top and the container wall. It should be also noted that as above-mentioned after the flow front moved outward and upward and finally filled the welding chamber, it will stay there and form another DMZ. These all can be seen in Figure 6.15.

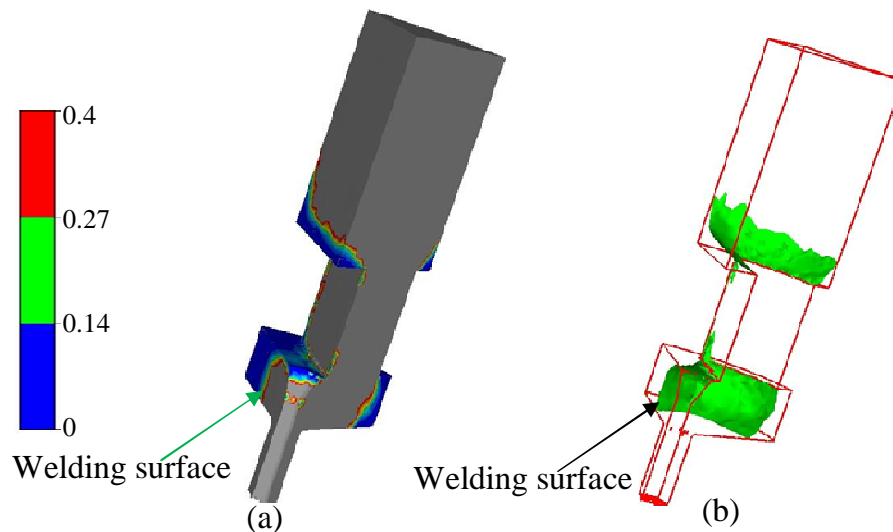


Figure 6.15 DMZs in tube extrusion (mm/s) shown (a) in filled contours (b) in iso-surfaces

Figure 6.15(a) displays the materials whose velocities are less than 0.4 mm/s in colour contours and Figure 6.15(b) shows the iso-surfaces of a velocity of 0.2mm/s. Besides the DMZ formed by the corner the bridge top and the container there is a large DMZ in the welding chamber which becomes thicker under the bridge, it even extends to the adjoining area of the mandrel and the bridge. Small DMZs also appear at the top and bottom of the sharp corner line of the porthole.

6.3.5 Weld seam formation and its quality criteria

Being a cost-effective method of producing tubular and hollow profiles, hot extrusion is extensively used in the aluminium industry. For low- and medium-strength aluminium alloys, a tubular profile can be easily produced using a conventional direct extrusion press and a porthole die. Upon entering the mandrel of a porthole die, the billet metal is split into distinct metal streams, which then rejoin and become welded by high pressure in the welding chamber of the die, and finally the tubular profile gains its shape and dimensions in the die bearing (Liu *et al.* 2007).

A drawback of using such an extrusion tooling setup is that the tubular or hollow profile so produced contains a number of weld seams along its length. For most of non-structural applications of tubular and hollow extrusions, the weld seams do not pose problems in terms of mechanical properties. However, for load-carrying structural applications, the quality of bonding at the weld seams is often a concern (Liu *et al.* 2007). While it is known that the weld seam formation is a solid-state bonding process during bridge die hot extrusion (Valberg 2002), due to the complex thermal and mechanical conditions inside the welding chamber and a large number of geometric parameters of dies, reliable inspection techniques and universal quality criteria for the weld seam are difficult to establish. Nonetheless, Akeret (1972) developed the pressure criterion that considers that the pressure, P , along converging streams' interface in the weld chamber should be high enough.

The weld seam can be assessed as:

$$P > constant \quad (6.1)$$

Bourqui (2002) found to obtain healthy weld seams the pressure in the weld chamber should exceed a critical value which is half the die entrance pressure, that is:

$$P_{weld} > P_{die\ entrance} \quad (6.2)$$

The pressure criterion can thus be normalised by effective stress:

$$\frac{P}{\sigma} > constant \quad (6.3)$$

Taking into the effect of time on seam welding, Plata and Piwnik (2000) proposed the pressure-time criterion that is based on the integral on time of contact pressure, normalised on the effective stress along the welding path, which can be expressed mathematically:

$$\int \frac{P}{\sigma} dt > constant \quad (6.4)$$

Donati and Tomesani (2004) argued that the pressure-time criterion overestimates the welding effect in the dead metal zones in the welding chamber where residence times are nearly infinite. They suggested a criterion that is a pressure-time-flow related as follows:

$$\int \frac{P}{\sigma} dt \cdot v = \int \frac{P}{\sigma} dl > constant \quad (6.5)$$

By comparing calculated results with Valberg' experiments (2002), a weld seam

quality criterion that takes pressure on the welding interface, effective stress and weld chamber height into consideration was proposed by Donati and Tomesani (2004):

$$\frac{1}{m} \int \frac{P}{\sigma} dt \cdot v = \frac{1}{m} \int \frac{P}{\sigma} dl > constant \quad (6.6)$$

where m is the welding chamber height and l is the welding path.

However huge difficulties exist in incorporating the equation (6.6) with FE softwares. First in FE simulation contact pressure between two metal streams cannot be read when assuming the welding plane as a symmetry plane. Second it is also very difficult to know the exact total contact time of the neighbouring metal streams because formidably advanced FE knowledge could be involved to detect the starting point of contact that varies across the welding plane in the welding chamber. Lastly no literature gives a universal critical constant for the criterion except that a rule of thumb that qualitatively the larger the value is, the better the weld seam is accepted.

In view of the difficulties applying the equation (6.6) directly into FE codes, researchers (Bourqui *et al.* 2002) either turned to simpler criterion such as the equation (6.1) or resorted to making assumptions to simplify the equation (6.6) (Liu *et al.* 2008). In Liu *et al.*'s work, welding pressure was represented by the mean stress

$$\sigma_m = \sigma_1 + \sigma_2 + \sigma_3 \quad (6.7)$$

where σ_m is the mean stress, σ_1 , σ_2 and σ_3 are the three principal stresses. And the contact time, t_w , of two metal streams was estimated by the quotient of the height of the welding chamber, h_{ch} , and the average flow velocity of the metal in

the chamber, v_{avg} ,

$$t_w = \frac{h_{ch}}{v_{avg}} \quad (6.8)$$

Now observe the Oyane damage law

$$C_{cr} = \int_0^{\bar{\epsilon}} \left(1 + 3 \cdot \frac{\sigma_m}{\bar{\sigma}}\right) d\bar{\epsilon} = \int_0^{\bar{\epsilon}} \left(1 + 3 \cdot \frac{\sigma_m}{\bar{\sigma}}\right) d\dot{\bar{\epsilon}} \cdot dt \quad (6.9)$$

and compare it with the equation (6.4), because it can be seen from Figure 6.16 that the strain-rate inside the welding chamber is small and doesn't vary greatly, to a great extent the equation (6.9) can be used to qualitatively represent the equation (6.4).

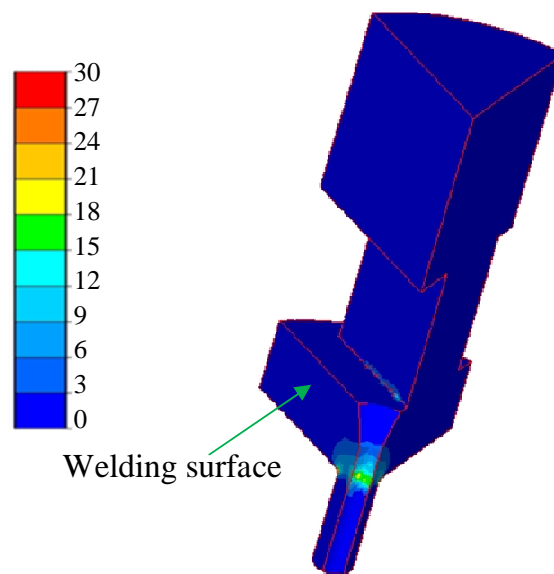


Figure 6.16 Strain-rate distribution in tube extrusion (s^{-1})

During hot extrusion through the porthole die, the weld seam formation is a solid-state bonding process. As the time needed for diffusion to proceed is highly limited in the welding chamber, adhesive bonding under pressure may be the

predominant mechanism. Thus, the contact time between two metal streams is expected to have a minor effect on the welding quality. Of more importance to the weld quality are the yielding of the material that is a function of temperature and the welding pressure affected by the dimensions of the welding chamber. Values higher than critical ones must be applied in the welding chamber to crush the asperities (roughness) of the metal streams through plastic deformation and to realise strong adhesion between the two neighbouring metal streams. Of course, the critical welding pressure required decreases as the yielding strength of the workpiece decreases or the temperature on the welding plane in the welding chamber increases. Therefore, the effect of ram speed on the weld quality is actually stronger because of its effects on temperature, yielding and the critical welding pressure required than through its effect on contact time (Liu *et al.* 2008).

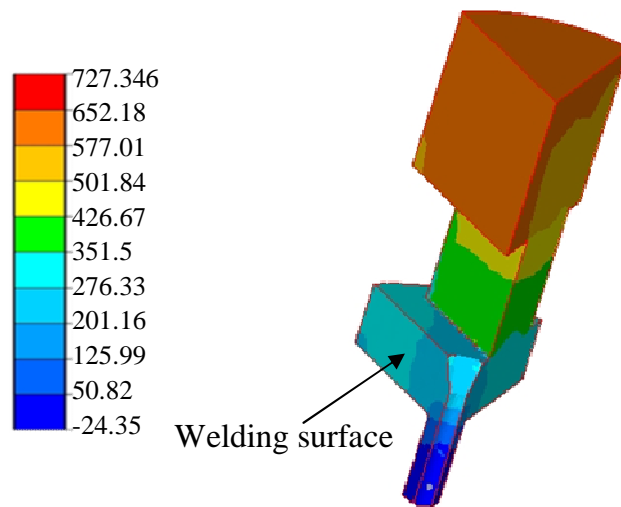


Figure 6.17 Mean stress distribution of tube extrusion (*MPa*)

Figure 6.17 shows the mean stress distribution of the billet at steady state in tube extrusion. It can be seen from it that the mean stress decreases from the container wall towards the mandrel in the welding chamber. From the top to the bottom of the chamber it decreases as well in the metal material next to the mandrel. Its value reduces to the minimum the extruded tube wall because of the pressure relief

when the material runs out of the die orifice through the die land.

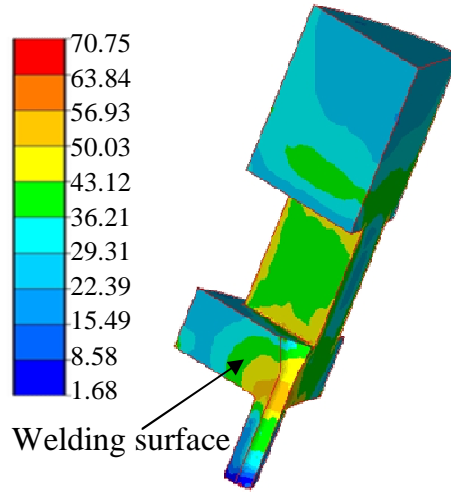


Figure 6.18 Effective stress distribution of tube extrusion (*MPa*)

Figure 6.18 shows the effective stress distribution that displays a similar distribution with that of the mean stress in the welding chamber. As stated earlier, it is an indicator of the combined result of temperature, strain and strain-rate. On the contact interface of the two streams, welding process could be easier to proceed when the effective stress is lower.

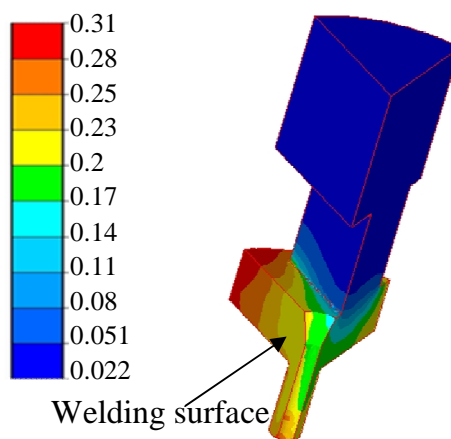


Figure 6.19 Weld quality index

Figure 6.19 shows the calculated weld seam quality using the equation (6.9) in which higher value denotes better welding quality. It indicates that better seam quality appears on the outer side of the tubular extrudate.

6.3.6 The simulation of one-third self-contact model

The symmetric features of extrusion are normally utilised to facilitate the FE simulation. However, its more important function in bridge die extrusion simulation is to avoid unnecessary self-contact problem in FE simulation. For example, in the above-studied tube simulation, instead of using the one-sixth model, if one-third model (as shown in Figure 6.3 that line OB and OC represent the two symmetry planes) is used self-contact mechanism will have to be triggered for the simulation to proceed because across the bridge the two streams will meet and bond under this arrangement. Furthermore, if the extruded cross-section is not symmetric or the cross-section is symmetric but the bridge is not coincident with the weld seam, self-contact cannot be evaded.

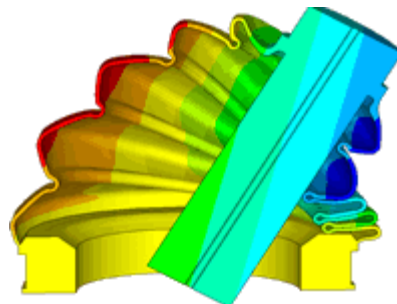


Figure 6.20 A self-contact example by Ansys[®] (Ansys 2010)

In fact, during metal forming processes, in some cases some areas of the billet may contact with themselves. Hence, a specific contact algorithm needs to be activated to manage the self-contact zones in order to correctly predict the material flow and provide a reliable estimation of the fold formation and its position. So far, most popular FE codes, such as Marc[®], Abaqus[®] and Deform[®], have claimed they have

the capability of dealing with self-contact problems. A typical example of this application is shown in Figure 6.20 in which the thinner upper material contacts itself under deformation. Unfortunately, none of these self-contact algorithms are robust enough to cope with the bridge die extrusion simulation. Divided by the bridges when the highly distorted elements meet again in the welding chamber, the software tries to remesh continuously or aborts the simulation prematurely because of the penetration of elements in the vicinity of the weld seam.

In the cases of a simulation in which self-contact of the neighbouring weld seams is inevitable, there could have several alternative methods:

- 1) Steady state assumption. Under this assumption, during the whole bridge die extrusion its major field variables are regarded as constant. And in the very beginning of the simulation, the billet is one that has filled the weld chamber so that there will not self-contact possible during the simulation. However, it is apparently that unless perfect boundary conditions are applied to this billet, the reliable information that can be acquired would only be connected with the metal flow;
- 2) Arbitrary Lagrangian and Eulerian (ALE) method. Some FE codes, like Hyperxtrude[®] and DiekA[®] employ ALE method to simulate complex hollow section extrusion. But these codes are still developing and far from being well-established. Of which DiekA[®] is still an in-house software that is confined to be used in a limited academic and industrial circle. Although Hyperxtrude[®] is a commercial FEM software, it lacks a powerful and flexible user-subroutine interface;
- 3) Two-step method. Quite recently Xie *et al* (2009) proposed a two-step method to simulate bridge die extrusion. Based on Deform-3D[®], the 3-dimensional solid FE model is converted into a stereolithographic (STL) model that is a 3-dimensional surface model composed of small triangles when the penetrated volume is equal to the unfilled volume (see Figure

6.21(b)). Then the STL model is repaired with Pro/Engineer[®] according to the Volume Conservation Law (see Figure 6.21(c)). Subsequently, the fixed STL model is imported into the original FE model and the nodal variables of the penetrated model are assigned to the repaired one and successful simulation can therefore be continued. At first glance, this method seems to be a good solution. But it applies artificial operations to the mesh and field variables for the newly generated nodes that fall within the unfilled areas before the reparation must be created by the user, which makes the simulation results doubtful.

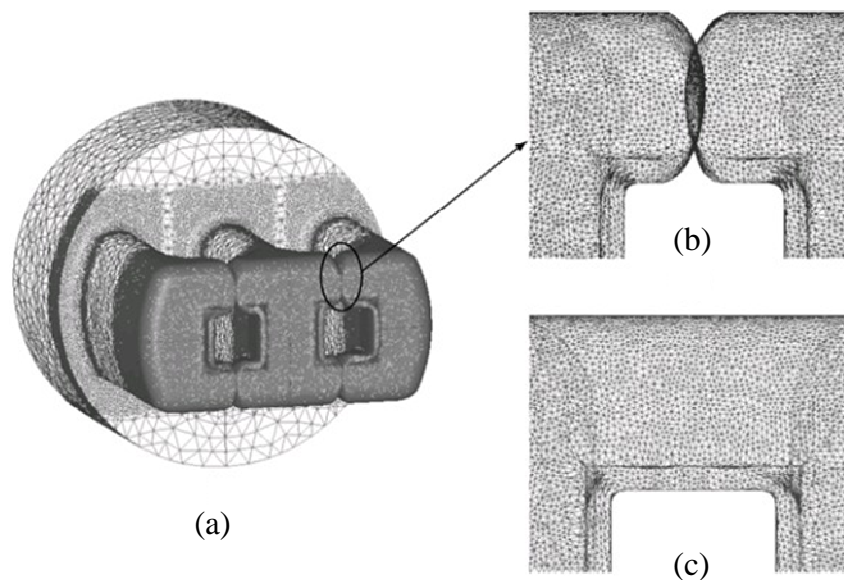


Figure 6.21 FEM model of penetrated mesh on welding surface before and after mesh repairing: (a) mutual penetration meshes on welding surfaces; (b) before mesh repairing; (c) after mesh repairing (Huang *et al.* 2010)

Forge[®] includes an exclusive formulation with a new element type enabling the computer to automatically handle self-contact and contact between multiple deformable bodies. Forge2009[®] has further improved self-contact nodes detection. Therefore it is worthwhile to test its capability in this field by bridge die extrusion simulation for future work.

6.3.6.1 One-third self-contact FE model

The one-third FE model is shown in Figure 6.22 in which all of the elements are one-third of the real situation and the symmetry planes are corresponding with the lines OB and OC in the Figure 6.3. The other boundary conditions are same as those in the one-sixth FE simulation.

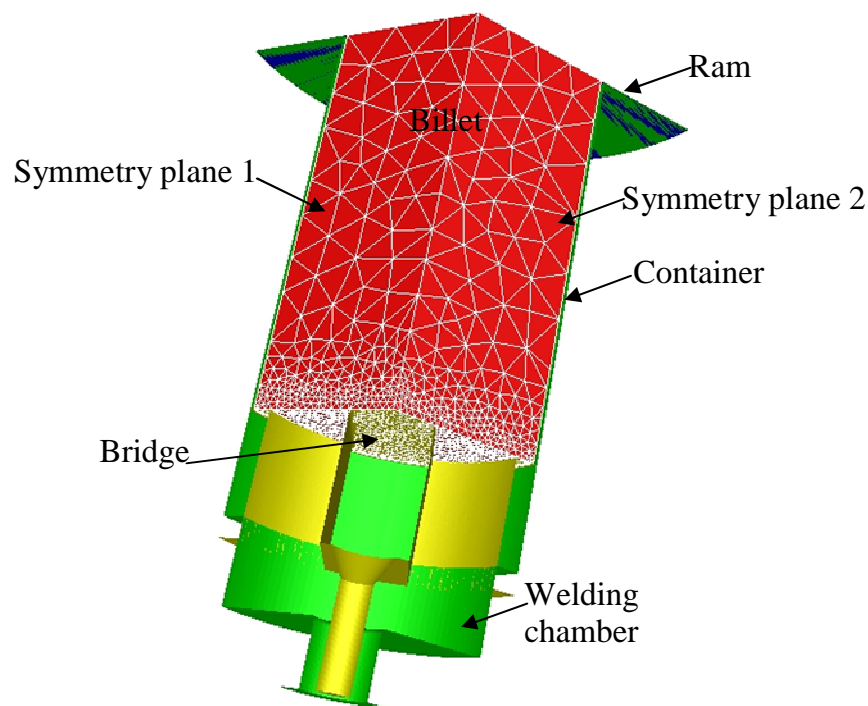


Figure 6.22 One-third model of the tube extrusion

Figure 6.23 are successive steps showing the process seam bonding process. The blue colour represents the contact degree of the material with the tools. The darker the blue is, the firmer is the contact. The red colour means there is no contact with other object. It can be seen that without manual interference with the simulation, at the ram displacement of 34mm a perfect seam bonding process was successfully realised. Without doubt, compared with the aforementioned the oversimplified steady-state assumption method, unsatisfactory ALE method or the unreliable and cumbersome two-step method, Forge2009[®] has great potential to resolve the self-

contact problem perfectly.

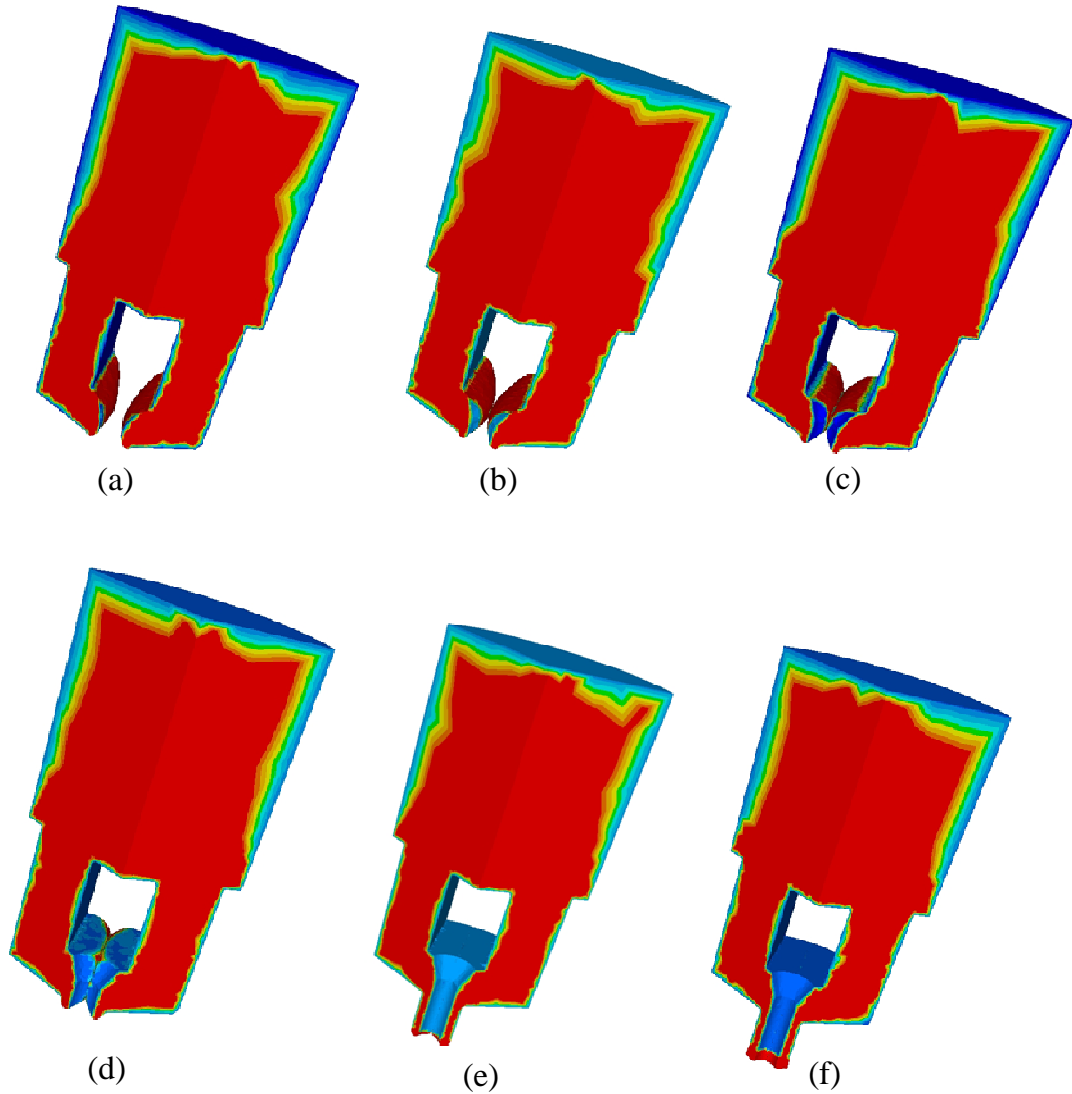


Figure 6.23 Metal flow of two neighbouring streams at the ram displacements of (a) 27 (b) 28 (c) 29 (d) 30 (e) 31 (f) 34 *mm* in the self-contact model

6.3.6.2 Predicted load, temperature and equivalent strain using the one-third model

Predicted load

Figure 6.24 is the predicted load evolution versus ram displacements using the one-third self-contact model, which highly resembles the Figure 6.5 with comparable values. The curve in Figure 6.24 clearly displays several distinct stages of the billet deformation that are the upsetting, splitting, welding-chamber filling (seam bonding) and extrudate formation. The predicted peak load is 252 tons which is only 3.6% lower than the experimental result 261 tons (Nisaratanaporn 1995).

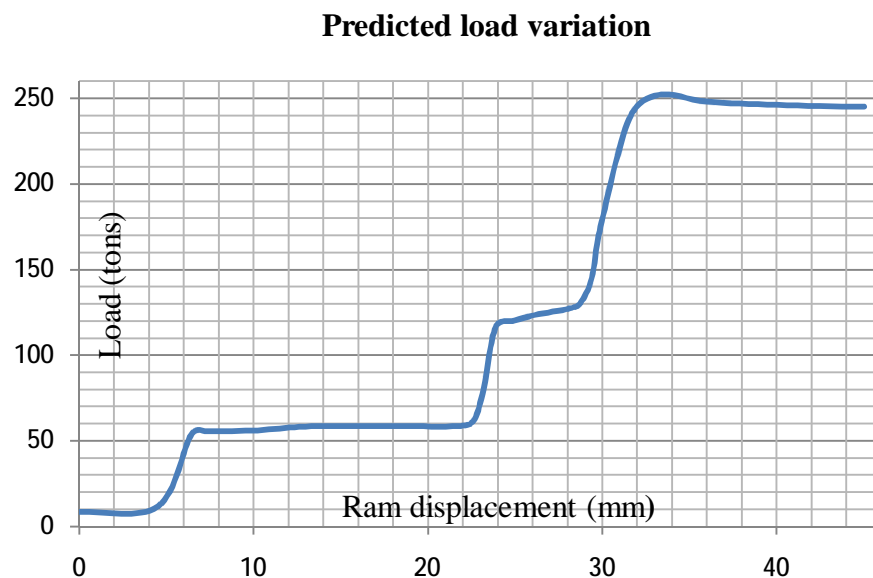


Figure 6.24 Load evolution versus ram displacement using one-third model

Temperature and equivalent strain distribution

Figure 6.25 is the temperature distributions at the ram travel of 40mm for both one-third and one-sixth models. At first glance the distributions are similar although it looks that one-third model gets lower values. It is hard to say which distribution is close to the reality since there are no experimental results to refer to. However the one-third model displays an important feature of the temperature distribution in bridge-die extrusion that is the temperature gradient from the welding surface to the non-welding area, which is marked in Figure 6.25. It is shown in Figure 6.25(a), not only does there exist a temperature gradient in the

thickness of the tube extrudate but also the temperature is higher on the weld seam than its neighbouring material. Similar phenomena can also be observed by comparing the equivalent strain results from these two methods in Figure 6.26.

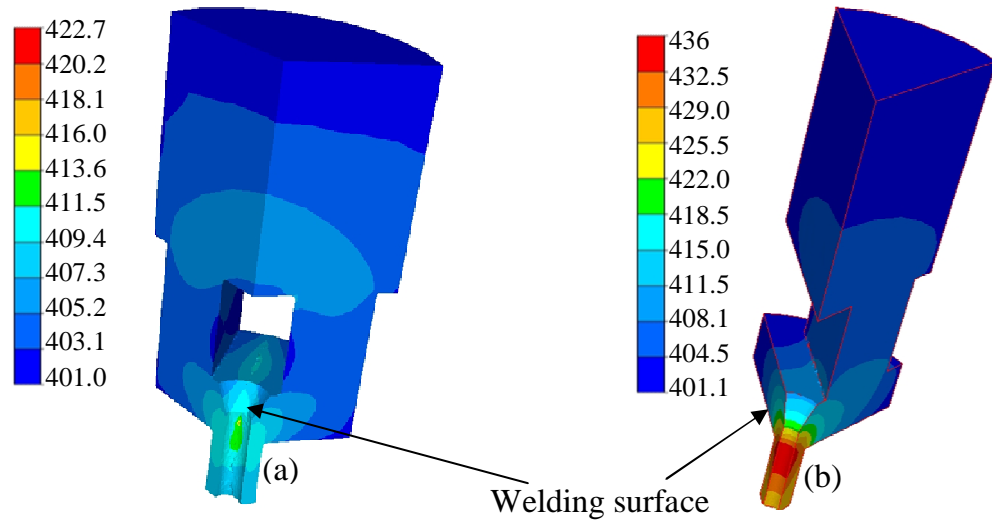


Figure 6.25 Temperature distribution at the ram displacement of 40mm (a) one-third model and (b) one-sixth model

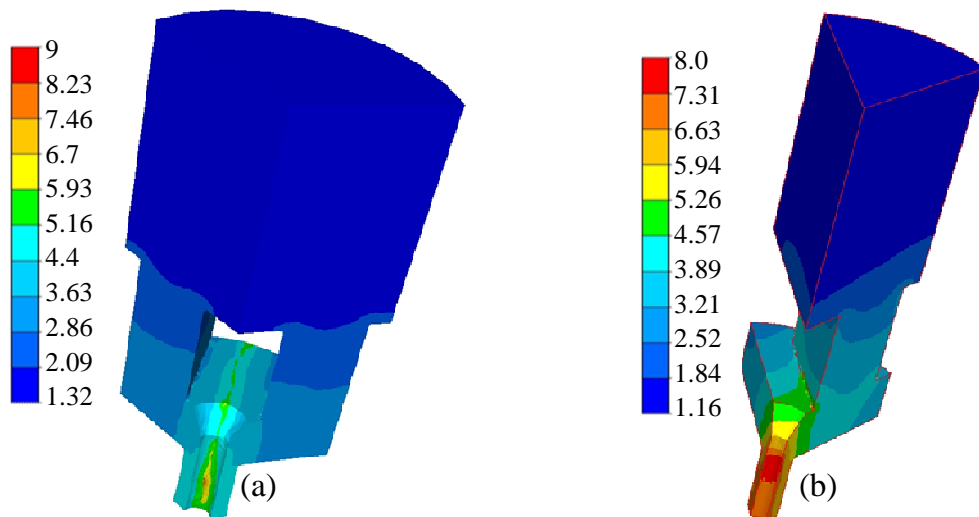


Figure 6.26 Equivalent strain distribution at the ram displacement of 40mm (a) one-third model and (b) one-sixth model

The significance of the difference of the predicted results from the two models

The positions where the samples were taken are illustrated in Figure 6.27. In the Figure 6.27 the cross-section of the tube are divided into two regions: weld region near the weld line and non-weld region. They are further divided into three areas: outer surface area, inner surface area and mid-radius area according to their positions on the tube wall.

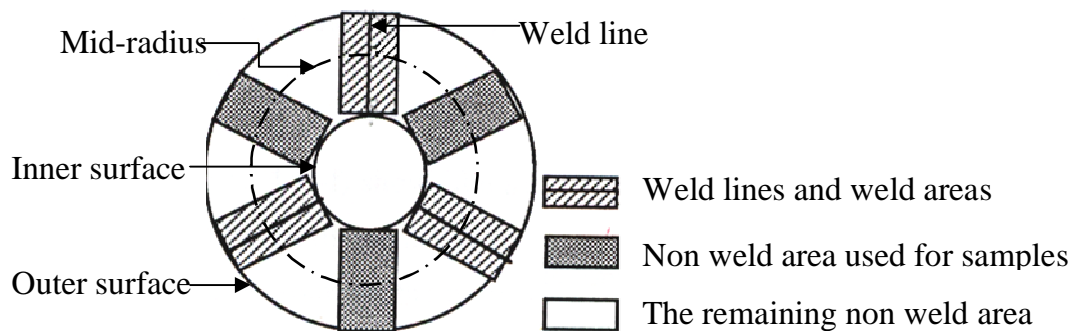


Figure 6.27 The weld and non weld areas (Nisaratanaporn 1995, p.149)

The microstructures variations across the extrudate cross-section of the as-extruded microstructures of tube extrudates are shown in Figure 6.28. Figure 6.28(a) and (b) are the as extruded microstructure at the outer surface of the tube extrudate when the initial temperature is 350°C in the weld area and non-weld area respectively. The recrystallisation is more complete in the weld area than in the non-weld area and the grains are also smaller in the weld area. At the same temperature, the microstructures at the mid-radius area are shown in Figure 6.28(c) and (d). Again the finer grains appeared in the weld area. Figure 6.28(e) and (f) compares the as extruded microstructure at the inner surface of the tube extrudate when the initial temperature is 450°C. In the inner surface area although some larger grains formed because of secondary recrystallisation, the primary recrystallised grain size is smaller in the weld area. These are all due to the higher temperature and higher strain in the weld area (Nisaratanaporn 1995, p.150). Compared with the one-sixth model, the one-third model can well predict the

temperature and strain distribution difference between the weld area and non-weld area in the tube extrusion. This feature presents the one-third model the potential to more accurately predict the microstructure evolution, hence, the mechanical properties prediction of the weld seam.

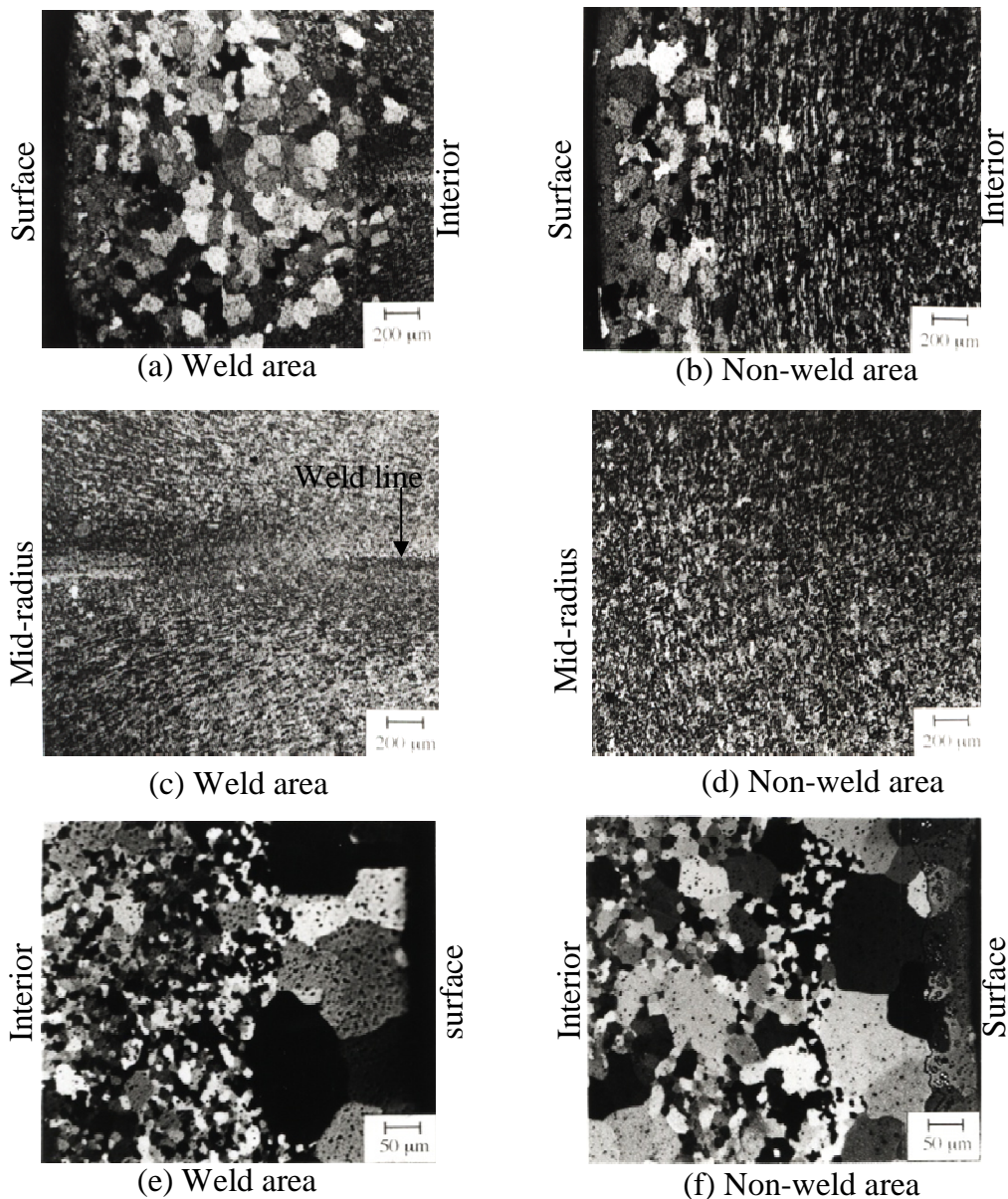


Figure 6.28 Microstructure of tube extrudate (as extruded, transverse section, I/D=4mm, O/D=16mm) (Nisaratanaporn 1995, p.151-153) (a),(b) at the tube outer surface, (c),(d) at the mid-radius area, (e) and (f) at the tube inner surface

6.4 Concluding remarks

Based on the discussion of this chapter, a few conclusions are drawn:

1. The Zener-Hollomon equation is suitable for numerical simulation of hot aluminium extrusion. A new set of constants were calculated. They can well describe flow behaviour of the AA6063 alloy at elevated temperatures.
2. The predicted load for tube simulation is very close to the experimental result. The temperature variation with time during a tube extrusion is more complex than that of the solid section extrusion because of the influence of the bridge. Tube extrusion also shows a different temperature distribution across the extrudate cross-section from the equivalent of the solid section extrusion: the temperature of the inner wall of the tube is higher than the outside wall.
3. Both grid method and surface method were used to observe the complicated material movement during tube extrusion. The predicted metal flow was compared with the experimental macrograph and they agree well. The detailed analysis of the predicted metal flow results indicate that the material at the centre of the billet forms the inner surface of the tube whilst the materials forming its outer surface are mainly from the outer part of the billet enclosed by two planes $\pm 15^\circ$ around the billet axis from the symmetry plane of the porthole.
4. It is widely accepted that the pressure in the weld chamber and the total contact time of the materials from the neighbouring metal streams are the most important factors that decide the weld seam quality. Although existing criteria that consider the influences of both contact time and pressure on the weld seam are difficult to be incorporated into the FE calculation, weld seam quality can be qualitatively evaluated by the Oyane damage law.

Simulated result shows that according to this law the outer surface area of the tube extrudate would have better weld quality than the inner surface area.

5. Compared with other popular FE packages, Forge2009[®] can better handle the self-contact problem because it avoids having to use the steady-state assumption and modifying the penetrated meshes manually. More importantly, unlike the one-sixth model, the one-third self-contact FE model can capture the temperature and strain gradients that vary from the weld seam to the non weld area, which is more realistic according to the comparison with the experimental measurements of microstructure. Therefore, although the self-contact FE model is more time-consuming, it is highly recommended to resolve more complex hollow section extrusion simulation, especially when microstructure prediction is considered.

7. Conclusions and further research

7.1 Conclusions

1. Commercial FEM codes, such as Forge2009[®], are suitable to accurately simulate hot extrusion and heat treatment processes.
2. Industrial extrusion of complex solid or hollow sections can now be efficiently simulated in order to predict the major extrusion parameters, such as pressure, temperature, strain, strain rate, stress and material flow.
3. Fundamental differences in surface formation between direct and indirect extrusions demonstrate the influence of the different modes on the productivity. Indirect extrusion can lead to higher productivity and a more homogeneous structure.
4. Microstructure evolution can be simulated by the integration of physically and semi-physically based metallurgical models with Forge2009[®]. These models predict the major internal state variables such as subgrain size, misorientation, dislocation density, volume fraction recrystallised and recrystallised grain size.
5. The Zener-Hollomon formulation is the most accurate equation to represent the flow stress in hot extrusion of aluminium alloys. However, caution must be given in the selection and processing of flow stress data in order to accurately represent the alloy's flow behaviour. In this thesis, a new set of constants for the AA6063 alloy were calculated and successfully applied to a hollow tube extrusion simulation.
6. Hollow section extrusion is more difficult to simulate because of the complexity of the tooling. The predicted load curve has numerous turning

points due to the billet upsetting, billet-dividing, welding-chamber filling and the hollow extrudate forming stages. The metal flow pattern is complex and comprises several DMZs.

7. Weld seam quality is still a serious concern for hollow extrusion. A universally accepted criterion for the formation of good quality weld seams still needs to be developed. However, the equation for the Oyane damage law can be used to qualitatively evaluate the weld seam quality.
8. Symmetry is often utilised to avoid self-contact problems with hollow section extrusion modelling. However, it is worthwhile to investigate the FE model with self-contact because under some circumstances self-contact is not avoidable. This study shows that Forge2009[®] is capable of dealing with the self-contact problem in the hollow extrusion simulation, without the need of over-simplified assumption or manual interference during the simulation. It also indicates that results from the self-contact model are closer to the real situation; therefore, the self-contact model should be used to achieve more realistic microstructure predictions.

7.2 Further research

1. Although reasonable results have been achieved for the simulation of solid and hollow sections, there is still much work to be done in this area. For instance, currently all the tools are assumed to be rigid to save simulation time. This assumption makes it impossible to get the temperature and deformation distribution in the tools, which is acceptable for normal extrusion, but definitely not for precision extrusion or occasions when deformation of the tool greatly affects the product quality. For example, the

deformation of the die land or the bridge die (with hollow sections) could significantly alter the extrudate profile.

2. Physically-based structure evolution models that can be incorporated into the FEM simulation have been widely regarded to be better than empirical models. However, this study shows that both empirical and semi-empirical models have to be used because of the lack of a suitable physically-based microstructure evolution model. The physically-based models that are currently available are either flawed or not suitable for aluminium extrusion. This demonstrates the need for more experimental study in order to enhance the understanding of microstructure evolution mechanisms and to reduce the amount of tuning parameters in various models.
3. The simulation of hollow sections is becoming more common and therefore appropriate self-contact algorithms must be developed.
4. Although in this thesis other numerical methods were not used, in the future it is sensible to combine FEM with other advanced methods, such as cellular automata, artificial neural networks and genetic algorithms, in order to make better microstructure analyses and to optimise the die design.

8. Appendix A

Datafile for a 3D T-section extrusion

```
! File Type:                FORGE3 V7.4 Data File
! Creator:                  GLpre Version 3. 2. 0. 24-Release
! Project name:             tshape
! Project description:      Empty_Generic_Project
! Simulation name:          Textrusion
! Simulation description:    3D_Hot_Forging
! Author:                   niu
! Creation Date:            2010-08-25 00:43:34
! GLPre active language:    English
! System language:          English (United States)
! Data File Name:           textrusion.ref
! Data File Location:       C:\User_niu\Tshape\100824\tshape.tsv\Textrusion\
!!!!!!!!!!!!!!!!!!!!!!!!!!!!!!!!!!!!!!!!!!!!!!!!!!!!!!!!!!!!!!!!!!!!!!!!!!!!
```

```
!===== OBJECTS Block
```

```
.OBJETS
```

```
    ProjectName = tshape
    SimulationName = Textrusion
    Fout = textrusion.out
    Fres = results\textrusion.res
    Faux = results\textrusion.vtf
    NBSD = 1
    objet 1, NAME=Billet
    objet 1, FMAY=billet.may
    objet 1, NomGen=results\billet_
    objet 1, rheol=1
    outil 1, NAME=LowerDie
    outil 2, NAME=ram
    outil 3, NAME=container
```

```
.FIN OBJETS
```

```
!=====
```

```
!===== APPROXIMATION Block
```

```
.APPROXIMATION
```

```
    Periode_Meca = 1
```

```
.FIN APPROXIMATION
```

```
!=====
```

```
!===== UNITS Block
```

```

.UNITES
  MM-MPA-SI
.FIN UNITES
!=====

!===== RHEOLOGY Block
.RHEOLOGIE

!!!!!!!!!!!!!!!!!!!!!!
MATERIAU 1 ! (object Billet)
!!!!!!!!!!!!!!!!!!!!!!
  EVP
  LOIV SIG0
  ZENER-H
  PAR DH = 148880.d0
  PAR R = 8.31d0
  PAR alpha = 0.016d0
  PAR n = 4.27d0
  PAR A = 325215956.1d0
  FIN LOI

!Elasticity coefficients
Youngmodulus = 7.300000e+04
Poissoncoeff = 0.300000

!Thermal coefficients
mvolumique = 2.800000e+03 !Density
cmassique = 1.230000e+03 !Specific Heat
conductmat = 2.500000e+02 !Conductivity
epsilon = 5.000000e-02 !Emissivity

!-----
OUTIL1          ! LowerDie
  File = lowerdie.tof

!Friction between deformable object and rigid die
tresca
mbarre = 4.000000e-01

!Thermal Exchange between part and rigid die
! Unit = si
alphat = 2.000000e+03      ! Transfert coefficient
effus = 1.176362e+04 ! tool effusivity

Temp_Die = 300.000000

```

```

FIN OUTIL
!-----

!-----
OUTIL2          ! ram
  File = ram.tof

  !Friction between deformable object and rigid die
  tresca
  mbarre = 4.000000e-01

  !Thermal Exchange between part and rigid die
  ! Unit = si
  alphas = 2.000000e+03      ! Transfert coefficient
  effus = 1.176362e+04 ! tool effusivity

  Temp_Die = 300.000000
FIN OUTIL
!-----

!-----
OUTIL3          ! container
  File = container.tof

  !Friction between deformable object and rigid die
  tresca
  mbarre = 9.000000e-01

  !Thermal Exchange between part and rigid die
  ! Unit = si
  alphas = 2.000000e+03      ! Transfert coefficient
  effus = 1.176362e+04 ! tool effusivity

  Temp_Die = 300.000000
FIN OUTIL
!-----

  !Thermal Exchange between deformable object and ambient medium
  ! Unit = si
  AlphasExt = 10.000000e+00 ! Transfert coefficient
  TempExt = 50 ! Ambient Temperature

  ! Initial temperature has been set in mesh file: already exists in mesh file

!!!!!!!!!!!!!!!!!!!!!!

```


FIN MATERIAU

!!!!!!!!!!!!!!!!!!!!

! *** User Variable Law: ZENERH

LOIV MECA

ZENERH

Par STRAIN_RATE = EXIST

Par DH1 = 148880.0

Par R1 = 8.3143

Var ZEN-HOLLOMON = 0.

FIN LOI

! *** User Variable Law: BOX

LOIV UTIL

BOX

Par XMIN = -100

Par XMAX = 100

Par YMIN = -100

Par YMAX = 100

Par ZMIN = -20

Par ZMAX = -10

Par EQ_STRAIN = EXIST

Eta EQ_STRAIN-BOX = 0.

FIN LOI

! *** User Variable Law: Tens_Def

LOIV INTG

Tens_Def

Eta TDEF(6) = 0, 0, 0, 0, 0, 0

FIN LOI

! *** User Variable Law: SigmaCylZ

LOIV MECA

SigmaCylZ

Par STRESSTENSOR(6) = EXIST

Var TENS_CYL(6) = 0, 0, 0, 0, 0, 0

FIN LOI

Stock=ZEN-HOLLOMON,TENS_CYL

! *** User Variable Law: PRINC_VAL_1

LOIV MECA

PRINC_VAL_1

PAR TDEF(6) = EXIST

VAR TDEF1= 0.d0

FIN LOI

! *** User Variable Law: PRINC_VAL_2

LOIV MECA

PRINC_VAL_2

PAR TDEF(6) = EXIST

VAR TDEF2= 0.d0

FIN LOI

! *** User Variable Law: PRINC_VAL_3

LOIV MECA

PRINC_VAL_3

PAR TDEF(6) = EXIST

VAR TDEF3= 0.d0

FIN LOI

! *** User Variable Law: MY

LOIV MECA

MY

var Hydro= 0.d0

FIN LOI

Stock=TDEF1,TDEF2,TDEF3, Hydro

! *** User Variable Law: SV_NIU

LOIV UTIL

SV_NIU

PAR D0_GRN = 50.0d-6

PAR TDEF1 = EXIST

PAR TDEF2 = EXIST

PAR TDEF3 = EXIST

PAR eq_strain=EXIST

ETA SV_NIU = 0.d0

ETA SV_OLD = 0.d0

ETA SV_New = 0.d0

FIN LOI

! *** User Variable Law: MY_SUB

LOIV UTIL

MY_SUB

Par A2024 = -0.5778d0

Par B2024 = 0.0378d0

Par C2024 =40.0d0

```

par di_val=50.0
par eq_strain=EXIST

par cd_val=1.48d-4
par g_val1=2.05d10
par burgers=2.86d-10
par misori= 3.0d0
par misori_c=15.0d0

par cmgb=3.07d11
par mgb_a=251.0
  Par STRAIN_RATE = EXIST
  Par DH_b = 152000.0d0
par cxv=0.693d0

par txv=3600.d0
par kxv=2.0d0
  par crex=2.347d0
  par delta_t=exist
  par Rg=2000.

par SV_NIU= exist
par ZEN-HOLLOMON= exist

Eta zener_1 = 1.d0
Eta subgrain = 1.d0
Eta D_Density = 1.d8
Eta pd01 = 1.d0
Eta pd02 = 1.d0

Eta pd03= 1.d0
Eta pd04 = 1.d0
Eta pd05 = 1.d0
Eta pd06= 1.d0
Eta pd= 1.d0

Eta SV_NIU2= 1.d0
Eta nv = 1.d0
Eta t50 = 1.d0
Eta t501= 1.d0
Eta t502= 1.d0

Eta t503 = 1.d0
Eta t504= 1.d0
Eta t505= 1.d0

```

Eta t506 = 1.d0
Eta t507= 1.d0

Eta t508= 1.d0
Eta t509 = 1.d0
Eta t510= 1.d0
Eta t511= 1.d0
Eta grain= 50.d-6

Eta xv = 1.d0
Eta xv1 = 1.d0
Eta xv2= 1.d0
Eta xv3 = 1.d0
Eta xv4 = 1.d0

Eta xv5= 1.d0
Eta xv6 = 1.d0
Eta xv7 = 1.d0
Eta xv8= 1.d0
Eta xv9 = 1.d0

Eta xv10 = 1.d0
Eta xv11= 1.d0

Eta subg1= 40.d-6
Eta subg2= 40.d-6
Eta subg3= 40.d-6
Eta subg4= 40.d-6
Eta subg5= 40.d-6

Eta subg6= 40.d-6
Eta subg7= 40.d-6
Eta subg8= 40.d-6
Eta subg9= 40.d-6
Eta subg10= 40.d-6

Eta subg11= 40.d-6
Eta subg12= 40.d-6
Eta subg13= 40.d-6
Eta subg14= 40.d-6
Eta subg15= 40.d-6

Eta misor1 = 0.01d0
Eta misor2 = 0.01d0
Eta misor3 = 0.01d0

Eta misor4 = 0.01d0
Eta misor5 = 0.01d0

Eta misor6 = 0.01d0
Eta misor7 = 0.01d0
Eta misor8 = 0.01d0
Eta misor9 = 0.01d0
Eta misor10 = 0.01d0

Eta misor11 = 0.01d0
Eta misor12 = 0.01d0
Eta misor13 = 0.01d0
Eta misor14 = 0.01d0

FIN LOI

!-----

INTERFACE
FIN INTERFACE

!-----

.FIN RHEOLOGIE

!=====

!===== INCREMENT Block

.INCREMENT

Deformation = 0.01

.FIN INCREMENT

!=====

!===== EXECUTION Block

.EXECUTION

Inertia

dtMin = 2.000000e-004

dtMax = 1.000000e-002

dhSto = 5.000000e-001

OBJET1

NO Folds_Detection

FIN OBJET

.FIN EXECUTION

!=====

!===== THERMAL Block

.THERMIQUE

.FIN THERMIQUE

!=====

!===== MESH BOXES Block

.BOITE

OBJET1

BOX 1

Type=20 ! CYLINDER
Eulerian
Size= 4
!Param Info: NbPar, Xcenter, Ycenter, Zcenter, Rext, Rint, H
Parameters: 6,0,0,0,47.8675,0,127.874
Matrix: 1, 0, 0, 0,
0, 1, 0, 0,
0, 0, 1, -75.9815,
0, 0, 0, 1

END BOX

BOX 2

Type=20 ! CYLINDER
Eulerian
Size= 2
!Param Info: NbPar, Xcenter, Ycenter, Zcenter, Rext, Rint, H
Parameters: 6,0,0,0,25.9087,0,123.536
Matrix: 1, 0, 0, 0,
0, 1, 0, 0,
0, 0, 1, -87.5904,
0, 0, 0, 1

END BOX

BOX 3

Type=20 ! CYLINDER
Eulerian
Size= 1
!Param Info: NbPar, Xcenter, Ycenter, Zcenter, Rext, Rint, H
Parameters: 6,0,0,0,19.435,0,46.1896
Matrix: 1, 0, 0, 0,
0, 1, 0, 0,
0, 0, 1, -26.0473,
0, 0, 0, 1

END BOX

FIN OBJET

.FIN BOITE

!=====

!===== BOUNDARY CONDITIONS Block

.CONDLIM

.FIN CONDLIM

!=====

!===== DAMAGE CONDITIONS Block

.DAMAGE

OBJET1

 Name = EQ_STRAIN-BOX

 Trigger Value = 0.0001

FIN OBJET

.FIN DAMAGE

!=====

!===== REMESHING Block

.MAUTO

OBJET1

 periode = 20

 lbase = 12

FIN OBJET

.FIN MAUTO

!=====

!===== KINEMATICS Block

.CINEMAT_OUT

 Outil2 ! ram

 maitre

 Axe = 3

 Fin Outil

.FIN CINEMAT_OUT

!=====

!===== PILOT Block

.PILOT

 NbPass= 1

 Pass1

 Fin Pass

.FIN PILOT

!=====

9. Appendix B

Take the calculation of the grain boundary surface area per unit volume as an example to illustrate the procedure to use the Forge2009[®] subroutine

1. In the data file

The user law SV_NIU was activated in the .RHEOLOGIE sub-module in the datafile, following codes were added

LOIV UTIL	user law type
SV_NIU	name of the user law
PAR D0_GRN= 50.0d-6	initial grain diameter
PAR TDEF1= EXIST	the first principal strain
PAR TDEF2= EXIST	the second principal strain
PAR TDEF3= EXIST	the third principal strain
ETA SV_NIU=0.d0	the state variable SV_NIU will be displayed in the post-processor
FIN LOI	declare the end of this user law

2. In the Fortran[®] subroutine

The following corresponding code lines must be added in the loiv_util.f file

```
else if (nom.eq.'SV_NIU') then
  if ((nbpar.ne.4).or.(nbeta.ne.1)) goto 99
  edge_tkd=7.0*gs_par(1)/(4*sqrt(6.0)+6.0*sqrt(2.0))
  sv0=3.0*(1+2.0*sqrt(3.0))/8.0/sqrt(2.0)/edge_tkd
  gs_eta(1)=sv0*0.5*(0.429*dexp(-1.0*gs_par(2))+0.571*dexp(-
1.0*gs_par(3))+dexp(-1.0*gs_par(4)))
```


10. Appendix C

Grain boundary area per unit volume when using a cube grain model

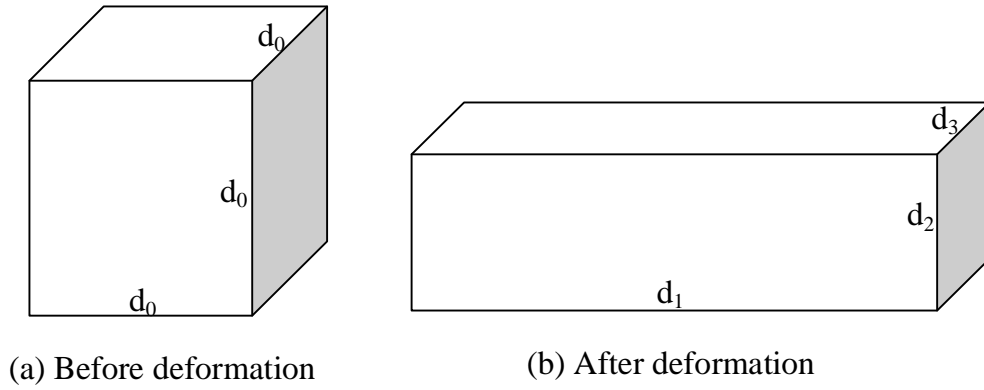


Figure 10.1 Grain shape (a) cube before deformation (b) block after deformation

Because $\varepsilon_1 = \ln \frac{d_1}{d_0}$, $\varepsilon_2 = \ln \frac{d_2}{d_0}$, $\varepsilon_3 = \ln \frac{d_3}{d_0}$, hence

$$d_1 = d_0 e^{\varepsilon_1}$$

$$d_2 = d_0 e^{\varepsilon_2}$$

$$d_3 = d_0 e^{\varepsilon_3}$$

After deformation

$$S_V = \frac{2(d_1 d_2 + d_2 d_3 + d_3 d_1)}{d_0^3} = \frac{2}{d_0} (e^{\varepsilon_1 + \varepsilon_2} + e^{\varepsilon_2 + \varepsilon_3} + e^{\varepsilon_3 + \varepsilon_1}) \quad (10.1)$$

Assume the extrusion is an axisymmetric process during which there is the relationship

$$2\varepsilon_2 = 2\varepsilon_3 = -\varepsilon_1 \quad (10.2)$$

Substitute (10.2) into (10.3)

$$S_V = \frac{2}{d_0} (e^{\varepsilon_1 + \varepsilon_2} + e^{\varepsilon_2 + \varepsilon_3} + e^{\varepsilon_3 + \varepsilon_1}) = \frac{2}{d_0} (2e^{0.5\varepsilon_1} + e^{-\varepsilon_1}) \quad (10.3)$$

If the deformation is plane strain compression, there are relations below

$$\varepsilon_2 = -\varepsilon_1 \tag{10.4}$$

$$\varepsilon_3 = \mathbf{0} \tag{10.5}$$

then

$$S_V = \frac{2}{d_0} (1 + e^{\varepsilon_1} + e^{-\varepsilon_1}) \tag{10.6}$$

11. Appendix D

The calculation of the effective strain

Strain tensor

$$\varepsilon_{ij} = \begin{pmatrix} \varepsilon_{xx} & \varepsilon_{xy} & \varepsilon_{xz} \\ \varepsilon_{yx} & \varepsilon_{yy} & \varepsilon_{yz} \\ \varepsilon_{zx} & \varepsilon_{zy} & \varepsilon_{zz} \end{pmatrix}$$

Deviatoric stress tensor

$$\varepsilon'_{ij} = \begin{pmatrix} \varepsilon_{xx} - \frac{\varepsilon_{xx} + \varepsilon_{yy} + \varepsilon_{zz}}{3} & \varepsilon_{xy} & \varepsilon_{xz} \\ \varepsilon_{yx} & \varepsilon_{yy} - \frac{\varepsilon_{xx} + \varepsilon_{yy} + \varepsilon_{zz}}{3} & \varepsilon_{yz} \\ \varepsilon_{zx} & \varepsilon_{zy} & \varepsilon_{zz} - \frac{\varepsilon_{xx} + \varepsilon_{yy} + \varepsilon_{zz}}{3} \end{pmatrix}$$

For ideal plastic deformation $\varepsilon_{xx} + \varepsilon_{yy} + \varepsilon_{zz} = \mathbf{0}$, and according the definition of the equivalent plastic strain,

$$\bar{\varepsilon}^p = \sqrt{\frac{2}{3} \varepsilon_{ij}{}^{ip} \varepsilon_{ij}{}^{ip}} = \sqrt{\frac{2}{3} \varepsilon_{ij}{}^p \varepsilon_{ij}{}^p}$$

therefore,

$$\begin{aligned}
\bar{\varepsilon}^p &= \frac{\sqrt{2}}{3} \sqrt{\left[(\varepsilon_{xx} - \varepsilon_{yy})^2 + (\varepsilon_{yy} - \varepsilon_{zz})^2 + (\varepsilon_{zz} - \varepsilon_{xx})^2 \right] + 6(\varepsilon_{xy}^2 + \varepsilon_{yz}^2 + \varepsilon_{zx}^2)} \\
&= \frac{\sqrt{2}}{3} \sqrt{2(\varepsilon_{xx}^2 + \varepsilon_{yy}^2 + \varepsilon_{zz}^2) - 2\varepsilon_{xx}\varepsilon_{yy} - 2\varepsilon_{yy}\varepsilon_{zz} - 2\varepsilon_{zz}\varepsilon_{xx} + 6(\varepsilon_{xy}^2 + \varepsilon_{yz}^2 + \varepsilon_{zx}^2)} \\
&= \frac{\sqrt{2}}{3} \sqrt{2(\varepsilon_{xx}^2 + \varepsilon_{yy}^2 + \varepsilon_{zz}^2) - [\varepsilon_{xx}(\varepsilon_{yy} + \varepsilon_{zz}) + \varepsilon_{yy}(\varepsilon_{zz} + \varepsilon_{xx}) + \varepsilon_{zz}(\varepsilon_{xx} + \varepsilon_{yy})] + 6(\varepsilon_{xy}^2 + \varepsilon_{yz}^2 + \varepsilon_{zx}^2)} \\
&= \frac{\sqrt{2}}{3} \sqrt{2(\varepsilon_{xx}^2 + \varepsilon_{yy}^2 + \varepsilon_{zz}^2) - [\varepsilon_{xx}(-\varepsilon_{xx}) + \varepsilon_{yy}(-\varepsilon_{yy}) + \varepsilon_{zz}(-\varepsilon_{zz})] + 6(\varepsilon_{xy}^2 + \varepsilon_{yz}^2 + \varepsilon_{zx}^2)} \\
&= \frac{\sqrt{2}}{3} \sqrt{3(\varepsilon_{xx}^2 + \varepsilon_{yy}^2 + \varepsilon_{zz}^2) + 6(\varepsilon_{xy}^2 + \varepsilon_{yz}^2 + \varepsilon_{zx}^2)} \\
&= \sqrt{\frac{2}{3} [(\varepsilon_{xx}^2 + \varepsilon_{yy}^2 + \varepsilon_{zz}^2) + 2(\varepsilon_{xy}^2 + \varepsilon_{yz}^2 + \varepsilon_{zx}^2)]} \\
&= \sqrt{\frac{2}{3} \left[(\varepsilon_{xx}^2 + \varepsilon_{yy}^2 + \varepsilon_{zz}^2) + \frac{1}{2}(\gamma_{xy}^2 + \gamma_{yz}^2 + \gamma_{zx}^2) \right]} = \sqrt{\frac{2}{3} [(\varepsilon_1^2 + \varepsilon_2^2 + \varepsilon_3^2)]}
\end{aligned}$$

where γ_{ij} are engineering shear strains, and ε_1 , ε_2 , and ε_3 are principal strains.

When the deformation is axisymmetric, from the equation (10.2),

$$2\varepsilon_2 = 2\varepsilon_3 = -\varepsilon_1, \text{ hence}$$

$$\bar{\varepsilon}^p = \varepsilon_1 \tag{11.1}$$

When it is plane strain compression, according to the equation (10.4) and (10.5)

$$\varepsilon_2 = -\varepsilon_1 \text{ and } \varepsilon_3 = 0,$$

$$\bar{\varepsilon}^p = \frac{4}{3}\varepsilon_1 \tag{11.2}$$

12. Appendix E

The bridge used in the tube extrusion

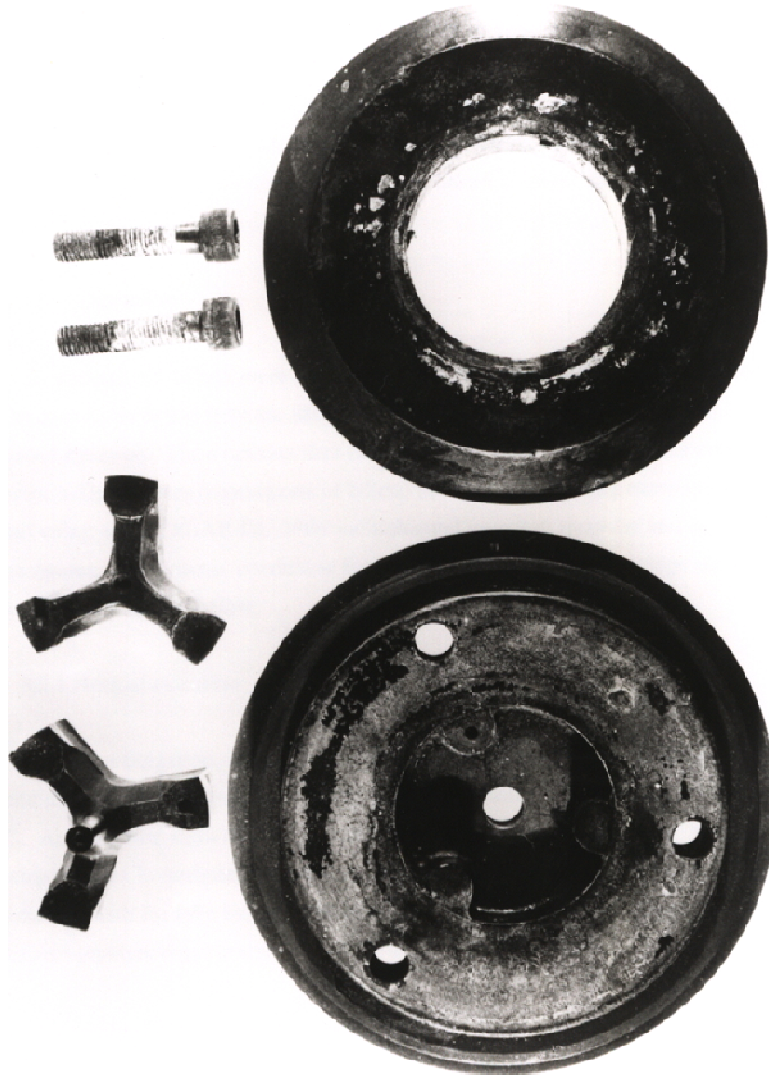


Figure 12.1 The bridge die used in the experiment (Nisaratanaporn 1995, p.74)

Billet length is about 100 mm.

Container diameter is 75 mm.

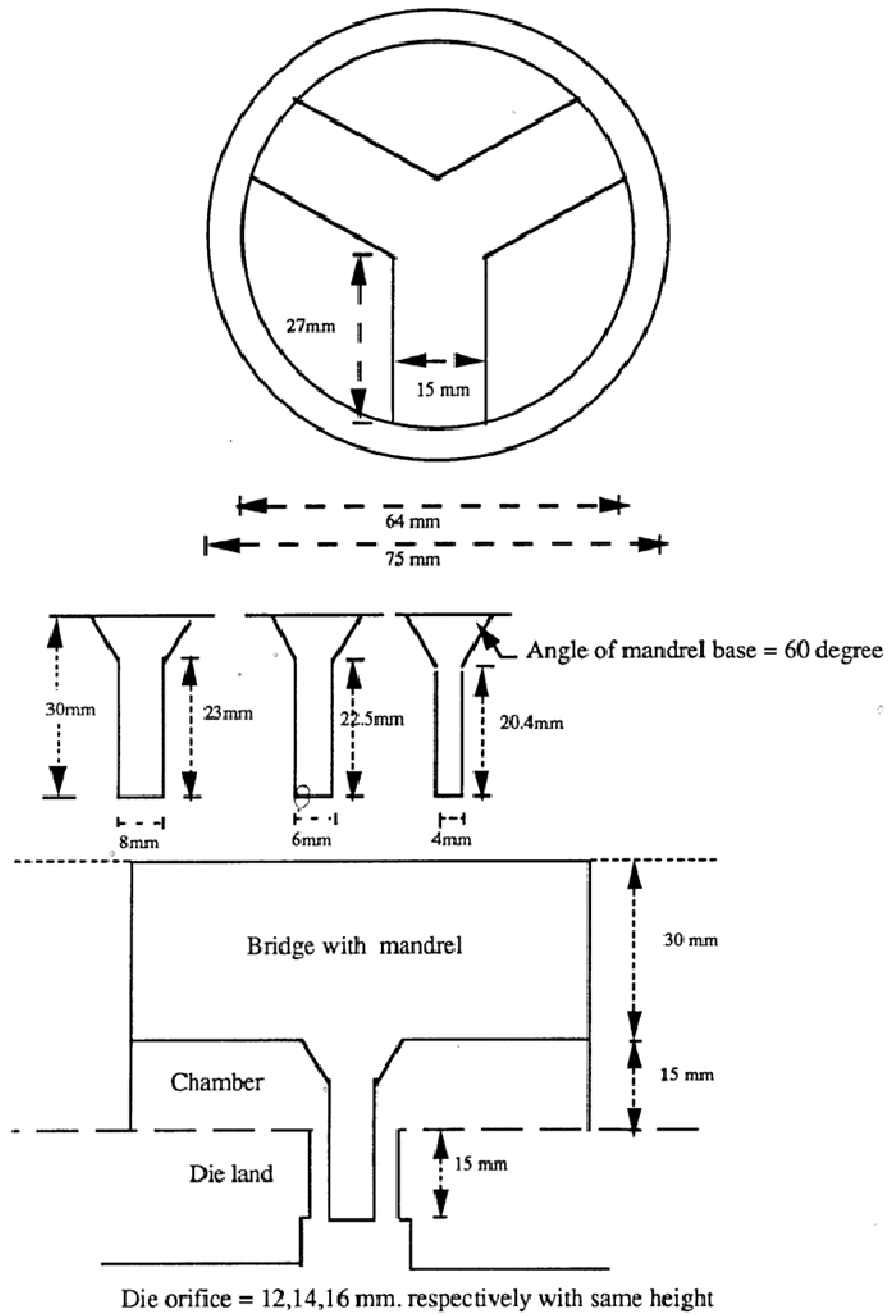


Figure 12.2 The dimensions of the die used in the study (Nisaratanaporn 1995, p.74)

13. Appendix F

The calculation of the constitutive equation constants

The flow stress data are from Akeret's work (1978) in which data are presented in the form of a series of graphs with true stress-true strain curves of different temperatures at a certain strain rate. To keep the influence of the temperature rise during the test as least as possible, only the peak stresses were selected for the constitutive equation calculation. These stresses were presented in Table 6.2 and represented below.

Stress (Mpa) \ Strain-rate(s ⁻¹)	0.05	0.1	0.2	0.5	1	2	5	10
Temperature (K)								
623	44	47	50	54	57.5	61	67	72
673	28	32	35	39	43	46.7	53	58
723	21	24.5	27	30.5	34.5	37.5	44	49.5
773	16.7	19.17	21	25	28.5	31.5	37	42
823	12.5	14.17	16	19.17	21.5	24.5	27.5	31

Table 13.1 Flow stress at different temperature and different strain rate Akeret's experiment (1978)

The goal of the data processing is to extract the necessary constants in equation (3.12). In hot working, the temperature and strain rate dependence of the stress can be expressed by the following constitutive equations

$$Z = \dot{\epsilon} \exp\left(\frac{\Delta H}{GT}\right) = A' \sigma^{n'} \quad (13.1)$$

$$Z = \dot{\epsilon} \exp\left(\frac{\Delta H}{GT}\right) = A'' \exp(\beta\sigma) \quad (13.2)$$

$$Z = \dot{\epsilon} \exp\left(\frac{\Delta H}{GT}\right) = A[\sinh(\alpha\sigma)]^n \quad (13.3)$$

where A' , n' , A'' , β , A , α , n are all constants and among them $\alpha = \beta/n'$. From equation (13.1), at constant temperature, $\beta = \frac{\partial \ln \dot{\epsilon}}{\partial \sigma}$, therefore the n' value can be achieved in Figure 13.1 by linear fitting the logarithmic strain rate against stress at one temperature. Finally a n' value is decided by the average of the slopes from different curves representing different temperatures. When the similar procedure applies to equation (13.2) β is decided by $n' = \frac{\partial \ln \dot{\epsilon}}{\partial \ln \sigma}$ in Figure 13.2. Then after α is determined by β/n' , because the equation (13.3) can be changed into

$$\ln[\sinh(\alpha\sigma)] = \frac{\ln \dot{\epsilon}}{n} + \left(\frac{\Delta H}{nG}\right)\left(\frac{1}{T}\right) - \frac{\ln A}{n} \quad (13.4)$$

once α is decided from the procedure described above, it is very convenient to apply a multiple regression analysis to equation (13.4) with a dependent variable of $\ln[\sinh(\alpha\sigma)]$ and two independent variables of $\frac{1}{T}$ and $\ln \dot{\epsilon}$ and $-\frac{\ln A}{n}$ is a constant.

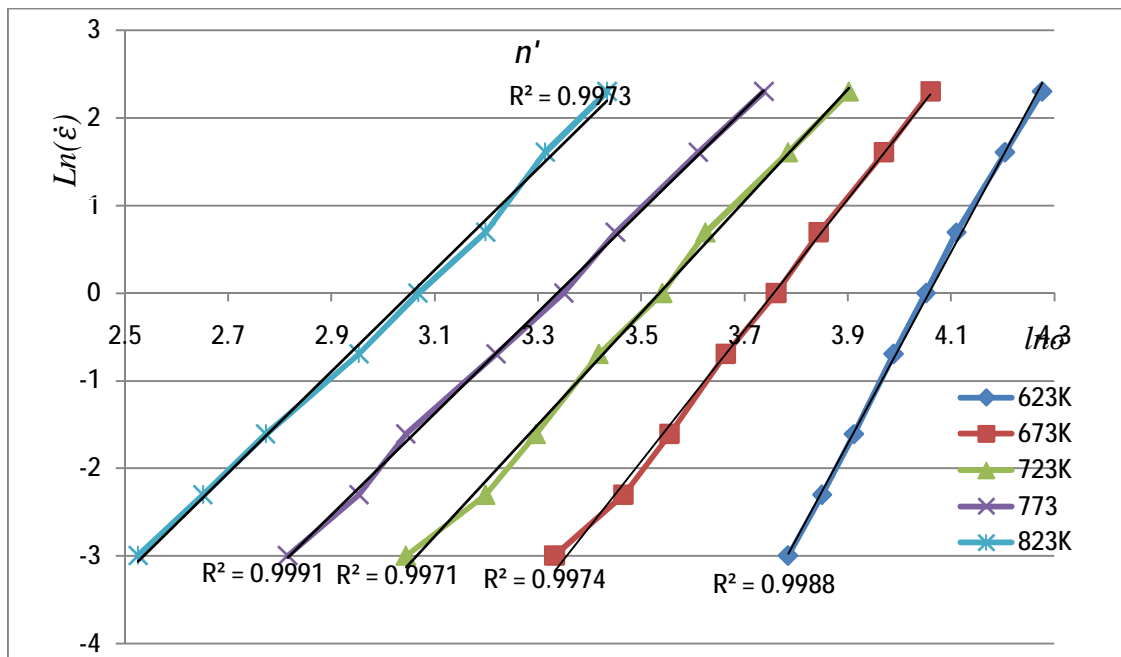


Figure 13.1 $\ln \dot{\epsilon}$ against $\ln \sigma$

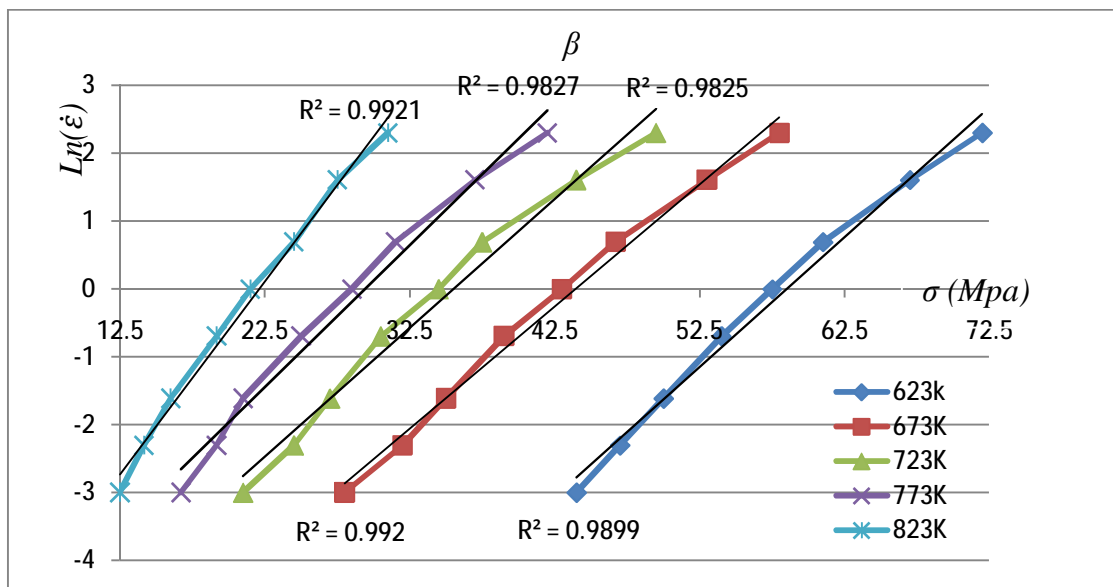


Figure 13.2 $\ln \dot{\epsilon}$ against σ

Using experimental data in Table 13.1, Figure 13.2 and Figure 13.1 can be drawn. The slopes of the fitted lines in Figure 13.2 and Figure 13.1 represent β and n'

respectively. Their average values are 0.065 and 2.31 so that $\alpha = \beta/n' = 0.0283$. Next using the α value to calculate $\ln[\sinh(\alpha\sigma)]$, a multiple regression operation, whose dependent variable is $\ln[\sinh(\alpha\sigma)]$ and two independent variables are $\frac{1}{T}$ and $\ln\dot{\epsilon}$ and constant $-\frac{\ln A}{n}$ was carried out. The derived coefficients for $\frac{1}{T}$ and $\ln\dot{\epsilon}$ and the interception are

$$\frac{\Delta H}{nG} = 3404.86 \quad (13.5)$$

$$\frac{1}{n} = 0.199 \quad (13.6)$$

$$-\frac{\ln A}{n} = -4.564 \quad (13.7)$$

Combining equation (13.5), (13.6) and (13.7), and using $G=8.314$, a complete set of constants for AA6063 alloy constitutive equation are achieved as

$$\alpha=0.0283, n=5.267, \Delta H=149103 \text{ and } A=2.75 \times 10^{10} \text{ or } \ln A=24.04.$$

14. References

- Abbod, M. F., Sellars, C. M., Cizek, P., Linkens, D. A., and Mahfouf, M., 2007. Modeling the flow behavior, recrystallization, and crystallographic texture in hot-deformed Fe-30wt% Ni austenite. *Metallurgical and Materials Transactions A-Physical Metallurgy and Materials Science*, 38A (10), 2400-2409.
- Ahmed, H., Wells, M. A., Maijer, D. M., Howes, B. J., and Winden, M. R. V. D., 2005. Modelling of microstructure evolution during hot rolling of AA5083 using an internal state variable approach integrated into an FE model. *Materials Science and Engineering A-structural Materials Properties Microstructure and Processing*, 390 (1-2), 278-290.
- Akeret, R., 1972. Properties of pressure welds in extruded aluminum alloy sections. *Journal Institute of Metals*, 10, 202-207.
- Akeret, R., 1978. *Atlas der warmformgebungseigenschaften von nichteisenmetallen band 1: Aluminiumwerkstoffe deutsche gesellschaft für metallkunde*.
- Ansys, I. Ansys mechanical solutions - technology. Available from: <http://www.ansys.com/solutions/solid-mechanics-contact.asp> [Accessed: 1st, June 2010].
- Avrami, M., 1939. Kinetics of phase change. I. General theory. *Journal of Chemical Physics*, 7 (12).
- Avrami, M., 1940. Kinetics of phase change.II. Transformation-time relations for random distribution of nuclei. *Journal of Chemical Physics*, 8 (2).
- Avrami, M., 1941. Kinetics of phase change. III. Granulation, phase change, and microstructure. *Journal of Chemical Physics*, 9 (2).
- Bandar, A., Weertruyden, W. V., and Misiolek, W. Z., 2008. Influence of geometric dynamic recrystallization in the dead metal zone on peripheral coarse grain. *In: the Ninth International Aluminum Extrusion Technology Seminar*, Orlando, Florida, USA.
- Bathe, K. J., 1996. *Finite element procedures* 2nd ed.
- Baxter, G. J., Furu, T., Zhu, Q., Whiteman, J. A., and Sellars, C. M., 1999. The influence of transient strain-rate deformation conditions on the deformed microstructure of aluminium alloy Al-1% Mg. *Acta Materialia*, 47 (8), 2367-2376.
- Belytschko, T., 2000. *Nonlinear finite elements for continua and structures*. Wiley-Blackwell.
- Bianchi, J. H., and Sheppard, T., 1987. A comparison of a viscoplastic finite-element model with slip-line field and upper-bound solutions for non-hardening material subjected to plane-strain and axisymmetrical extrusion. *International Journal of Mechanical Sciences*, 29 (1), 61-81.
- Blazek, J., 2001. *Computational fluid dynamics: Principles and applications*. Elsevier Science.

- Blum, W., Zhu, Q., Merkel, R., and McQueen, H. J., 1996. Geometric dynamic recrystallization in hot torsion of Al-5Mg-0.6Mn (AA5083). *Materials Science and Engineering A-structural Materials Properties Microstructure and Processing*, 205 (1-2), 23-30.
- Bograd, D.-I. S. Boundary element methods: Numerical solutions for engineering problems. Available from: http://www.iam.uni-stuttgart.de/bem/home_bem_introduc.html [Accessed: December 17 2008].
- Bonet, J., and Wood, R. D., 1997. *Nonlinear continuum mechanics for finite element analysis* Cambridge University Press.
- Bourqui, B., Huber, A., Moulin, C., Brunetti, A., and Krähenbül, Y., 2002. Improved weld seam quality using 3D FEM simulation in correlation with practice. In: *the first EAA extruder division congress*, Carda Holtel, Montichiari, Brescia, Italy.
- Bozzi, S., Vedani, M., Lotti, D., and Passoni, G., 2009. Extrusion of aluminium hollow pipes: Seam weld quality assessment via numerical simulation. *Metallurgical Science and Technology*, 27.
- Cahn, R. W., and Haasen, P., 1996. *Physical metallurgy (three volume set)*. Fourth ed.: North Holland.
- Carron, D., Bastid, P., Yin, Y., and Faulkner, R. G., 2010. Modelling of precipitation during friction stir welding of an Al-Mg-si alloy. *TECHNISCHE MECHANIK*, 1-3 (30), 29- 44
- Castle, A., Flory, R., and Gagg, J., 1988. Die design and construction in europe. In: *4th International aluminium extrusion technology seminar*, Chicago, Washington.
- Castle, A. F., 1992. Temperature control in aluminium extrusion. In: *5th International aluminium extrusion technology seminar*, Chicago, Washington.
- Castle, A. F., and Sheppard, T., 1976a. Development of product structure at commencement of extrusion. *Metals Technology*, 9 (3), 433-436.
- Castle, A. F., and Sheppard, T., 1976b. Pressure required to initiate extrusion in some Al-alloys. *Metals Technology*, 2, 465-475.
- CFD_Online. 9 June, 2008. What is the difference between FEM, FVM and FDM Available from: http://www.cfd-online.com/Wiki/General_CFD_FAQ [Accessed: April 25].
- Chadwick, R., 1970. The relevance of lubrication in extrusion. *Metals and Materials*, 4 (5), 201-207.
- Chanda, T., Zhou, J., and Duszczek, J., 2000. 3D FEM simulation of thermal and mechanical events occurring during extrusion through a channel-shaped die. In: *7th International aluminium extrusion technology seminar*, Chicago, Washington.
- Chen, B. K., Choi, S. K., and Thomas, P. F., 1991. Simulation of evolution of microstructure in a thermo-mechanical analysis of the hot rolling of aluminium. *Res Mechanica*, 31, 455-469.
- Chenot, J. L., Coupez, T., Fourment, L., and Ducloux, R., 1996. 3-D finite element

- simulation of the forging process: Scientific developments and industrial applications. *In: Altan, T. ed. 5th International Conference on technology of plasticity*, Columbus.
- Chenot, J. L., Coupez, T., Fourment, L., Ducloux, R., and Wey, E., 1999. Practical simulation of forging sequence of complex 3-D parts in industry. *In: Geiger, M. ed. 6th International Conference on technology of plasticity*, Nuremberg, Germany: Springer-Verlag Telos.
- Chenot, J. L., Fourment, L., Coupez, T., Ducloux, R., and Wey, E., 1998. Forge 3 - a general tool for practical optimization of forging sequence of complex three-dimensional parts in industry. *In: IMechE (C546/033/98)*, London, UK.
- Chopard, B., and Droz, M., 1999. *Cellular automata modeling of physical systems*. Cambridge University Press
- Chung, T. J., 2002. *Computational fluid dynamics* 1 ed.: Cambridge University Press.
- Clode, M. P., and Sheppard, T., 1990. Formation of die lines during extrusion of AA6063. *Materials Science and Technology*, 6 (8), 755-763.
- Cubic, D., Lencova, B., Read, F. H., and Zlamal, J., 1999. Comparison of FDM, FEM and BEM for electrostatic charged particle optics. *Nuclear Instruments and Methods in Physics Research Section A: Accelerators, Spectrometers, Detectors and Associated Equipment*, 427 (1-2), 357-362.
- Daaland, O., and Nes, E., 1996. Recrystallization texture development in commercial Al--Mn--Mg alloys. *Acta Materialia*, 44 (4), 1413-1435.
- Das, S., Abbod, M. F., Zhu, Q., Palmiere, E. J., Howard, I. C., and Linkens, D. A., 2007. A combined neuro fuzzy-cellular automata based material model for finite element simulation of plane strain compression. *Computational Materials Science*, 40 (3), 366-375.
- Dashwood, R. J., Mcshane, H. B., and Jackson, A., 1996. Computer prediction of extrusion limit diagrams. *In: 6th International aluminium extrusion technology seminar* Chicago. Washington
- Dieter, G. E., 1987. *Metallurgical fundamentals*. 2nd ed.
- Dobrzanski, L. A., and Trzaska, J., 2004. Application of neural networks to forecasting the CCT diagrams. *Journal Of Materials Processing Technology*, 157-158, 107-113.
- Doherty, R. D., Hughes, D. A., Humphreys, F. J., Jonas, J. J., Jensen, D. J., Kassner, M. E., King, W. E., Mcnelley, T. R., Mcqueen, H. J., and Rollett, A. D., 1997. Current issues in recrystallization: A review. *Materials Science and Engineering A*, 238 (2), 219-274.
- Donati, L., and Tomesani, L., 2004. The prediction of seam welds quality in aluminum extrusion. *Journal Of Materials Processing Technology*, 153-154, 366-373.
- Dorn, J. E., 1957. *Creep and recovery*. ASM.
- Duan, X., 2001. *Some problems in hot rolling of Al-alloys solved by the finite element method*. Thesis. Bournemouth University, Bournemouth, UK.
- Duan, X., and Sheppard, T., 2001. Prediction of temperature evolution by FEM

- during multi-pass hot flat rolling of aluminium alloys. *Modelling and Simulation in Materials Science and Engineering*, 9 (6), 525-537.
- Duan, X., and Sheppard, T., 2002a. Influence of forming parameters on static recrystallization behaviour during hot rolling aluminium alloy 5083. *Modelling and Simulation in Materials Science and Engineering*, 10 (4), 363-379.
- Duan, X., and Sheppard, T., 2002b. Influence of forming parameters on the final subgrain size during hot rolling of aluminium alloys. *Journal of Materials Processing Technology*, 130-131, 245-249.
- Duan, X., and Sheppard, T., 2003a. Computation of substructural strengthening by the integration of metallurgical models into the finite element code. *Computational Materials Science*, 27 (3), 250-258.
- Duan, X., and Sheppard, T., 2003b. Simulation and control of microstructure evolution during hot extrusion of hard aluminium alloys. *Materials Science and Engineering A-structural Materials Properties Microstructure and Processing*, 351, 282-292.
- Duan, X., Sheppard, T., and Velay, X., 2004. Prediction of flow stress and recrystallization by the finite element method during the hot extrusion of aluminum alloys. *In: 8th International aluminum extrusion technology seminar*, Orlando, Illinois.
- Ferziger, J., and Peric, M., 2002. *Computational methods for fluid dynamics*. 3rd ed.: Springer.
- Flitta, I., 2004. *Simulation of aluminium extrusion process*. Thesis (Ph.D). Bournemouth University, Bournemouth, UK.
- Flitta, I., and Sheppard, T., 2000. On the mechanics of friction during the extrusion process. *In: 7th International aluminium extrusion technology seminar*, Chicago, Washington.
- Flitta, I., and Sheppard, T., 2002. Simulation of bridge die extrusion using the finite element method. *Materials Science and Technology*, 18 (9), 987-994.
- Flitta, I., and Sheppard, T., 2003. Nature of friction in extrusion process and its effect on material flow. *Materials Science and Technology*, 19 (7), 837-846.
- Flitta, I., and Sheppard, T., 2004. Prediction and control of substructure evolution during aluminium extrusion using finite element modelling *In: ESAFORM 2004*, Trondheim, Norway.
- Flitta, I., and Sheppard, T., 2005. Effect of pressure and temperature variations on FEM prediction of deformation during extrusion. *Materials Science and Technology*, 21, 339-346.
- Flitta, I., Sheppard, T., and Peng, Z., 2007. FEM analysis to predict development of structure during extrusion and subsequent solution soak cycle *Materials Science and Technology*, 23 (5), 582-592.
- Furu, T., Shercliff, H. R., Baxter, G. J., and Sellars, C. M., 1999. The influence of transient deformation conditions on recrystallization during thermomechanical processing of an Al-1% Mg alloy. *Acta Materialia*, 47 (8), 2377-2389.

- Gandin, C. A., and Rappaz, M., 1994. A coupled finite element-cellular automaton model for the prediction of dendritic grain structures in solidification processes. *Acta Metallurgica Et Materialia*, 42 (7), 2233-2246.
- Garofalo, F., 1963. An empirical relation defining stress dependence of minimum creep rate in metals. *Transactions of the Metallurgical Society of Aime*, 227 (2), 351-365.
- Garofalo, F., 1966. *Fundamentals of creep and creep-rupture in metals*. MacMillan.
- Grasmo, G., Holthe, K., Storen, S., Valberg, H., Flatval, R., Hanssen, L., Lefstad, M., Lohne, O., Welo, T., Orsund, R., and Herberg, J., 1992. Modelling of two-dimensional extrusion. In: *5th International aluminium extrusion technology seminar* Chicago. Washington.
- Grong, and Shercliff, H. R., 2002. Microstructural modelling in metals processing. *Progress In Materials Science*, 47 (2), 163-282.
- Guillemot, G., Gandin, C. A., and Bellet, M., 2007. Interaction between single grain solidification and macrosegregation: Application of a cellular automaton-finite element model. *Journal Of Crystal Growth*, 303 (1), 58-68.
- Haepf, H.-J., and Roll, K., 1999. Future perspectives and limits for the mathematical modelling of metal forming processes in automotive industry. In: Geiger, M. ed. *6th International Conference on technology of plasticity*, Nuremberg, Germany: Springer-Verlag Telos.
- Herba, E. M., and McQueen, H. J., 2004. Influence of particulate reinforcements on 6061 materials in extrusion modeling. *Materials Science and Engineering A-structural Materials Properties Microstructure and Processing*, 372 (1-2), 1-14.
- Hesselbarth, H. W., and Gobel, I. R., 1991. Simulation of recrystallization by cellular automata. *Acta Metallurgica Et Materialia*, 39 (9), 2135-2143.
- Hill, R., 1950. *The mathematical theory of plasticity*. Oxford, Clarendon Press.
- Hirsch, J., 2006. *Virtual fabrication of aluminum products: Microstructural modeling in industrial aluminum production*.
- Hirth, J. P., and Loath, J., 1982. *Theory of dislocations*.
- Holt, D. L., 1970. Dislocation cell formation in metals. *Journal of Applied Physics*, 41 (8), 3197-3201.
- Hou, J., Bengtsson, B., and Lindqvist, H., 2000. FE-analysis of inward flow of surface materials at the back end of billet during Al-extrusion. In: *7th International aluminium extrusion technology seminar*, , Chicago. Washington
- Huang, D.-D., Jing-Yuan , L., Zhang, Z.-H., and Xie, J.-X., 2010. Metal flowing behaviors during diplopore extrusion of square tube with porthole die. *The Chinese Journal of Nonferrous Metals*, 20 (3), 488-495.
- Huang, Y.-J., 1998. Integrated computer aided extrusion process simulation, die design/ manufacturing, and management planning system. *Light Met. Age*, 56 (5-6), 76-81.
- Huang, Y., and Humphreys, F. J., 1999. Measurements of grain boundary mobility during recrystallization of a single-phase aluminium alloy. *Acta Materialia*, 47

- (7), 2259-2268.
- Huang, Y., and Humphreys, F. J., 2000. Subgrain growth and low angle boundary mobility in aluminium crystals of orientation $\{110\}\langle 001\rangle$. *Acta Materialia*, 48 (8), 2017-2030.
- Huda, Z., and Zaharinie, T., 2008. Kinetics of grain growth in 2024-T3: An aerospace aluminum alloy. *Journal Of Alloys and Compounds*, In Press, Corrected Proof.
- Humphreys, F. J., and Hatherly, M., 2004. *Recrystallization and related annealing phenomena*. Elsevier.
- Hurley, P. J., and Humphreys, F. J., 2003a. The application of EBSD to the study of substructural development in a cold rolled single-phase aluminium alloy. *Acta Materialia*, 51 (4), 1087-1102.
- Hurley, P. J., and Humphreys, F. J., 2003b. Modelling the recrystallization of single-phase aluminium. *Acta Materialia*, 51 (13), 3779-3793.
- Janssens, K., Raabe, D., Kozeschnik, E., Miodownik, M., and Nestler, B., 2007. *Computational materials engineering*. ACADEMIC PRESS.
- Jo, H. H., Jeong, C. S., Lee, S. K., and Kim, B. M., 2003. Determination of welding pressure in the non-steady-state porthole die extrusion of improved al7003 hollow section tubes. *Journal Of Materials Processing Technology*, 139 (1-3), 428-433.
- Johnson, W., and Kudo, H., 1962. *The mechanics of metal extrusion*. Manchester University Press.
- Jonas, J. J., Sellars, C. M., and Mcg, W. J., 1969. Strength and structure under hot-working conditions *International Metallurgical Reviews*, 130, 1-23.
- Jones, M. J., and Humphreys, F. J., 2003. Interaction of recrystallization and precipitation: The effect of Al_3SC on the recrystallization behaviour of deformed aluminium. *Acta Materialia*, 51 (8), 2149-2159.
- Jowett, C., Parson, N., and Fraser, W., 2000. Simulation of billet surface into the extruded product. *In: 7th International aluminium extrusion technology seminar*, Chicago. Washington
- Korczak, P., Dyja, H., and Labuda, E., 1998. Using neural network models for predicting mechanical properties after hot plate rolling processes. *Journal Of Materials Processing Technology*, 80-81, 481-486.
- Lens, A., Maurice, C., and Driver, J. H., 2005. Grain boundary mobilities during recrystallization of Al-Mn alloys as measured by In Situ annealing experiments. *Materials Science and Engineering: A*, 403 (1-2), 144-153.
- Li, L., Zhang, H., Zhou, J., Duszczynk, J., Li, G. Y., and Zhong, Z. H., 2008. Numerical and experimental study on the extrusion through a porthole die to produce a hollow magnesium profile with longitudinal weld seams. *Materials & Design*, 29 (6), 1190-1198.
- Libura, W., Richert, J., Pacanowski, J., and Senderski, J., 2000. Temperature-speed parameters in extrusion of thin-walled sections from aluminium alloys. *In: 7th International aluminium extrusion technology seminar*, Chicago, Washington.
- Lin, Y. C., Liu, G., Chen, M.-S., and Zhong, J., Prediction of static recrystallization in

- a multi-pass hot deformed low-alloy steel using artificial neural network. *Journal Of Materials Processing Technology*, In Press, Corrected Proof.
- Liu, G., Zhou, J., and Duszczek, J., 2008. FE analysis of metal flow and weld seam formation in a porthole die during the extrusion of a magnesium alloy into a square tube and the effect of ram speed on weld strength. *Journal Of Materials Processing Technology*, 200 (1-3), 185-198.
- Liu, G., Zhou, J., Huang, K., and Duszczek, J., 2007. Analysis of metal flow through a porthole die to produce a rectangular tube with weld seams. In: *Extrusion Workshop 2007 and 2nd Extrusion Benchmark* Bologna, Italy
- Lou, S., Zhao, G., Wang, R., and Wu, X., 2008. Modeling of aluminum alloy profile extrusion process using Finite Volume Method. *Journal Of Materials Processing Technology*, 206 (1-3), 481-490.
- Marthinsen, K., Holmedal, B., Abtahi, S., Valle, R., Chen, S., and Nes, E., 2003. Coupled FEM and microstructure modeling applied to rolling and extrusion of aluminium alloys. *Thermec'2003, Pts 1-5*, 426-4, 3777-3782.
- Marthinsen, K., and Nes, E., 1997. A general model for metal plasticity. *Materials Science and Engineering A*, 234-236, 1095-1098.
- Marthinsen, K., and Nes, E., 2001. Modelling strain hardening and steady state deformation of Al-Mg alloys. *Materials Science and Technology*, 17, 376-387.
- Mattiussi, C., and Peter, W. H., 2002. A reference discretization strategy for the numerical solution of physical field problems. In: *Advances in imaging and electron physics* Vol. Volume 121: Elsevier, 143-279.
- Mclaren, A. J., and Sellars, C. M., 1992. Modeling distribution of microstructure during hot-rolling of stainless-steel. *Materials Science and Technology*, 8 (12), 1090-1094.
- Mcqueen, H. J., 1977. Production and utility of recovered dislocation substructures. *Metallurgical Transactions a-Physical Metallurgy and Materials Science*, 8 (6), 807-824.
- Mcqueen, H. J., and Blum, W., 2000. Dynamic recovery: Sufficient mechanism in the hot deformation of Al (< 99.99). *Materials Science and Engineering A-structural Materials Properties Microstructure and Processing*, 290 (1-2), 95-107.
- Mollerbernd, N., Elsner, P., and Leppin, J., 1996. Mathematical computer-aided determination of heating processes in aluminium logs and billets during heating to extrusion temperature in gas-fired billet In: *6th International aluminium extrusion technology seminar*, Chicago, Washington.
- Nakamura, T., Bay, N., and Zhang, Z. L., 1997. FEM simulation of friction testing method based on combined forward rod-backward can extrusion. *Journal of Tribology-Transactions of the Asme*, 119 (3), 501-506.
- Nakamura, T., Tanaka, S., Hayakawa, K., and Takahashi, S., 2003. Tribo-testing method for estimating tribo-characteristics at piercing punch in backward can extrusion (c). *Lubrication Engineering*, 59 (4), 12-17.
- Nes, E., 1997. Modelling of work hardening and stress saturation in FCC metals.

- Progress in Materials Science*, 41 (3), 129-193.
- Nes, E., and Marthinsen, K., 2002. Modeling the evolution in microstructure and properties during plastic deformation of FCC-metals and alloys - an approach towards a unified model. *Materials Science and Engineering A-structural Materials Properties Microstructure and Processing*, 322 (1-2), 176-193.
- Nes, E., Pettersen, T., and Marthinsen, K., 2000. On the mechanisms of work hardening and flow-stress saturation. *Scripta Materialia*, 43 (1), 55-62.
- Nes, E., Vatne, H. E., Daaland, O., Furu, T., Ørsund, R., and Marthinsen, K., 1994. *Physical modelling of microstructural evolution during thermomechanical processing of aluminium alloys*. Trondheim, Norway SINTEF (STF24 S94003).
- Nisaratanaporn, E., 1995. *Microstructural development and pressure requirements in 6063 aluminium alloy tube extrusion*. Thesis (Ph.D). university of london, London, UK.
- Niu, L., Sheppard, T., and Velay, X., 2008. Process optimisation and metal flow analysis of direct and indirect extrusion of aluminium using FEM simulation. *In: 6th International conference on manufacturing research (ICMR08)*, Brunel University, UK.
- Nix, W. D., Gibeling, J. C., and Hughes, D. A., 1985. Time-dependent deformation of metals. *Metallurgical Transactions a-Physical Metallurgy and Materials Science*, 16 (12), 2215-2226.
- Paterson, S. J., 1981. *The direct and indirect extrusion of aluminium alloys*. Thesis. Imperial College of Science and Technology, London, UK.
- Peng, Z., 2005. *Numerical modelling of the aluminium extrusion process*. Thesis (Ph.D). Bournemouth University, Bournemouth, UK.
- Peng, Z., and Sheppard, T., 2004. Study of surface cracking during extrusion of aluminium alloy AA2014. *Materials Science and Technology*, 20 (9), 1179-1191.
- Peng, Z., and Sheppard, T., 2004 Prediction of static recrystallization during shaped extrusion. *In: 8th International aluminum extrusion technology seminar*, Orlando, Illinois.
- Plata, M., and Piwnik, J., 2000. Theoretical and experimental analysis of seam weld formation in hot extrusion of aluminum alloys. *In: Proceedings of 7th International aluminium extrusion technology seminar*.
- Raabe, D., 1998. *Computational materials science: The simulation of materials microstructures and properties* John Wiley & Sons Canada, Ltd. .
- Raj, S. V., and Pharr, G. M., 1986. A compilation and analysis of data for the stress dependence of the subgrain size. *Materials Science and Engineering*, 81 (1-2), 217-237.
- Reddy, J. N., 2006. *An introduction to the Finite Element Method*. McGraw-Hill Higher Education.
- Rossi, P. L. O., and Sellars, C. M., 1997. Quantitative metallography of recrystallization. *Acta Materialia*, 45 (1), 137-148.

- Saha, P. K., 2000. *Aluminium extrusion technology*. Material park, Ohio: ASM International.
- Saha, P. K., 2004 Use of tribology to improve performance and quality in aluminum extrusion. *In: 8th International aluminum extrusion technology seminar*, Orlando, Illinois.
- Schikorra, M., Donati, L., Tomesani, L., and Kleiner, M., 2007. The role of friction in the extrusion of AA6060 aluminum alloy, process analysis and monitoring. *Journal Of Materials Processing Technology*, 191 (1-3), 288-292.
- Sellars, C. M., 1990. Modelling microstructural development during hot rolling. *Materials Science and Technology*, 6, 1072-1081.
- Sellars, C. M., 1997. An internal state variable approach to modelling microstructural evolution during thermomechanical process. *In: Chandra, T., and Sakai, T. eds. Thermec'97 international conference on thermomechanical processing of steels & other materials* University of Wollongong, Australia.
- Sellars, C. M., Tegart, W., and Mcg, J., 1972. Hot workability. *International Metallurgical Reviews*, 17 (1), 1-24.
- Sellars, C. M., and Zhu, Q., 2000. Microstructural modelling of aluminium alloys during thermomechanical processing. *Materials Science and Engineering A-structural Materials Properties Microstructure and Processing*, 280 (1), 1-7.
- Sheppard, T., 1984. Metallurgical aspects of direct and indirect extrusion. *In: 3rd International aluminium extrusion technology seminar*, Atlanta, Washington.
- Sheppard, T., 1993. Extrusion of aa2024 alloy. *Materials Science and Technology*, 9, 430-440.
- Sheppard, T., 1999a. *Extrusion of aluminium alloys*. Dordrecht, Netherlands: Kluwer Academic Publishers.
- Sheppard, T., 1999b. Temperature changes occurring during extrusion of metals: Comparisons of bulk, numerical, and integral profile predictions with experimental data. *Materials Science and Technology*, 15, 459-463.
- Sheppard, T., and Duan, X., 2002. Modelling of static recrystallisation by combining FEM with empirical models. *Journal of Materials Processing Technology*, 130-131, 250-253.
- Sheppard, T., and Jackson, A., 1997. Constitutive equations for use in prediction of flow stress during extrusion of aluminium alloys. *Materials Science and Technology*, 13 (3), 203-209.
- Sheppard, T., Nisaratanaporn, E., and Mcshane, H. B., 1998. Material flow and pressure prediction when extruding through bridge dies. *Zeitschrift fuer Metallkunde/Materials Research and Advanced Techniques*, 89, 327-337.
- Sheppard, T., and Raghunathan, N., 1989. Modification of cast structures in Al-Mg alloys by thermal treatments. *Materials Science and Technology*, 5 (3), 268-280.
- Sheppard, T., and S.J. Paterson. 1982. Direct and indirect extrusion of aluminum-alloys. *Metals Technology*, 9 (Jul), 274-281.
- Sheppard, T., and Tutcher, M. G., 1980. Development of duplex deformation

- substructure during extrusion of a commercial Al-5Mg-0.8Mn Alloy. *Metal Science*, 14 (12), 579-589.
- Sheppard, T., and Velay, X., 2007. Innovative methodologies for the simulation of static recrystallisation during the solution soaking process of shape extrusion. *In: Extrusion Workshop 2007 and 2nd Extrusion Benchmark* Bologna, Italy
- Sheppard, T., and Wood, E. P., 1980. Effect of section geometry on extrudability of Al-Cu-Mn alloy. *Metals Technology*, 7 (Feb), 58-66.
- Sheppard, T., and Wright, D. S., 1979a. Determination of flow-stress .1. Constitutive equation for aluminum-alloys at elevated-temperatures. *Metals Technology*, 6 (Jun), 215-223.
- Sheppard, T., and Wright, D. S., 1979b. Determination of the constitutive equations for aluminium alloys at elevated temperatures. *Metals Technology*, 6, 215-223.
- Shercliff, H. R. 1997. Modelling and materials processing: Cambridge University
- Shercliff, H. R., and Lovatt, A. M., 1999. Modelling of microstructure evolution in hot deformation. *Philosophical Transactions of the Royal Society A: Mathematical, Physical and Engineering Sciences*, 357 (1756), 1621-1643.
- Shercliff, H. R., and Lovatt, A. M., 2001. Selection of manufacturing processes in design and the role of process modelling. *Progress In Materials Science*, 46 (3-4), 429-459.
- Subramaniyan, J., 1989. *Extrusion of 2024 aluminium alloy sections*. Thesis. University of London, London.
- Talamantes-Silva, J., Abbod, M. F., Cabrera, E. S. P., Howard, I. C., Beynon, J. H., Sellars, C. M., and Linkens, D. A., 2009. Microstructure modelling of hot deformation of Al-1%Mg alloy. *Materials Science and Engineering: A*, 525 (1-2), 147-158.
- Transvalor. 2009a. Forge 2009 documentation - datafile forge2v44.
- Transvalor. 2009b. Forge 2009 documentation - datafile forge3v74.
- Transvalor. 2009c. Forge 2009 documentation - user routines.
- Tuschy, E., 1971. Differences in flow behaviour during extrusion of various materials. *Zeitschrift Fur Metallkunde*, 62 (7), 513-516.
- Tutcher, M. G., 1979. *Deformation processing applied to the Al-Mg alloy system*. Thesis (Ph.D). Imperial College of Science and Technology, London, UK.
- Underwood, E. E., 1970. *Quantitative stereology*.
- Valberg, H., 2002. Extrusion welding in aluminium extrusion. *International Journal of Materials and Product Technology*, 17 (7), 497-556.
- Valberg, H., and Loeken, T., 1992. Formation of the outer surface layers of the profile in direct and indirect extrusion. *In: 5th International aluminium extrusion technology seminar* Chicago, Washington.
- Valberg, H., and Malvik, T., 1996. Metal flow in die channels of extrusion investigated by an experimental grid pattern technique. *In: 6th International aluminium extrusion technology seminar* Chicago. Washington
- Vatne, H. E., Furu, T., Ørsund, R., and Nes, E., 1996. Modelling recrystallization after hot deformation of aluminium. *Acta Materialia*, 44 (11), 4463-4473.

- Velay, X., 2004. *Analysis of the conform process: A specific form of aluminium extrusion*. Thesis (Ph.D). Bournemouth University, Bournemouth, UK.
- Velay, X., Duan, X., and Sheppard, T., 2003. *Prediction of material flow pattern in the hot extrusion of aluminium alloys by the finite element method*. Paper presented at the THERMEC'2003, Universidad Carlos III de Madrid, Leganes, Spain.
- Vierod, R. P., 1983. *The effect of copper additions on the deformation processing of aluminium alloys*. Thesis (Ph.D). University of London, London, UK.
- Wagener, H. W., and Wolf, J., 1994. Coefficient of friction in cold extrusion. *Journal Of Materials Processing Technology*, 44 (3-4), 283-291.
- Weertman, J., 1968. Dislocation climb theory of steady-state creep. *Asm Transactions Quarterly*, 61 (4), 681.
- Wei, Y. O. U., Wei-Hong, X. U., Ya-Xiu, L. I. U., Bing-Zhe, B. a. I., and Hong-Sheng, F., 2007. Effect of chromium on CCT diagrams of novel air-cooled bainite steels analyzed by neural network. *Journal of Iron and Steel Research, International*, 14 (4), 39-42.
- Wood, E. P., and Sheppard, T., 1975. Evaluation of shape factors for aluminium alloy extrusions. *Aluminium* 51 (12), 760-764.
- Wright, D. S., and Sheppard, T., 1979. Determination of flow-stress .2. Radial and axial temperature distribution during torsion testing. *Metals Technology*, 6 (Jun), 224-229.
- Xie, X., Huang, D., Li, J., and Zhang, Z., 2009. *A numerical simulation technique for hollow section using porthole die*. China CN200910088960.7.
- Zaidi, M. A., and Sheppard, T., 1982. Development of microstructure throughout roll gap during rolling of aluminum-alloys. *Metal Science*, 16 (5), 229-238.
- Zaidi, M. A., and Sheppard, T., 1983. Recrystallization mechanisms in commercial Al-2Mg alloy. *Metal Science*, 17 (5), 219-228.
- Zasadzinskii, J., and Misiolek, W., 1988. Estimating optimal speed/temperature parameters to maximise hot extrusion exit speed. *In: 4th International aluminium extrusion technology seminar*, Chicago, Washington.
- Zener, C., and Hollomon, J. H., 1944. Effect of strain rate upon plastic flow of steel. *Journal Of Applied Physics*, 15 (1), 22-32.
- Zhu, Q., 1994. *Effect of subgrain boundaries in plastic deformation of aluminium alloys*. Thesis (Ph.D). university of Erlangen-Nuremberg.
- Zhu, Q., Abbod, M. F., Talamantes-Silva, J., Sellars, C. M., Linkens, D. A., and Beynon, J. H., 2003. Hybrid modelling of aluminium-magnesium alloys during thermomechanical processing in terms of physically-based, neuro-fuzzy and finite element models. *Acta Materialia*, 51 (17), 5051-5062.
- Zhu, Q., and Sellars, C. M., 1996. Microstructural modelling of hot deformation behaviour of single phase alloys in continuous and reversing deformation. *In: the Proc. of 2nd Int. Conf. on Modelling of Metal Rolling Processes*, London.
- Zhu, Q., and Sellars, C. M., 2000. Microstructural evolution of aluminium-magnesium alloys during thermomechanical processing. *Aluminium Alloys*:

- Their Physical and Mechanical Properties, Pts 1-3*, 331-3, 409-420.
- Zhu, Q., and Sellars, C. M., 2001. Evolution of microbands in high purity aluminium-3% magnesium during hot deformation testing in tension-compression. *Scripta Materialia*, 45 (1), 41-48.
- Zhu, Q., Sellars, C. M., and Bhadeshia, H. K. D. H., 2007. Quantitative metallography of deformed grains. *Materials Science and Technology*, 23 (7), 757-766.
- Zhu, Q., Shercliff, H. R., and Sellars, C. M., 1997, Jul 07-11. *Modelling hot deformation behaviour based on evolution of dislocation substructures*. Paper presented at the 2nd International Conference on Thermomechanical Processing of Steels and Other Materials (THERMEC 97), Wollongong, Australia.
- Zienkiewicz, O. C., and Taylor, R. L., 2005. *The Finite Element Method sixth edition: 3 volume set*. Sixth ed.: Butterworth-Heinemann.
- Zienkiewicz, O. C., Taylor, R. L., Papadopoulos, P., and Onate, E., 1990. Plate bending elements with discrete constraints - new triangular elements. *Computers & Structures*, 35 (4), 505-522.
- Zienkiewicz, O. C., Taylor, R. L., and Zhu, J. Z., 2005. *The Finite Element Method: Its basis and fundamentals*. Butterworth-Heinemann publications.

15. Publications

Niu, L., Sheppard, T., and Velay, X., 2008. Process optimisation and metal flow analysis of direct and indirect extrusion of aluminium using FEM simulation. *In: 6th International conference on manufacturing research (ICMR08)*, Brunel University, UK

Sheppard, T., Velay, X. and Niu, L., On Material Flow and Aspects of Structural Modification during Direct and Indirect Extrusion of an Aluminium Alloy, resubmitted after revision according to the feedback from Journal of Materials Processing Technology